Propeller Blade Optimisation for Minimised Perceived Noise

The Role of Blade Sweep and Comparison with Physical Noise Minimisation

Aerospace Engineering Master's Thesis — Guillaume D. J. van Dijk

TU Delft
Delft University of Technology

Propeller Blade Optimization for Minimized Perceived Noise

The Role of Blade Sweep and Comparison with Physical Noise Minimization

by

Guillaume D.J. van Dijk

in partial fulfillment of the requirements for the degree of

Master of Science

in Aerospace Engineering

at the Delft University of Technology,

to be defended publicly on May 20th, 2025.

Thesis committee:	
Chair:	Prof. dr. ing. G. Eitelberg
Supervisor:	Dr. ir. T. Sinnige (responsible)
	Prof. dr. ing. G. Eitelberg
External examiner:	Dr. D. Ragni
Place:	Faculty of Aerospace Engineering, Delft
Student number:	4672968

TU Delft Delft University of Technology

PREFACE

As I write this on Liberation Day in the Netherlands, the 5th of May, I could not have chosen a more symbolic moment to submit my Master's Thesis. The past nine months have been challenging—a rollercoaster to say the least—but they have taught me much, not only about technical topics but also about myself. This journey, and my entire academic path, has shaped me into a better researcher and engineer, and has deepened my admiration for the academic world and the field of aerospace engineering. It has fuelled my passion for engineering more than ever before.

I want to express my gratitude to my supervisors, Tomas Sinnige and Georg Eitelberg, for guiding me through this process and giving me the freedom to approach this study in the way I envisioned. Although there were moments when my progress did not meet expectations, I believe I completely turned things around after the midterm, and the final result is something I am truly proud to call my own. Additional thanks go to the inspiring Technical University of Delft, which enables and supports such educational journeys. It is a place that will always remain close to my heart.

During this time, I had the privilege of working side by side with two of my best friends, Job and Casper, who were also completing their Master's theses and successfully finished theirs a few months ago. I'll never forget the countless coffee breaks, darting sessions, and debates over who brought the best lunch. Let's be honest—those lunches were often the brightest moments of the day.

After they graduated, my enthusiasm for quadcopter drones took centre stage. Organizing flying sessions and diving into drone design significantly boosted my confidence in engineering. It helped me work more efficiently and consistently—even when the progress on my thesis report wasn't going as hoped. That experience, among many others, has greatly enriched this thesis, making it a fitting capstone to my academic career.

I'm deeply thankful to all my friends and family who supported me—especially when this thesis consumed nearly all my time and energy. A final thank you to my girlfriend, Isa, for being there for me. I'll never forget the fun I had during the final days of writing when I replaced every "-ize" with "-isa" while switching my spelling from American to British English.

This thesis has been the most meaningful academic journey I've ever experienced—one that will stay very dear to me throughout all the journeys to come.

Guillaume D.J. van Dijk
Delft, May 2025

SUMMARY

With the increasing emphasis on fuel efficiency and the growing demand for short-haul flights, propeller aircraft—offering higher propulsive efficiency than turbofan engines—may experience a resurgence, particularly as electric regional aviation is showing potential. However, the lack of a shroud around propeller blades can result in elevated noise annoyance, potentially hindering the reintroduction of this technology. While reduced-noise propeller design is well-documented, the influence of perceived noise on propeller design remains underexplored.

This thesis investigates the role of noise perception—modelled through Effective Perceived Noise Level (EPNL), defined in ICAO Annex 16, Volume I—in propeller (blade) design, especially with regard to blade sweep distribution. Blade sweep is shown to primarily affect high-frequency tonal noise, which is weighted higher in perceived noise with respect to physical noise. This difference between perceived and physical noise can potentially lead to a different blade design when including noise perception in the trade-off between noise reduction and required power. As the influence of noise perception in propeller design is little investigated in literature, this study is split up into a first study to research the broader influence of noise perception in propeller design in a parameter study, and second, an optimisation study is done to do a deep dive in propeller (blade) design for minimising perceived noise.

Aerodynamic and aeroacoustic modelling is performed using a Vortex Lattice Method and Hanson's Helicoidal Surface Theory, focusing solely on tonal noise components. In the optimisation study, an Euler-Beam structural model is used to put a constraint on the blade shape.

The initial parameter study is conducted under both take-off and cruise conditions to evaluate the effects of various parameters on both physical and perceived noise, as well as the noise reduction resulting from blade sweep. The parameters investigated include blade number, rotational tip Mach number, thrust level, and flight Mach number. A full factorial design is employed, varying each of these parameters between predefined "low" and "high" values. Since the thrust level is itself one of the variables, it is held constant at either its low or high value for each run in an implicit way by varying the blade pitch accordingly. To isolate the effect of blade sweep, each simulation is performed twice—once with blade sweep and once without, while maintaining constant thrust in both cases. The results show that blade sweep has little effect on both perceived and physical noise during cruise, justifying a focus on take-off conditions for further analysis. Most notably in the remainder of this study, first, it is shown that at higher rotational velocities, sweep is more efficient at reducing perceived noise, while overall noise levels, both with and without sweep, decrease as rotational velocity increases, indicating that the latter effect is the dominant noise-reduction mechanism, an effect that will show its importance in the optimisation study. Secondly, two opposing effects are observed: increasing rotational velocity amplifies the sweep-induced reduction in perceived noise but diminishes the physical noise reduction. For perceived noise, the benefit of reducing higher-weighted frequencies with sweep outweighs the penalty of less favourable blade loading. Since this does not hold for physical noise, it suggests that the optimal blade design for minimising perceived noise may differ from that for minimising physical noise—a divergence explored in greater depth in the optimisation study.

In the second phase of this study, the trade-off between reducing Effective Perceived Noise Level and the power required is explored. Multiple Pareto fronts are constructed by running a series of optimisations in take-off conditions. Each Pareto front begins with a propeller optimised for minimum required power; from that baseline, Effective Perceived Noise Level is then minimised while imposing an increasing power penalty that grants the optimiser increasing freedom to adjust design parameters in order to reduce noise. The variables that are used in optimisation are blade pitch, advance ratio, and spanwise distributions of sweep and twist, each represented by Bézier curves. This process is repeated twice—once holding blade radius constant and once holding blade length constant—to isolate the effect of sweep-induced changes in loading. Because increasing blade sweep inherently lengthens the blade, with a constant blade radius, it reduces blade loading, which results in a key mechanism for sweep-induced noise. To differentiate between the effects of sweep versus blade loading (to reduce noise), two additional Pareto fronts are generated for the constant-length case

using reduced design-vector dimensionality. Finally, relevant optimisations are repeated while minimising physical noise to compare optimal propellers for perceived versus physical noise reduction.

It is found that optimising for EPNL or physical noise does not lead to significantly different optimised propeller blades, as the optimiser primarily reduces the rotational velocity. This shifts the tonal noise spectrum toward lower frequencies, where blade sweep becomes less effective.

Starting from the initial propeller blade that minimises the required power, through allowing a penalty of +1% and +2% in required power, the combination of advance ratio and blade pitch can reduce the EPNL by 12 dB and 19 dB, respectively. Introducing blade twist distribution yields an additional 2 dB reduction, and incorporating blade sweep provides a further 4 dB reduction.

Secondly, a significant difference is observed in the noise reduction mechanisms between constant blade length and constant blade radius. For a constant blade length, noise is reduced primarily through phase cancellation in the tip region, resulting in maximum tip sweep. For constant blade radius, the blade length is increased by allowing maximum sweep along the entire blade span (within the structural stress constraint), effectively lowering blade loading and thus noise. This results in an additional noise reduction of 8 dB and 2 dB for the +1% and +2% power penalty cases, respectively, compared to the constant blade length optimisation.

Contents

Nomenclature

β Blade pitch angle [deg]

$\beta_{0.7}$ Blade pitch angle at $0.7R_p$ [deg]

ΔPNL Perceived Noise Reduction [dB]

ΔSPL Physical noise reduction [dB]

ΔV_t Radial induced velocity [m/s]

γ Blade sweep angle [deg]

γ Local twist angle relative to $\beta_{0.7}$ [deg]

Λ Blade sweep angle [deg]

Λ Sweep angle between mid-chord line and X-X axis [deg]

$\mathbf{e}_\eta$ Unit vector along the η-axis [-]

$\mathbf{e}_\zeta$ Unit vector along the ζ-axis [-]

Ω Angular velocity [rad/s]

ϕ_0 Phase shift due to offset [-]

ϕ_s Phase shift due to sweep [-]

$\Psi_D(k_x)$ Normalized source transform of drag noise [-]

$\Psi_L(k_x)$ Normalized source transform of lift noise [-]

$\Psi_V(k_x)$ Normalized source transform of thickness noise [-]

ρ Air density [kg/m^3]

σ Normal stress [Pa]

σ_{VM} Von Mises stress [Pa]

τ Shear stress [Pa]

θ Radiation angle [deg]

A_L Cross-sectional area of the blade along the local coordinate system [m^2]

BPF Blade Passage Frequency [Hz]

c Chord length [m]

c/R_p Normalized chord length [-]

c_0 Ambient speed of sound [m/s]

C_D Section drag coefficient [-]

C_L Section lift coefficient [-]

C_T Thrust coefficient [-]

D Diameter of the propeller [m]

D Duration correction factor [-]

d/c Maximum camber-to-chord ratio [-]

dt Incremental time step [s]

dx Incremental distance along flight path [m]

$EPNL$ Effective Perceived Noise Level [dB]

$ESPL$ Effective Sound Pressure Level [dB]

f Sound frequency in noise departure frame of reference[Hz]

f_d Doppler-shifted frequency [Hz]

f_{harm}^{PNL} Harmonic Fraction of Perceived Noise [dB]

f_{harm}^{SPL} Harmonic Fraction of PhysicalNoise [dB]

FA Face alignment [-]

h Flight altitude [m]

$H(X)$ Normalized thickness distribution [-]

I_η Moment of inertia about the η-axis [m^4]

I_ζ Moment of inertia about the ζ-axis [m^4]

J Advance ratio [-]

J_{mN_b} Bessel function of the first kind [-]

k_x Chordwise wave number [-]

k_y Local dimensionless wave number [-]

M_r Sectional helicoidal Mach number [-]

M_t Tip Mach number in the rotational plane [-]

M_t Tip rotational Mach number [-]

M_x Flight Mach number [-]

M_{rt} Tip helicoidal Mach number [-]

MCA Mid-chord alignment [-]

n Rotational frequency [rev/s]

N_b	Number of blades [-]
N_b	Number of blades in the propeller [-]
N_c	Number of chordwise points [-]
N_k	Perceived noisiness [noy]
N_s	Number of spanwise points [-]
N_w	Number of wake points [-]
$OSPL$	Overall Sound Pressure Level [dB]
$OSPL^{RMS}$	Root Mean Square of Overall Sound Pressure Level [dB] over the entire noise directivity
$p(t)$	Pressure as a function of time [Pa]
P_{mN_b}	Fourier coefficient of pressure at the m-th harmonic [Pa]
p_{ref}	Reference pressure threshold for human hearing (2e-5 Pa) [Pa]
P_{req}	Required Power [W]
PNL	Perceived Noise Level [dB]
$PNLT$	Tone-corrected Perceived Noise Level [PNLdB]
$PNLTM$	Maximum Tone-corrected Perceived Noise Level [PNLdB]
Q	Torque [Nm]
r	Radial position on the blade [m]
R_p	Propeller radius [m]
R_{hub}	Hub radius [m]
r_{obs}	Observer distance [m]
SPL_m	Sound Pressure Level at the m-th harmonic [dB]
T	Thrust [N]
t/c	Maximum thickness-to-chord ratio [-]
t_0	Reference time duration (10 seconds) [s]
t_1, t_2	Time bounds for noise integration [s]
U_∞	Freestream velocity [m/s]
V_∞	Freestream velocity [m/s]
V_a	Axial induced velocity [m/s]
V_t	Radial velocity [m/s]
V_{eff}	Effective velocity [m/s]
x/c	Chordwise position of maximum camber [-]

List of Figures

List of Tables

I

BACKGROUND

1
INTRODUCTION

The interest in efficient aviation raises the potential of implementing propellers. A range of new configurations and concepts for air mobility are emerging, utilising propellers as their primary means of propulsion. When transporting more people, noise generation increases, and so does its relevance [18]. To assess the noise produced, it is crucial to understand how humans perceive it. To incorporate the role of noise perception, aircraft noise certification involves metrics that account for key characteristics to represent human perception of noise accurately. One of the important aspects is the sensitivity of human hearing to a specific frequency range between 2000 and 5000 Hz , which increases the importance of reducing noise in this bandwidth of the frequency spectrum [19]. Consequently, this role of human perception impacts how propellers are designed to include noise reduction. Among the available techniques, applying a sweep distribution to the blades presents a method to reduce the higher-harmonic noise without significantly affecting aerodynamic performance [6], which is especially important when looking at perceived noise. To research this effect, a fundamental study with isolated propellers can add to the backbone for designing propellers for perceived noise.

Looking at the history of flight, after the Wright brothers' first powered flight in 1903, propellers were the only means of propulsion for aircraft. From that point on, the propeller became a big subject of research, which got a boost from the Great War. In 1919, Lynam and Webb's first publication on developing a noise prediction method emerged [20], aiming to make propellers quieter for operations over enemy territory [21]. However, this relevance declined after World War II when turbojet engines were introduced. Their superior cruise speeds and low oil prices led to their dominance in aircraft propulsion. Interest in propellers resurfaced during the 1973-1974 oil crisis when fuel efficiency became more relevant [22]. With this oil embargo encouraging propeller development, the start of the Advanced Turboprop Project ushered in a new era of propeller research [23]. This mirrors the current trend driven by concerns over global warming, where sustainable and efficient flight is more important than ever. Although the research momentum gained during the oil crisis faded as fuel prices stabilised, the urgency surrounding global warming is not temporary. The aviation industry now faces a growing urgency to improve efficiency for long-term sustainability. Climate change is becoming more problematic each year. Aviation is responsible for 2% of global greenhouse gas emissions and rises 3%-4% annually. [18]. In this way, international aviation is expected to triple its proportional share of a Paris-compatible 1.5 °C budget for global temperature rise by 2050 under current international policies. Since current development is too focused on improving fuel consumption through engines, aerodynamic improvements, and weight reduction, revolutionary designs with propellers can offer much promise [24].

Turbofan engines with a high bypass ratio have become the standard for passenger aircraft. By accelerating a larger fraction of the total airflow with a smaller velocity increment, high-bypass turbofans achieve efficient propulsion at high cruise Mach numbers, offering an optimal commercial balance between speed and fuel economy. Although propellers are limited to lower cruise speeds and cannot operate efficiently at the higher Mach numbers of turbofans, they exhibit superior propulsive efficiency at their optimal cruise Mach number. Specifically, while the optimal cruise Mach number for turbofans is approximately 0.75, propellers operate

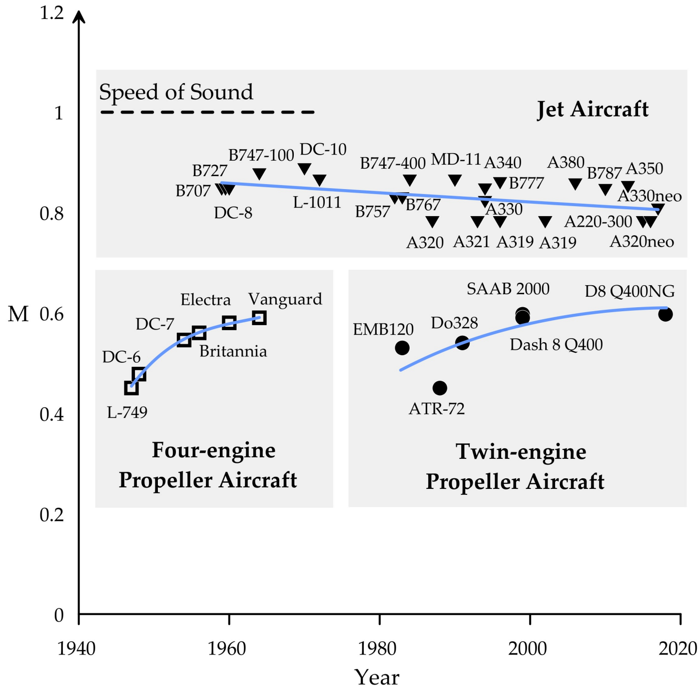

Figure 1.1: Historical development in maximum cruise speeds for commercial aircraft [1]

most efficiently around Mach 0.55 [25]. At these respective cruise speeds, propellers demonstrate higher efficiency than turbofans [1]. As a trend is seen where the airspeed of propeller and turbofan aircraft move closer together (Figure 1.1 and fuel efficiency is chosen above trip duration; a comeback of this "outdated tech" could show promise.

Whilst gaining propulsive efficiency, noise problems are challenging to tackle due to the lack of a shroud around the blades. The human population is growing in many countries, and flight movements are also increasing, leading to more aircraft noise annoyance. As the share of propeller aircraft grows, the consequences on human health due to this annoyance will have to be considered. Unwanted sounds often disrupt activities that require a quiet environment, reduce communication quality, and contribute to stress. Other factors that lower the quality of life, like the resulting sleep disturbance and increased physiological health effects like cardiovascular disease, have resulted from exposure to too much environmental noise [26] which are all problems that could potentially be worsened with added noise generation by introducing new propeller aircraft and visa versa can slow down the reintroduction of propeller aircraft.

While noise is usually described with metrics based on the amplitude of pressure waves in the air, when looking at how humans process sound, different factors must be considered to study perceived noise. For this reason, the Effective Perceived Noise Level is brought to life, which includes effects of perceived loudness, different frequency amplitude, and duration of the noise event [2]. Through this assessment, a translation is made from physical noise to perceived noise.

Looking at the effect of converting noise to perceived noise, going from Sound Pressure Level (SPL) to Perceived Noise Level (PNL), it can be seen that generally higher-frequency sound is perceived as being louder. This can have a significant impact on designing propellers to reduce perceived noise, as this means that reducing higher-frequency sound becomes more important.

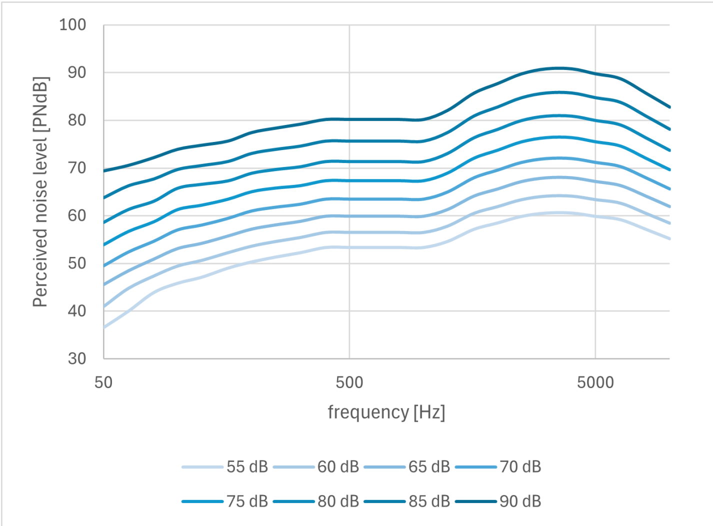

Figure 1.2: Perceived noise level over a range of frequencies at a constant Specific Noise Level (60dB to 90dB) based on [2]

Although extensive research has been conducted on propeller design to optimise the standard noise metric, research specifically aimed at reducing perceived noise remains limited. While some work is available on what noise reduction could be achieved for open rotors and passenger aircraft using Effective Perceived Noise (EPNL)[27, 28], the specific consequence of including noise perception in designing propulsion systems is still underexposed. In addition, most methods for reducing propeller noise affect all harmonics in a similar manner. While being effective ways of reducing noise, most methods are equally effective at reducing both noise and perceived noise.

These methods reduce the tonal noise by radiating pressure in a less efficient way, thereby affecting the amplitude across all harmonics more or less in the same way. By adding more detailed blade parameters to the optimisation methods, noise can be reduced by changing the shape of the blade to spread noise radiation such that far-field sound amplitude is reduced, utilising destructive interference [6]. The most effective way of reducing noise through this method is by adding a sweep distribution, which is studied in multiple optimisation studies [7, 29, 30]. Figure 1.3 shows that adding blade sweep, noise reduction is higher for higher harmonics.

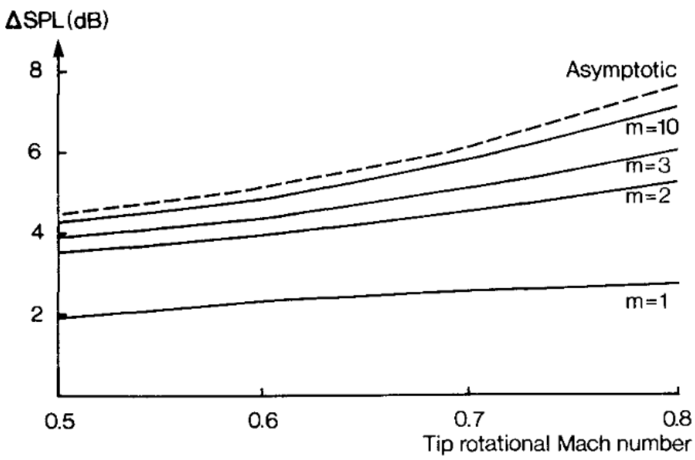

Figure 1.3: Numerical and asymptotic predictions of the effect of blade sweep on a subsonic propeller; 12 blades, 50-deg tip sweep [3]

The enhanced reduction of higher-frequency noise, combined with the greater auditory sensitivity to these frequencies, raises questions about the implications of including perceived noise metrics in propeller design, particularly for determining the optimal sweep distribution.

1.1. THESIS AIM AND OBJECTIVE

Extensive research has examined the trade-off between propeller noise and efficiency, but little attention has been paid to the impact of noise perception on propeller design. Converting noise to perceived noise gives higher weights to higher frequencies, which could potentially open up a more subtle way of reducing perceived noise with less unfavourable effect on aerodynamic performance. As blade sweep has been proven to be more effective at higher harmonics than the lower ones, the added importance of higher frequencies could potentially be used to reduce perceived noise more efficiently. The next logical step, therefore, is to determine if sweep distribution should be tailored when the objective shifts from minimising physical noise to minimising perceived noise.

To do so, the objective of this study is the following:

Research Objective

Quantify the impact of optimising blade sweep for minimised perceived noise

Obtaining the goal of this research, while taking into account the gap in the knowledge regarding noise perception in propeller design, the study is divided into two parts: the first develops a broad understanding of this subject through a parameter study, and the second conducts an in-depth optimisation targeting perceived noise minimisation.

The first part of this study, therefore, investigates how physical noise and perceived noise respond differently across a wide range of flight conditions and propeller configurations. The following research questions are formulated to guide this investigation.

Research Question 1

How do operating conditions (and blade count) influence the sweep-induced reduction of perceived noise?

This question will be addressed through the following sub-questions:

1. At which flight condition is including noise perception in propeller design the most relevant?
2. Which parameters have the most influence on sweep-induced (perceived) noise reduction, and what is the most significant difference in response between physical and perceived noise?
3. What role does harmonic noise play in these trends?

The parameter study is done on the effect of operating conditions and blade count on (perceived) noise and the reduction thereof by adding blade sweep. This will be done through executing a full factorial study, varying the number of blades, flight Mach number, tip rotational Mach number, and thrust from a "high" to "low" value, and assessing the response in perceived noise and physical noise, the sweep-induced reduction thereoff and the difference between those metrics. While varying these factors, thrust is kept at the predetermined value through implicitly varying pitch to ensure a fair comparison. The sweep-induced noise reduction will be calculated by performing every run with a straight and a swept blade. The difference in harmonic content will be analysed, as this results in different levels of noise and perceived noise. The goal of this study is to know what role is played by the harmonic content, analyse what parameters are dominant, and determine their interaction. These takeaways lead to knowledge that is used in the second part of this research and provide starting conditions for the optimisation that will be done.

Insights from this first study define the optimisation problems and baseline propeller configurations for the second phase, forming a toolbox to address subsequent research questions. The second phase will then explore the trade-off between reducing Effective Perceived Noise Level and required power, compare optimal propeller designs for perceived versus physical noise reduction, and investigate the role of blade loading in these optimisations.

To obtain these findings, the second research question is formulated as follows:

Research Question 2

How does blade sweep contribute to the trade-off between Effective Perceived Noise Level and required power?
This question will be addressed through the following sub-question:

1. What is the difference in the resulting sweep distribution when optimising Effective Perceived Noise Level and the physical noise equivalent?
2. In the trade-off between Effective Perceived Noise Level and required power, what is the difference in contribution of blade sweep and blade loading (distribution)?

Starting from a propeller optimised for minimum required power, Effective Perceived Noise Level is minimised under increasing power penalties to give the optimisation algorithm increased freedom in reducing noise. In this way, multiple Pareto fronts are formed, with blade pitch, advance ratio, and spanwise sweep and twist distribution as design variables. By repeating this with constant blade radius and constant blade length—and adding reduced-dimensionality cases—the study isolates the sweep-induced noise reduction from noise reduction due to favourable blade loading. Parallel optimisations are also done to target physical noise instead of perceived noise to reveal how (and if) optimal sweep distributions differ when minimising perceived versus physical noise.

1.2. REPORT OUTLINE

This report is organised into four main parts. The first part, presented in Part I, gives aim to the study and provides a literature review that sets the context for the work. The second part, Part II, begins with the parametrisation of the propeller geometry and the discretisation of its blades. It proceeds to describe the models developed to predict the propeller's aerodynamic performance and blade loading in chapter 4; its aeroacoustic behaviour in chapter 5, and its structural predictions in chapter 6. This part concludes with the validation of these models, as detailed in chapter 7.

The third part, Part III, explains the methodology used in the applied parameter and optimisation study. It includes the setup and execution of a parametric study in chapter 8, as well as the formulation and approach of the optimisation study in chapter 9.

The fourth part, Part IV, presents the outcome of both studies. The findings of the parametric study, discussed in chapter 10, among others, guide the selection of relevant flight conditions and design parameters for the optimisation study. These are then used in the optimisation study, the results of which are presented in chapter 11.

The final part of the report, Part V, draws conclusions from the overall findings, reflects on the results, and highlights key insights into propeller design. It also outlines several recommendations and directions for future work.

2

Overview of relevant work in propeller research

This chapter gives background to studying the reduction of propeller tonal noise, and through the effect of including noise perception, an emphasis will be put on higher harmonics. First, in section 2.1, the basic principles of propeller propulsion are presented, and characteristics for performance assessment are detailed. section 2.2 goes through the noise sources of propellers and noise reduction optimisations. The concept of noise perception is shown in section 2.3 and section 2.5, which focuses on the frequency envelope and reduction of harmonic noise. Lastly, an overview is given of the work on aerodynamic modelling that is used in this Thesis in section 2.6.

2.1. Propeller Aerodynamics and Performance Characteristics

To address the basic principles of propeller propulsion and the assessment of its performance, general propeller theory is covered to establish a theoretical foundation [31] [32].

Propellers generate thrust by accelerating air from flight speed, V, with downstream velocity increment, ΔV, to the final slipstream velocity, $V + \Delta V$. In momentum theory, due to this acceleration, some energy is lost in creating a slipstream, which means that the higher the velocity increment, the lower the propulsive efficiency, η_p. This efficiency is defined as the ratio of thrust power P to the change in kinetic energy flux, ΔE_{kin}, delivered from the propeller to the flow as shown in Equation 2.2. At a constant speed, the propulsive efficiency can thus only be increased by reducing the velocity increment, ΔV. To maintain the same thrust, the mass flow, $\dot{m}$, has to increase, thus increasing the propeller diameter for better efficiency.

$$T \approx \dot{m} \cdot \Delta V \tag{2.1}$$

$$\eta_p = \frac{P}{\Delta \dot{E}_{kin}} = \frac{2}{2 + \frac{\Delta V}{V}} \tag{2.2}$$

To assess the performance of a propeller, the power, thrust, and operating conditions are evaluated with dimensionless parameters to obtain results that can be used to compare different cases. As the propeller has to achieve thrust by the acceleration of air, aerodynamic losses are induced, which are quantified by propeller efficiency, η. This is the ratio of propeller power, P, to the shaft power, P_{shaft}, which takes into account the drag of the blades, and thus the propeller torque, through Equation 2.6. This characterisation is typically expressed using three dimensionless parameters: the thrust coefficient, C_T, the power coefficient, C_P, and the advance ratio, J. These parameters are made dimensionless with rotational frequency n the flow density ρ_∞ and the propeller diameter, D, and are defined as follows:

$$\eta = \frac{P}{P_{shaft}} = \frac{VT}{\Omega Q} = \frac{C_T}{C_Q}\frac{J}{2\pi} = J\frac{C_T}{C_P} \tag{2.3}$$

$$C_T = \frac{T}{\rho_\infty n^2 D^4} \tag{2.4}$$

$$C_P = \frac{P}{\rho_\infty n^3 D^5} = 2\pi C_Q \tag{2.5}$$

$$J = \frac{V}{nD} \tag{2.6}$$

The rotational frequency, n, relates to angular velocity with; $n[\frac{rev}{s}] = \frac{\Omega[\frac{rad}{s}]}{2\pi}$. Additionally, some frequently used dimensionless velocities as given in Equation 2.7

$$M_x = \frac{V_\infty}{a_\infty} \tag{2.7}$$

$$M_T = \frac{\Omega R}{a_\infty} = \frac{\pi n D}{a_\infty}\frac{V_\infty}{V_\infty} = M_x\frac{\pi}{J} \tag{2.8}$$

$$M_r = \sqrt{M_x^2 + r^2 M_T^2} \tag{2.9}$$

$$M_{rt} = \sqrt{M_x^2 + R^2 M_T^2} \tag{2.10}$$

M_x and M_T are the flight Mach number and tip Mach number in the rotational plane, respectively, and M_x and M_{rt} are the sectional helicoidal Mach number and tip helicoidal Mach number, respectively. R and r are the propeller radius and radial position, respectively.

To generate the velocity increment, the propeller's blades provide lift and drag. This lift and drag can be decomposed into thrust and torque, T and Q, in a process that changes due to different pitch and incidence angles across the blade. This can be illustrated in detail through blade element theory, which treats each blade as a series of 2D airfoils with associated forces and velocities, as shown in Figure 2.1.

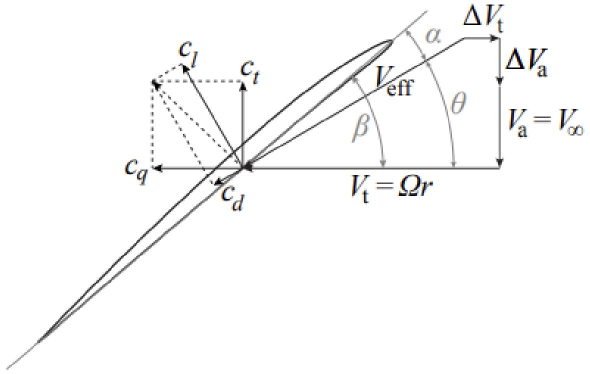

Figure 2.1: Velocity diagram and resulting force components of a propeller blade section at radial position r [4]

This figure shows a radial element at an arbitrary position on the blade and chord length, c, that is considered an individual airfoil, exposed to incoming axial flow, $V_\infty + V_a$, and to the radial velocity, $V_t = \Omega r$, which is reduced by the radial induced velocity, ΔV_t, due to the swirl created by the propeller to give, $V_t - \Delta V_t$. These velocity components can be combined to give the effective velocity, V_{eff}.

$$V_{eff} = \sqrt{(V_\infty + \Delta V_a)^2 + (\Omega r - \Delta V_t)^2} \tag{2.11}$$

The angle formed by the effective velocity and the plane of rotation is the aerodynamic advance angle θ. Using this angle, along with the velocity diagram and the airfoil characteristics, $c_l(\alpha, Re, M)$ and, $c_d(\alpha, Re, M)$, the thrust and power required can be calculated by summing Equations 2.12 and 2.13 over all blades.

$$dT = \frac{1}{2}\rho V_{eff}^2 c(c_l \cos\theta - c_d \sin\theta)\, dr, \tag{2.12}$$

$$dQ = \frac{1}{2}\rho V_{eff}^2 \Omega r\, c(c_l \sin\theta + c_d \cos\theta)\, dr. \tag{2.13}$$

2.2. AEROACOUSTICS

Propellers lack a casing around the blades that can shield noise, and apply acoustic liners to attenuate it. The large diameters of propellers and high flight velocity result in high tip speeds, leading to an increase in the amplitude of sound emissions through a rotating pressure field. Understanding the various noise sources associated with propellers is crucial to minimising their sound emissions. As this study will be performed on isolated propellers in purely axial flow, information will be focused on steady, tonal noise. An overview work on propeller noise is used for this general theory of propeller noise [33].

The produced noise can be categorised in the following way:

- Tonal noise sources
- Broadband noise sources

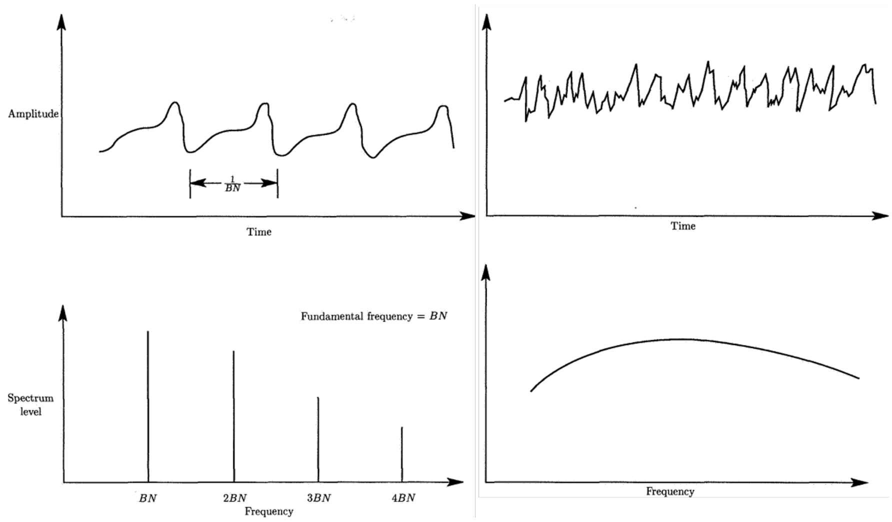

Figure 2.2: Characteristics of propeller tonal noise (left) and broadband noise (right) [5]

Tonal noise can be built out of sinusoids with frequencies being multiples of the blade passage frequency (BPF), which is defined as the number of blades times the rotational frequency. Broadband noise is random noise containing all frequencies. With such a continuous spectrum, the frequency spectrum contains a shape of amplitudes related to the frequencies. Broadband noise also includes narrowband noise, which is random noise concentrated around the harmonics. This narrow-band noise is especially spread out at higher harmonics.

Steady Sources As the propeller rotates, the load and thickness distribution cause a steady pressure field in the rotating frame, which observers in a static frame perceive as noise. This steady pressure field in the rotating frame becomes noise to the observer. It can be subdivided into three sources:

- Thickness noise
- Loading noise

- Quadrupole noise

Thickness noise results from the periodic air displacement due to the propeller blade volume. This source is particularly relevant at high tip speeds, as amplitude scales with the blade volume. The noise components are affected by blade volume, variation in blade cross-section, and rotational speed. Thickness noise is dominant for high speeds and for thicker blades.

Loading noise is generated by pressure disturbances associated with the propeller blade loading, which can be divided into thrust and torque components or as lift and drag from the blades using a slightly rotated reference frame. It is dominant at lower tip speeds and when the blade loading is high.

While thickness and loading noise can be modelled by placing monopoles and dipoles, respectively, on the surface of the blades, **quadrupoles** can be placed in the volume surrounding the blades for noise accounting for the viscous and propagation effects that the thickness and loading sources cannot cover. At local transonic speeds, quadrupole interaction enhances thickness and loading sources.

Unsteady Noise While in the rotating plane, the pressure field is steady over time, there are also noise sources that are time-dependent on this plane of rotation. This unsteady noise results from the associated circumferential variation of the blade loading, leading to constructive or destructive interference with steady-loading noise. Typical causes are the effect of the propeller incidence angle to the incoming flow, counter-rotating propellers, and the installation of the propeller on the wing and airframe.

Broadband The first broadband noise source is turbulence-ingestion noise, which arises when inflow turbulence interacts with the leading edges of the propeller blades, creating random fluctuations in blade loading. It becomes significant under conditions of high inflow turbulence at low speeds. Trailing-edge noise is the second broadband mechanism. This noise results from the scattering of turbulent boundary layers from the trailing edge and is characterised by the boundary layer properties.

2.3. NOISE PERCEPTION

Sound can be described in multiple metrics. The most used one is sound pressure level (SPL) in decibels (dB).

$$SPL = 20log_{10}(\frac{P}{P_{ref}}) \tag{2.14}$$

Where P is the pressure of the sound wave and P_{ref} is the reference pressure, usually taken as the threshold of hearing at $2 \cdot 10^{-5} N/m^2$.

To calculate how much people perceive the produced Sound Pressure Level, different metrics are brought to life to assess that sound and to use that to study noise, and also for certification purposes. The Effective Perceived Noise Level (EPNL), measured in units of EPNdB, is the primary metric used in aircraft noise certification [2]. EPNL serves as an evaluator of the subjective effects of airplane noise on human listeners, combining factors such as the perceived loudness, different frequency amplitudes, and duration of the noise event. It is derived from the Perceived Noise Level (PNL), incorporating corrections for spectral irregularities (tones) and duration effects to capture the complex human response to noise.

The calculation of EPNL from the raw pressure data proceeds through a series of steps:

1. The 24 one-third octave bands of sound pressure level are converted to perceived noisiness (noy) using the method described in section A36.4.2.1 (a). The noy values are combined and then converted to instantaneous perceived noise levels, PNL(k).
2. A tone correction factor $C(k)$ is calculated for each spectrum to account for the subjective response to the presence of spectral irregularities.
3. The tone correction factor is added to the perceived noise level to obtain tone-corrected perceived noise levels PNLT(k), at each one-half second increment:

$$\text{PNLT}(k) = \text{PNL}(k) + C(k)$$

The instantaneous values of tone-corrected perceived noise level are derived and the maximum value, PNLTM, is determined.

4. A duration correction factor, D, is computed by integration under the curve of tone-corrected perceived noise level versus time.

5. Effective perceived noise level, EPNL, is determined by the algebraic sum of the maximum tone-corrected perceived noise level and the duration correction factor:

$$\mathrm{EPNL} = \mathrm{PNLTM} + D$$

The first step in the process is to convert the sound pressure levels in each of the 24 one-third octave bands into perceived noisiness values, termed *noy*. This conversion uses a standardisad procedure that reflects the subjective response to noise at different frequencies. The individual noy values for each band are combined to yield an instantaneous Perceived Noise Level, denoted as $PNL(k)$, at each time increment k. An example of this conversion can be seen in Figure 2.3, where it can be clearly seen that the higher frequencies are perceived as louder than lower ones.

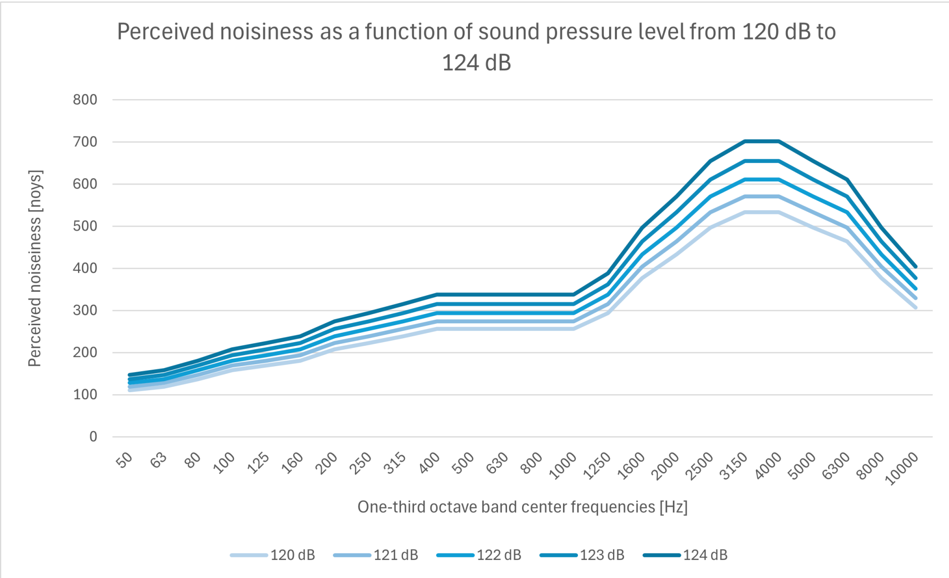

Figure 2.3: Example of the conversion from sound pressure level to perceived noisiness [2]

Next, a tone correction factor, $C(k)$, is applied to account for the highest tones throughout the frequency spectrum, which are known to increase the subjective annoyance of noise. The tone correction factor is calculated at each time increment and added to the Perceived Noise Level to obtain the tone-corrected Perceived Noise Level, $PNLT(k)$:

$$PNLT(k) = PNL(k) + C(k) \tag{2.15}$$

In addition to the tone correction, a duration correction factor, D, is computed to reflect the influence of the noise event's length on perceived annoyance. The duration correction is obtained by integrating the tone-corrected Perceived Noise Level, $PNLT(k)$, over the time of the noise event. This integral quantifies the total annoyance and acknowledges that longer durations have a more substantial impact on perception. This duration correction factor D is summed to the maximum tone-corrected perceived noise level to complete the conversion to EPNL:

$$EPNL = PNLTM + D \tag{2.16}$$

2.4. NOISE REDUCTION

In this section, methods are presented to reduce propeller noise and to showcase the trade-off between noise and efficiency. Magliozzi et al. in [33] and Miller et al. [34] give good fundament for noise reduction, and additionally Hanson, with his work [6] show ways of reducing noise through spreading the noise sources over the blade and in this way reducing tonal noise by the concept of non-compactness which are most effective when looking at airfoil shape and distributions in blade sweep, twist and chord. Lastly, a range of optimisation studies further expand on these noise reduction methods [7] [35] [36], [37], [38].

The most significant means of reducing propeller noise is reducing tip speed. By reducing tip speed, the rotational relative Mach number decreases, and as all noise components scale with M_r^2, the noise decreases drastically. Although this does decrease thrust, when compensating for this, overall noise reduction is still achieved. Next to that, the rotational relative Mach number is also part of the Bessel function and thus decreases radiation efficiency when decreasing tip speed. Another effective way of reducing noise is to reduce disk loading, which is best achieved by increasing the propeller diameter. Doing so reduces loading noise, which is most effective at low speeds. As propeller diameter is often a required maximum, the balance between reducing tip speed and disk loading to achieve the best trade-off between noise reduction and propeller efficiency is complex. In addition to this trade-off, all propeller have their own characteristics in aerodynamics and aeroacoustics. A list is provided below with the evaluation of the most critical parameters.

- Increasing the **number of blades**, blade loading can be reduced by spreading it over more blades. This reduces loading and quadrupole noise, which is most effective at low speeds where loading noise dominates. While this does decrease noise, it shifts the noise spectrum to higher frequencies that are perceived as being louder. Adding blades can also increase thickness noise because the overall blade volume is increased. Nonetheless, overall noise reduction is expected with an increase in the number of blades.

- Increasing **blade thickness**, increases noise due to a greater cross-sectional area moving through the air, which amplifies thickness noise. This noise reduction is most effective at high speeds where thickness noise dominates. While thinner blades can thus help reduce this noise source, structural considerations often limit how thin a blade can be made.

- Increasing **propeller diameter** reduces noise by allowing for lower rotational speeds, which reduces tip speed and noise from compressibility effects. It also spreads the aerodynamic load over a bigger area, reducing blade loading and, thus, loading noise. Especially at low speeds, this high propeller diameter also adds to the propeller's efficiency.

- Adjusting the **twist and chord distribution** over the span can shift the loading distribution more inboard. The load is transferred to locations with a lower Mach number and radiating less noise. The most significant addition to this noise reduction, however, comes from obtaining a better aerodynamic performance through a better load distribution.

- As **blade sweep** distribution will play a significant role in this study, some extra background is provided:

Blade sweep is added to propeller blades to decrease drag because of transonic compressibility in the same way as this is used for wing sweep; additionally, for lower flight Mach numbers, noise is reduced by dephasing [6] sound frequencies. As the same frequency noise signals radiate from different parts of the blade, these signals are partly cancelled because of destructive interference, thus reducing noise. When the phases of these signals are shifted more, this dephasing can be increased. The primary method of doing that is by adding backwards sweep like in Figure 2.4.

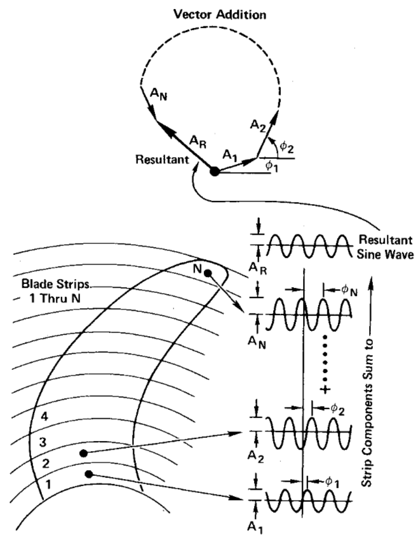

Figure 2.4: Conceptual benefit of sweep: resultant signal is the sum of elemental contributions at all radii [6]

Following the Helicoidal surface theory for harmonic noise [39], the noise reduction can be shown by vector addition of the noise signals of the same frequency noise in the complex plane, 2.4. For such a single harmonic, the amplitude A_j and phase lag ϕ_j of all blade strips across its span are summed to obtain the total noise as in Equation 2.17.

$$A_R e^{i\phi_s} R = \sum_{j=1}^{N} A_j e^{i\phi_{sj}} \tag{2.17}$$

As can be seen in Figure 2.4, the higher the phase lag is, the more the vectors fold in on themselves and thus contribute to noise reduction. The phase lag is calculated in Equation 2.18 where the most important notes are that it increases with sweep, MCA, flight Mach number, M_x, and blade passing frequency harmonics mB.

$$\phi_s = \frac{2mBM_T}{M_r(1 - M_x cos\theta)} \cdot \frac{MCA}{D} \tag{2.18}$$

Noise reduction through phase cancellation is dependent on the radiation angle as shown in Figure 2.5.

OPTIMISATION STUDIES

This section will go through studies into optimising noise while maintaining a certain propeller performance parameter, and study more in-depth phenomena when doing so.

An optimisation algorithm that uses these parameters to reduce noise while maintaining performance is the optimisation study by Ingraham [37]. Fixing other parameters, the chord distribution is optimised so that the loading lies more inboard for noise reduction. This reduces the thickness and loading noise by decreasing the blade area where noise radiates best. By adding the propeller diameter to the design variables, it is immediately maximised. In this way, the aerodynamic loads are spread, and a reduction in rotational speed can be realised. Finally, by increasing blade loading, the rotational velocity is gradually reduced.

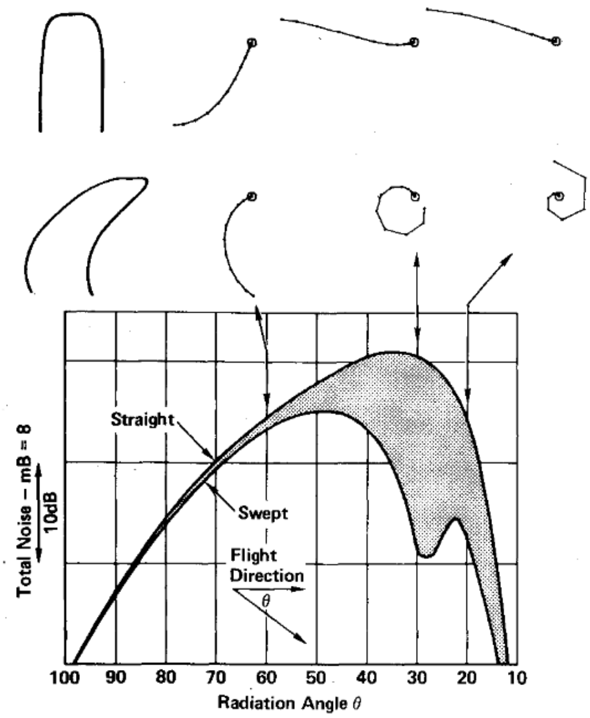

Figure 2.5: Directivity dependence of phase interference due to sweep at prop fan cruise condition [6]

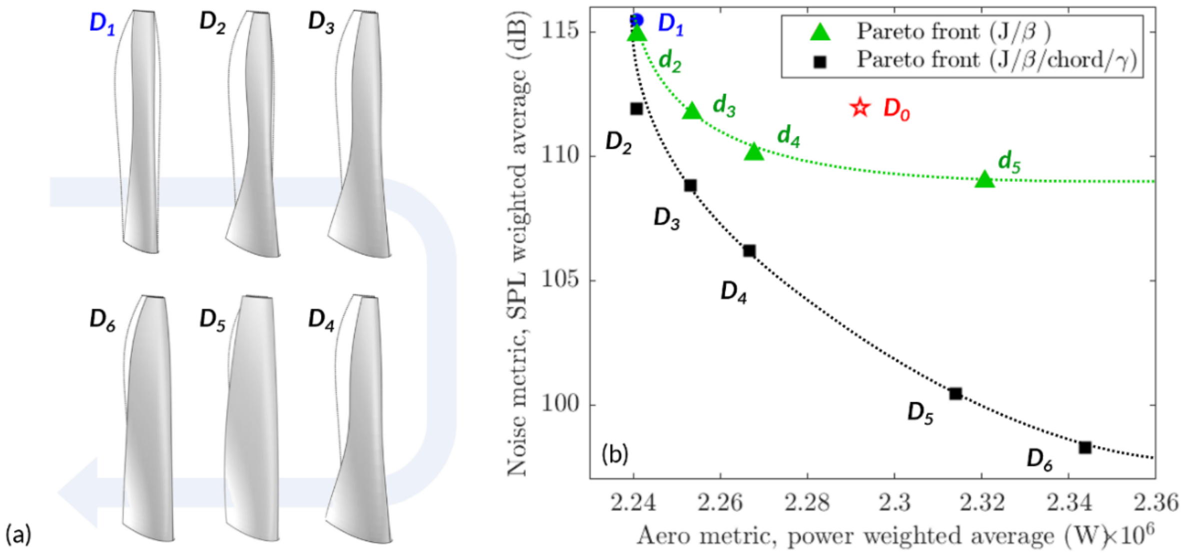

Figure 2.6: Blade shape optimisation (chord c, twist γ, advance ratio J, pitch β) pareto front. Blade geometries (a), noise/aerodynamic performances (b)

In the optimisation study by Margalida [36], the effect of reducing tip speed is clearly demonstrated as the dominant way to reduce propeller noise. As shown in Figure 2.6 two Pareto fronts were generated by incrementally increasing the weighting on noise reduction, providing a clear view of how the optimiser reduces noise while preserving performance. The optimiser reduces noise primarily by lowering the rotational speed, which affects all noise components via the tip Mach number. Chord and twist distributions are included as design parameters, and these are also adjusted to decrease the rotational speed further. Once this reduction is achieved, the optimiser employs an additional method for noise reduction: redistributing the spanwise load inward, where the sectional Mach number is lower.

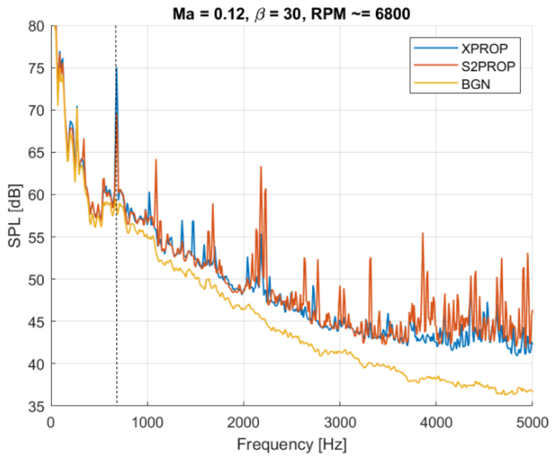

Figure 2.7: Results from measurements in the acoustic wind-tunnel for two different operating conditions. 6800 RPM on the left and 5800 RPM on the right. The measured background noise of the wind tunnel is also displayed as BGN. The dashed vertical line is the first blade passing frequency.

A subsequent study [40], comparing the resulting S2PROP propeller (optimised for noise and power required) with the starting XPROP propeller, showed that while the propeller produced significantly less noise, the perception of the noise of both propellers was quite the same. Looking at Figure 2.7 the tonal noise, the highest amplitude tonal frequency (which is the fundamental frequency) is significantly lower for the S2PROP compared to the XPROP. Presumably, this could be because of the human ear's insensitivity to lower frequencies and higher amplitude sound pressures at other frequencies of the S2PROP [40].

With an optimisation process that relies on the combined use of an artificial neural network metamodel, Marinus et al. [29] obtain a series of competing designs that reduce noise in their own way. With the design parameters of sweep distribution, twist, chord, thickness, and airfoil shape, the four-shaped blades in Figure 2.8 are the result.

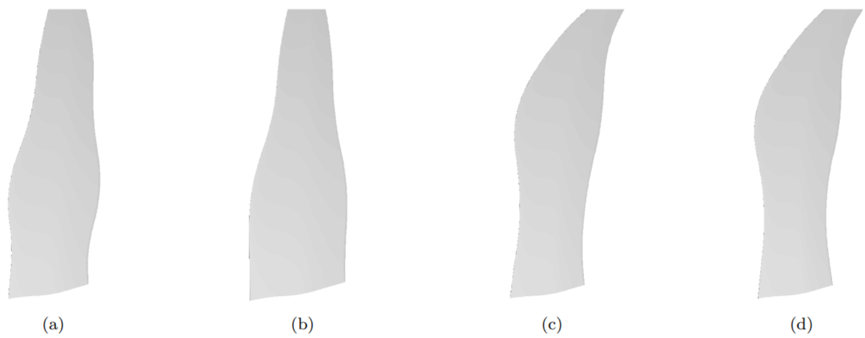

Figure 2.8: Blade geometry of the resulting optimised propellers

Spanwise interference does not necessarily need to be implemented through a standard sweep or chord distribution. In the study of Marinus et al. [38], an interesting effect is observed: "humps" in the chord distribution can also reduce noise at these lower harmonics which is also seen in other studies [41]. While it started as a way of reducing higher harmonics, the introduction of humps has been researched extensively afterward [42]. While the hump itself experiences a moderate load, the tips are, however, highly loaded. These humps are believed to reduce thickness noise by reducing the chord-to-diameter ratio near the tip.

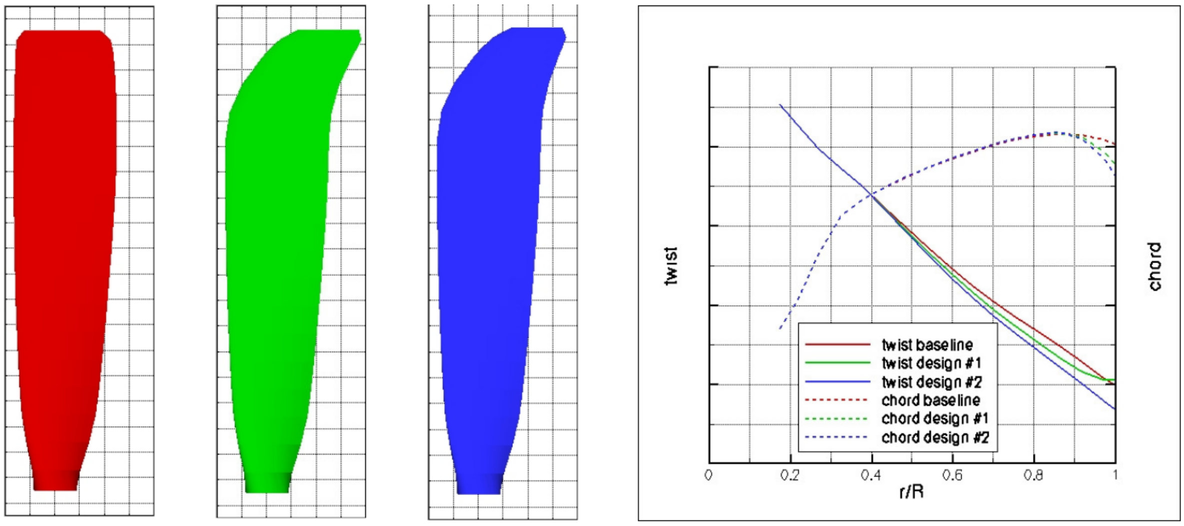

Figure 2.9: Comparison of blade geometries. Baseline (a), Design 1 (b), Design 2 (c) planforms; twist and chord distributions (d) [7]

Pagano et al. [7] details an optimisation approach aimed at reducing propeller noise and improving aerodynamic efficiency. This optimisation is applied to a propeller of the Piaggio P-180 aircraft, focusing on noise reduction during take-off and fuel efficiency during cruise. The results show how the optimised 6-bladed propeller achieves a Pareto front, reducing noise by 0.1 dB at the cost of only 0.2 percentage points on average. This is accomplished mainly by adding sweep to the tip while transferring the load from the tip by reducing tip sweep and chord as shown in Figure 2.9.

Looking at the optimisation problem that is solved. With two requirements on the thrust at Take-Off and cruise at a specified angular velocity, a multi-objective optimisation is chosen, targeting both noise and efficiency. Using an evolutionary algorithm, optimum blade designs are obtained. Within this optimisation, a Multi Disciplinary Analysis (MDA) iteration is used, coupling aerodynamics with structural modelling, to find the correct pitch to satisfy structural constraints. The outcome is fed into the aeroacoustic model for noise predictions.

The same effect is seen in [35].

2.5. HARMONICS

Tonal noise consists of a spectrum of frequencies with different amplitudes. These are harmonics of the blade passage frequency (BPF) and form the frequency envelope as shown in Figure 2.10. While usually, this fundamental frequency of 1xBPF dictates the majority of the tonal noise, all harmonics contribute. The more these harmonics dominate the sound spectrum, the more tonal noise can be reduced by reducing the noise of the harmonics. The tip rotational Mach number and the number of blades most significantly affect the frequency envelope shape [9], so these parameters will be the focus.

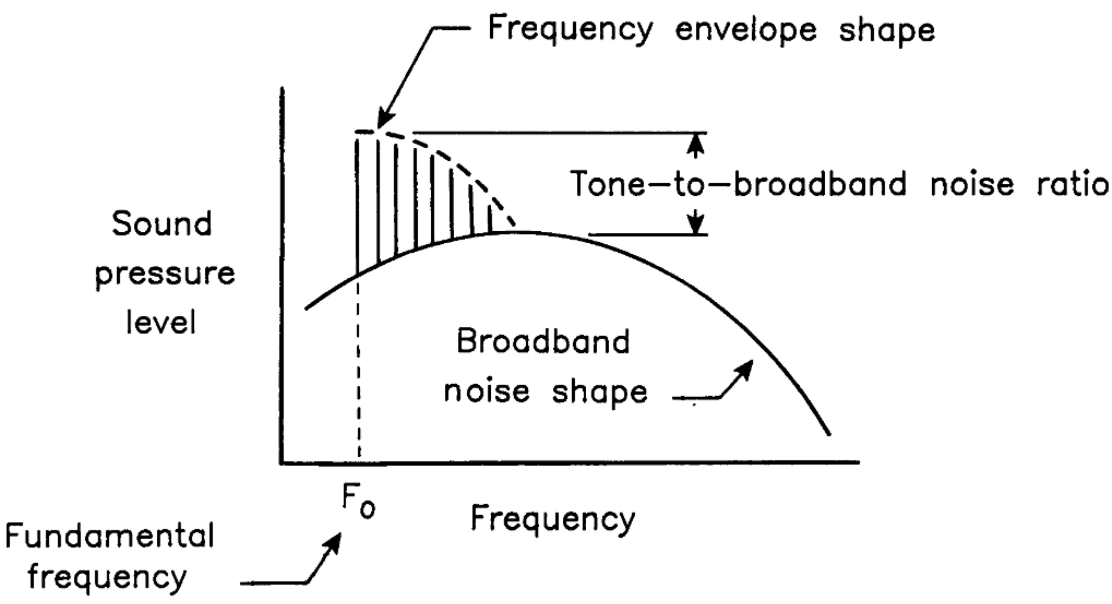

Figure 2.10: Noise characteristics of propeller aircraft [8]

BALANCE OF BROADBAND AND TONAL NOISE

For aeroacoustic analysis, the balance of broadband noise and tonal noise is important to take into account so that the dominant noise source for certain conditions can be predicted. Generally, a high relative tip Mach number and a low blade number cause tonal noise to dominate, while broadband noise becomes dominant under opposite conditions [9].

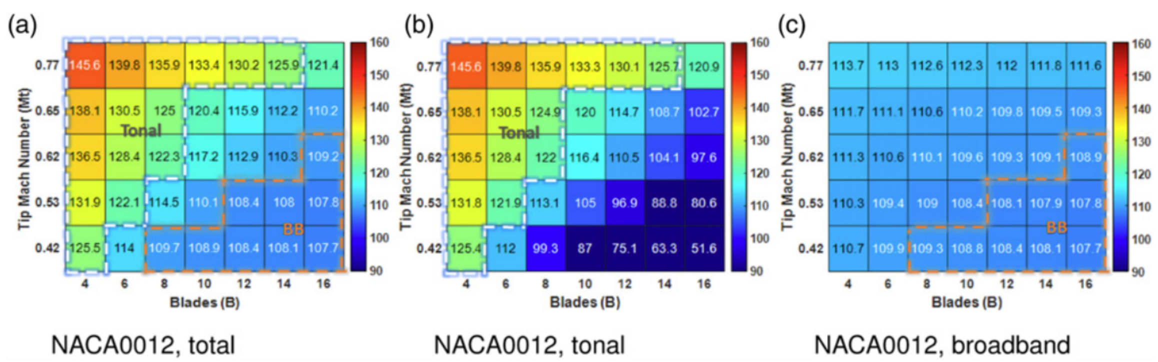

Figure 2.11: 2D plot representation of OSWL for NACA0012 airfoil geometry for tip Mach and blade number(a) total (b) tonal (c) broadband. [9]

In Figure 2.11 the noise predictions are presented that sum the tonal and broadband noise in OSWL (Overall Acoustic Sound Power Level) and show where in the domain of tip Mach number and blade number, if either tonal or broadband noise is dominant. The graph results are obtained from varying tip Mach number and blade number while maintaining the blade solidity and thrust. The parts where one of the noise sources is encircled are where it is more than 10 dB louder than the other noise type.

Effectively, for every propeller, there is a critical tip Mach number at which the level of tonal and broadband noise is identical, Figure 2.12. When analysing one of the noise types, it is important not to get too close to the critical Mach number, as the analysis may lose relevance due to the dominance of the other noise type. For tonal noise, this broadband noise acts as a floor for which the noise reduction method only has an effect until this value is reached.

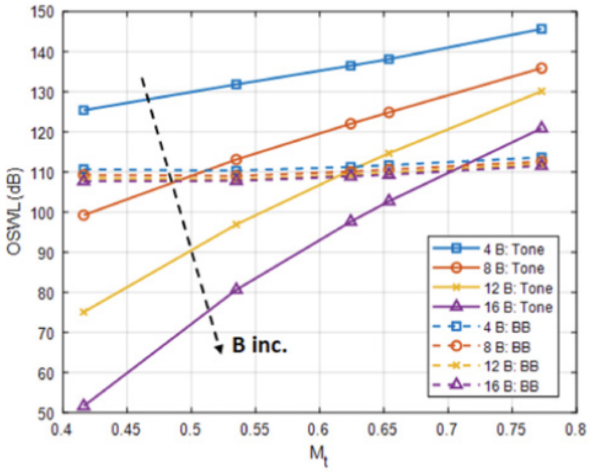

Figure 2.12: Tonal and Broadband OSWL against tip speed at different blade numbers for NACA0012 airfoil geometry. [9]

Figure 2.12 shows that tonal noise varies 70 dB in noise level with tip Mach number while the broadband noise only varies by 3 dB. This difference lies in the mechanism that these noise types generate noise [9]. As tonal noise consists of discrete frequencies that radiate with an efficiency determined by the Bessel function, this noise radiates more efficiently when the noise source is rotating at a higher frequency. As the solidity is kept constant for all results, the broadband noise does not vary much with the number of blades.

FREQUENCY ENVELOPE

Looking at the tip rotational Mach number, the shape of the frequency envelope flattens when the tip rotational Mach number M_t increases, as can be seen in Figure 2.13 meaning that with a higher rotational velocity while keeping the solidity, radius, and thrust the same, harmonics become more dominant in the tonal noise [6] [9].

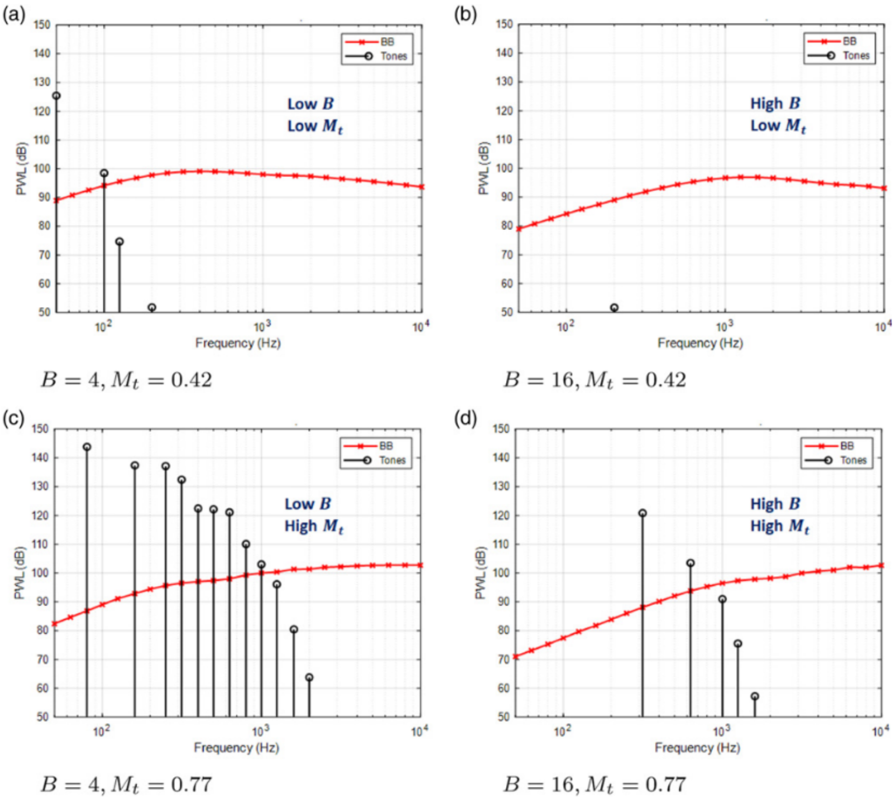

Figure 2.13: Sound power level (PWL) against frequency for extreme tip Mach numbers and blade numbers for NACA0012. (a) B = 4, Mt = 0.42, (b) B = 16, Mt = 0.42, (c) B = 4, Mt = 0.77, (d) B = 16, Mt = 0.77 [9]

The opposite is true for the number of blades. From the same figure (2.13 can be seen that when the number of blades increases, the frequency envelope steepens and thus the noise of the harmonics is reduced [9] [8].

NOISE REDUCTION BY REDUCING HARMONICS

As the phase lag increases with increasing harmonics number, the noise of these higher harmonics is reduced more. While being beneficial for the higher harmonics, this effect is subject to asymptotic behavior such that there is maximum noise reduction achieved by this phase lag [3]. Figure 1.3 shows this effect. 4 different harmonic numbers, m, are plotted by numerical calculation as well as the asymptote of m approaches infinity. The noise reduction grows quickly from the fundamental to the 3rd harmonic and quickly gets close to this asymptote.

$$\frac{P_m(swept)}{P_m(straight)} = \left\{1 + \frac{4M_t^2}{M_{rt}^2\left((1 - M_x cos\theta)^2\right) - M_t^2 sin^2} \times \left(\frac{tan\Lambda_t}{2} - \frac{s_t}{D}\frac{M_t^2}{M_{rt}^2}\right)^2\right\}^{-(\nu+1)/2} \tag{2.19}$$

This asymptote is formulated as Equation 2.19 [3]. It shows the noise reduction possible for the harmonic $m \to \infty$ for a propeller with sweep applied at the tip under sweep angle and Mid Chord Alignment, Λ_t and s_t, subject to the tip rotational, blade tip relative, and flight Mach number, M_t, M_{rt} and M_x, respectively. θ is the radiation angle for which its definition can be seen in Figure 2.5. D is the propeller diameter, and ν is a variable in using Laplace's method that can be put to zero at the tip. The derivation is done with Hanson's integral expressions, formulating the frequency-domain noise radiation [39] where the assumption of a "many-bladed propeller" ($B \gg 1$) is deemed to be of practical use at a number of blades of 4 and higher[3]. It calculates the noise reduction linearised at the tip as this is where noise is radiated from most efficiently and, thus, where most noise can be reduced. While this asymptote only gives accurate results for higher harmonics, it does give information about the operating conditions at which the added sweep will provide the most noise reduction and what the order of magnitude that can be.

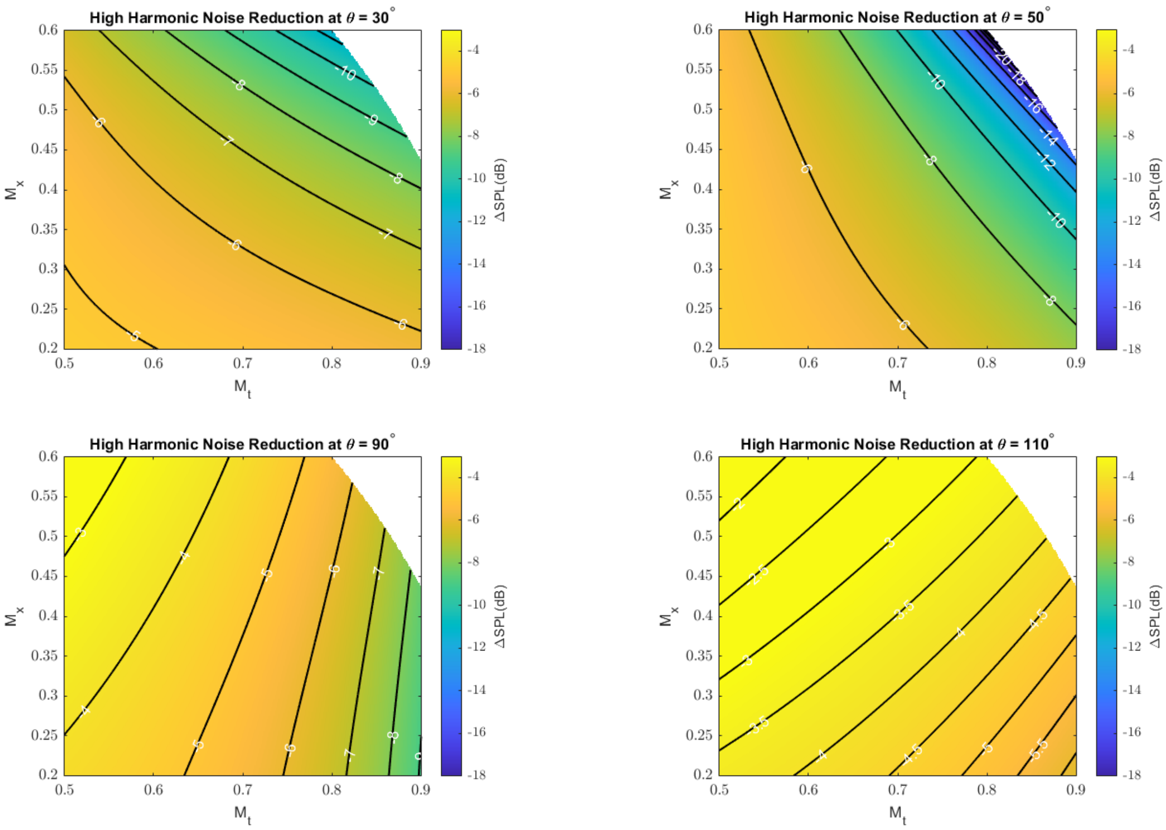

Figure 2.14: Asymptote of high harmonic noise reduction asymptote of 50-deg tip sweep blade at a range of operating conditions from Equation 2.19 (white part in graph where tip relative Mach number is greater than one.)

In Figure 2.14, Equation 2.19 is plotted for a blade with a 50-deg tip sweep with different radiation angles, θ. In this figure, values are excluded with a blade tip relative Mach number higher than one because the results are deemed irrelevant due to compressibility effects. The figure shows that noise reduction of higher harmonics due to sweep is most effective at a high flight Mach number or a high rotational Mach number, which differs through the radiation angle. What is interesting in these graphs is that the sensitivity of noise reduction to flight Mach number and tip rotational Mach number depends heavily on the radiation angle. For the the cases with a radiation angle of $\theta = 30°$ and $\theta = 50°$, the noise reduction increases with flight Mach number while for $\theta = 90°$ and $\theta = 110°$, noise reduction decreases with flight Mach number, although to a lesser extent.

Although these values predict the maximum achievable noise reduction of the harmonics, this does not say anything about how fast the accuracy of this equation rises with the harmonic number. But while the asymptote will remain the same for the number of blades, as the number of blades increases, the assumption of a "many-bladed propeller" gets more accurate, meaning that the lines of noise reduction for each harmonic will get closer to the asymptote, leading to more tonal noise reduction. Thus, for propellers with a higher number of blades, blade sweep leads to more noise reduction when following this reasoning.

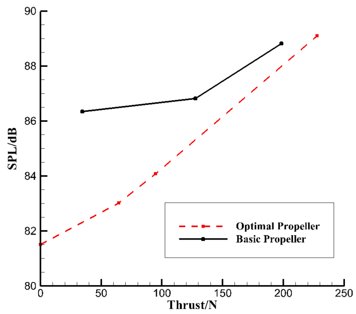

(a) Comparison at 1 BPF

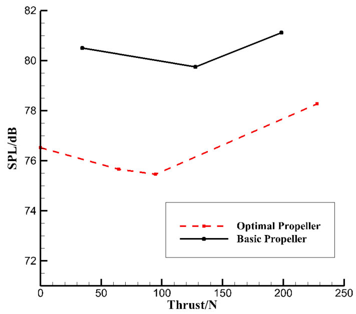

(b) Comparison at 2 BPF

Figure 2.15: Comparison of thrust–SPL between the basic and optimised propeller [10]

Another interesting effect is that the noise reduction of different frequency tonal noise responds differently to different levels of thrust[10]. In Figure 2.15, the noise reduction can be seen for the first and second BPF (fundamental and first harmonic), from a propeller optimised for noise (with the same efficiency) versus the starting propeller, which uses sweep as one of the design variables. While the noise reduction of the fundamental seems to be higher for lower levels of thrust, the reduction of the first harmonic sound level seems to be equal for different levels of thrust. While this does only contain one specific case, and thus the conclusions can not be generalised, it still raises the question of how different levels of thrust affect the effectiveness of reducing tonal noise with blade sweep because of the different ratio of loading noise to thickness noise. It is also noted that a constant noise level of the first harmonic may indicate a flaw that could invalidate these results.

2.6. AERODYNAMIC MODELLING

To predict the performance of propellers and the detailed loading on the blade, many models can be used that range from low-cost models for preliminary design, which can calculate results in milliseconds, to high-fidelity Computational Fluid Dynamics (CFD) simulations that solve the entire flow along the propeller can take days to weeks to obtain very accurate results. Four approaches are discussed: Blade Element Momentum (BEM) theory, Lifting Line Theory (LLT), the Vortex Lattice Method (VLM), and hybrid/CFD methods. As the author will make a choice to use a VLM method for this study, characteristics will be discussed of using VLM and the specific VLM model coupled with a structural model that is used from Ir. Jamie Thielen [15].

MODELLING METHODS

The Blade Element Momentum (BEM) theory combines one-dimensional momentum theory with blade element theory to provide a simple yet effective method for calculating propeller performance. Due to its low computational cost and relatively accurate results, BEM is widely used for (preliminary) design purposes using basic analysis. However, it has limitations as it assumes quasi-steady conditions, limited geometrical complexity, and does not account for aerodynamic interactions between adjacent blade elements [43]. Lifting Line Theory (LLT) and its extended forms, such as Weissinger's LLT, model the aerodynamic characteristics of propeller blades using vortex singularities, along the spanwise direction [43]. Just as BEM, LLT provides a simplified yet efficient representation of blade aerodynamics but includes the aerodynamic interaction between

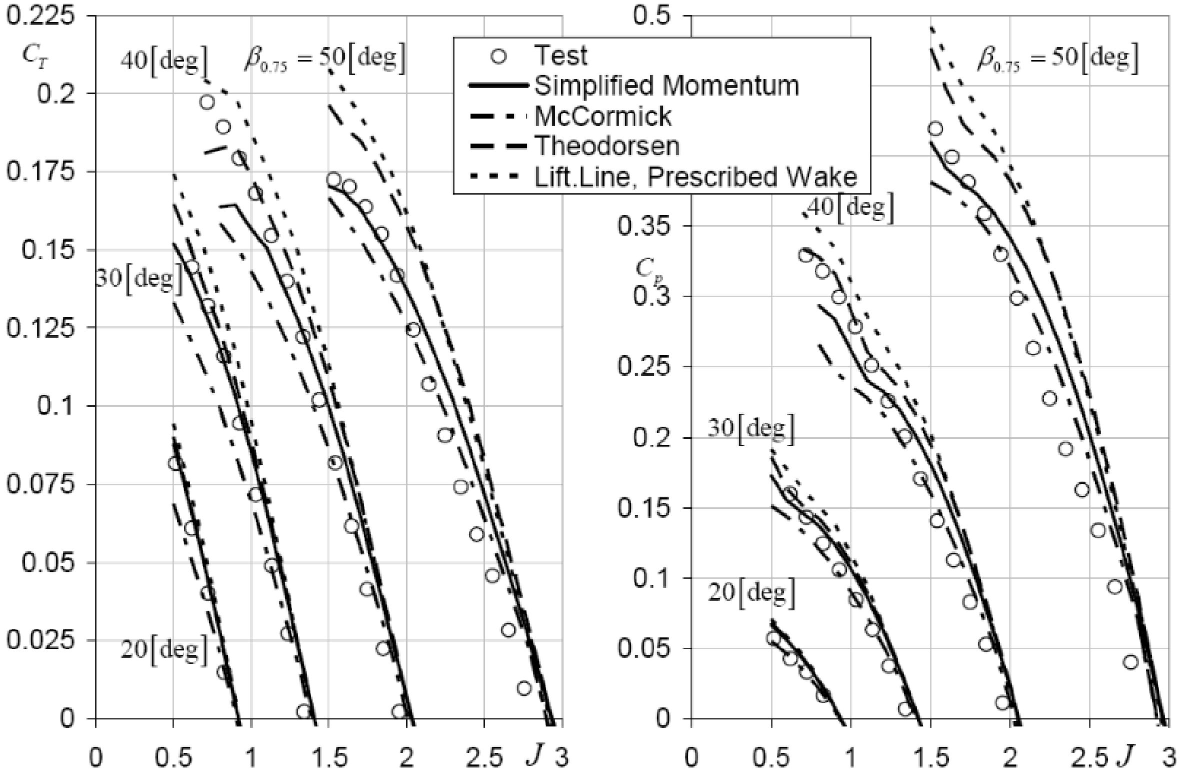

Figure 2.16: Comparison between the various BEM models (Simplified Momentum, McCormick and Theodorsen) and an LLT model and test results of a propeller having two swept blades [11], in axial flight [12]

blade elements, coming at the cost of some computational expense. While both methods do not capture three-dimensional flow effects, modifications can be done to both BEM and LLT to model blade sweep. Both BEM and LLT give great accuracy for small sweep or low load cases, but inaccuracies start to be introduced at high thrust or low advance ratio operations, as is shown in Figure 2.16.

Computational Fluid Dynamics (CFD) provides high-fidelity simulations of propeller flow fields by solving fluid dynamic equations for entire flows, including turbulence models such as Reynolds-Averaged Navier–Stokes (RANS), Large Eddy Simulation (LES), and Detached Eddy Simulation (DES). CFD methods offer detailed insights into unsteady and transient aerodynamic phenomena but suffer from high computational costs and grid-induced dissipation errors. To address these challenges, hybrid approaches integrating vortex methods with CFD have been developed, offering a balance between computational efficiency and accuracy. Furthermore, despite numerous enhancements aimed at increasing the efficiency of CFD methods, the significant computational expenses and the complex setup of equations continue to make these methods impractical for the analysis of a high number of different configurations in the same study [43].

Vortex Lattice Method

The Vortex Lattice Method (VLM) extends LLT by incorporating both chordwise and spanwise distributions of vortex ring elements to model the propeller blade's camber surface, explained in more detail in chapter 4. This method significantly improves the representation of three-dimensional aerodynamic effects compared to LLT. While LLT models use look-up tables to use the correct lift, drag (including profile drag), and momentum coefficients, VLM uses the 3D geometry of the blade, effectively using the camber line and chord length to determine its aerodynamics. As a VLM uses only the camber line in the blade cross-section, it does not account for blade thickness, thus being impractical when dealing with thick airfoils or modelling additional volumes like a fuselage. The source-doublet panel method improves upon VLM by including thickness effects and thus being able to model propellers with additional geometries and full rotorcraft [43]. While such panel methods are able to more accurately model complex geometric shapes, the algorithms used for these models take an order of magnitude longer to run, while standard VLM methods can still be used to give results of many configurations in an hour [44].

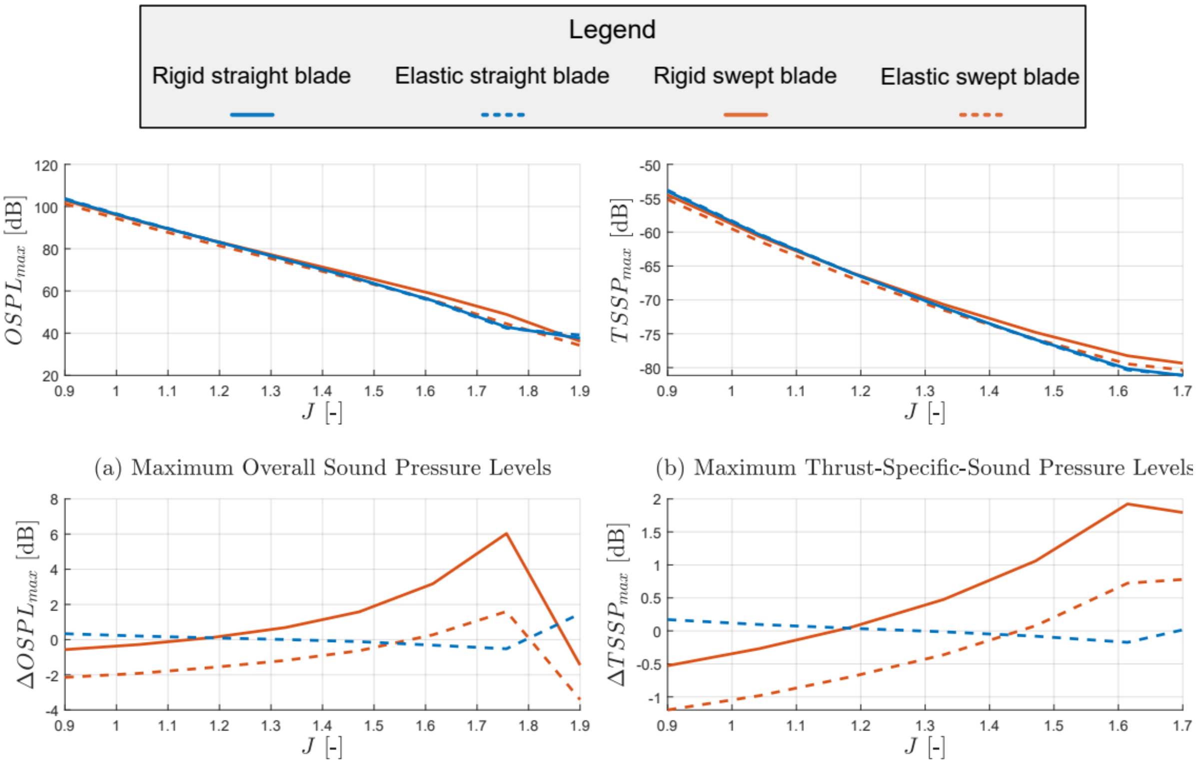

(a) Maximum Overall Sound Pressure Levels

(b) Maximum Thrust-Specific-Sound Pressure Levels

(c) Difference in maximum OSPL compared to the rigid straight blade

(d) Difference in maximum TSSP compared to the rigid straight blade

Figure 2.17: The acoustic performance of the rigid straight blade, elastic straight blade, rigid swept blade and elastic swept blade as a function of the advance ratio. The tip sweep of the swept blade has a value of 45°
[15]

ADDED AEROELASTICITY

Using a VLM, a propeller can be modelled with the 3d geometry of the blade surface, for which the loads can be calculated over the blade surface and coupled with a structural model to allow aeroelasticity to be taken into account. The highest deformation occurs at the tip, which is also the location where most noise is radiated from, and thus, aeroelasticity has a big impact on the interaction of aerodynamics and aeroacoustics [15].

Figure 2.17 presents the total noise emissions as a function of the advance ratio at a constant pitch, expressed in the $OSPL_{max}$ and $TSSP_{max}$ comparison between the results of a swept and straight blade, both modelled with and without taking into account the aeroelasticity. These metrics show the maximum value over the total range of radiation angle of the overall noise level and the maximum value of the overall noise level normalised by the reduction in thrust, respectively. Especially the lower figures about the difference in maximum noise level show interesting results, presenting the increase in noise production when comparing the resulting noise to that of the rigid straight blade.

As the advance ratio gets lower, the load increases, and so do structural deformations, especially at the tip where most noise is radiated from. The result is that for swept blades, the higher the loads are, the lower the noise that is generated, even when normalising the noise with the reduction of the thrust because of a lower lift blade tip. An opposite effect can be seen for a straight blade to a lesser extent. However, the remark has to be made that these results show the maximum value over all radiation angles and not the sound that is produced in the Overall Sound Pressure Level (OSPL), which more accurately represents the noise production. Looking at the high advance ratio case, the swept blade produces more noise than the straight blade, as in this study, the resulting thrust from the swept blade was higher than that of the straight blade. Comparing the increase in noise of the swept blade with and without aeroelastic modelling, a bigger difference can be noticed for increasing advance ratios, from about -1.8dB to +4.2dB.

II

Modelling

3

Propeller Parametrisation and Blade Discretisation

When modelling propellers, a suitable parametrisation must be adopted to define the propeller and its blades in a way that ensures compatibility with the models used and alignment with relevant literature. This parametrisation facilitates the generation of propeller geometries and their discretisation into a workable mesh. The chosen parametrisation and blade discretisation follow the modelling framework provided by Dr. G. Margalida's [13], as well as the aerodynamic and structural model implemented by Ir. J. Thielen within the same framework [15], supplemented by related literature.

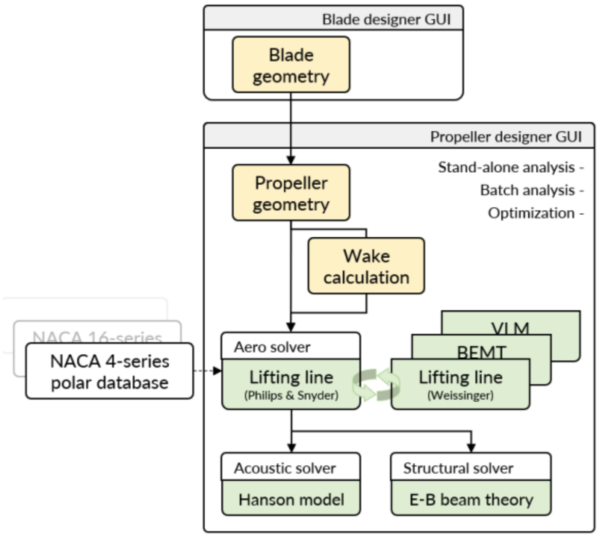

Figure 3.1: SmartRotor Framework for propeller analysis[13]

3.1. Propeller Parametrisation

The propeller design used in this study is defined through a set of global and blade-specific parameters. The global propeller parameters define the primary configuration of the propeller, while the blade section parameters describe how the shape of each blade evolves from root to tip in a normalised fashion such that, with the blade and global propeller parameters, the entire propeller is defined. The details of this parametrisation are outlined below:

Global Propeller Parameters

- R_p: Propeller radius

- N_b: Number of blades
- $\beta_{0.7}$: Blade pitch angle at $0.7R_p$
- R_{hub}: Hub radius (starting point for all blade parameter distributions)

Blade Section Parameters All parameters below are defined as spanwise distributions along the blade

- c/R_p: Normalized chord length
- γ: Local twist angle relative to $\beta_{0.7}$
- t/c: Maximum thickness-to-chord ratio
- d/c: Maximum camber-to-chord ratio
- x/c: Chordwise position of maximum camber
- Sweep:
  - MCA: Mid-chord alignment (see Figure 3.2)
  - Λ: Sweep angle between mid-chord line and X-X axis
- Lean: Face alignment (FA) distance between chordline and rotation plane (definition similar to MCA, shown in Figure 3.2)

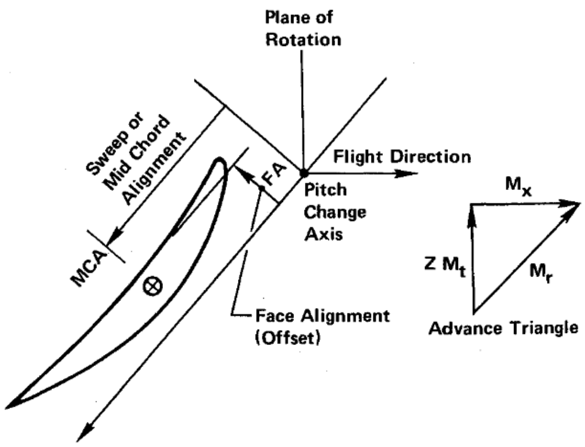

Figure 3.2: Blade Sweep definition, Mid Chord Alignment (MCA)

All blade parameters are defined as spanwise distributions along the chord, with their spatial variation specified at each blade location as illustrated in Figure 3.3. When combined with the global propeller parameters, these distributions completely define the propeller geometry. These parameter distributions serve as the baseline blade design for this study.

The parameter distributions are implemented using Bézier curves, following the same parametrisation approach as the SmartRotor framework. As shown in Figure 3.4, each distribution is defined by four control points with six governing parameters. Points p_1 and p_4 have reduced degrees of freedom since they are constrained at the hub and tip, respectively. For both hub and tip locations, the parametrisation specifies:

- The absolute parameter values
- The Bézier curve angle (first derivative)
- The curve "tension" (proportional to the second derivative)

3.2. DISCRETISATION

The geometry is discretised to generate meshes suitable for both aerodynamic and structural analyses. Two parameters control this discretisation:

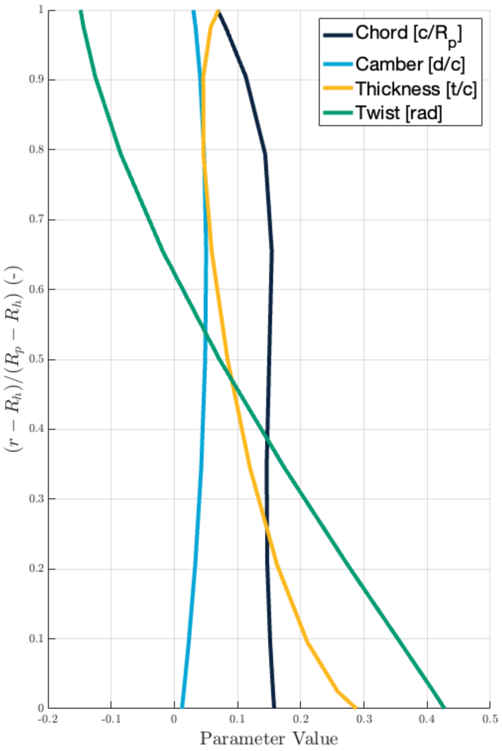

Figure 3.3: Parameter Distribution of XPROP blade (with MCA and FA are zero over the entire blade span

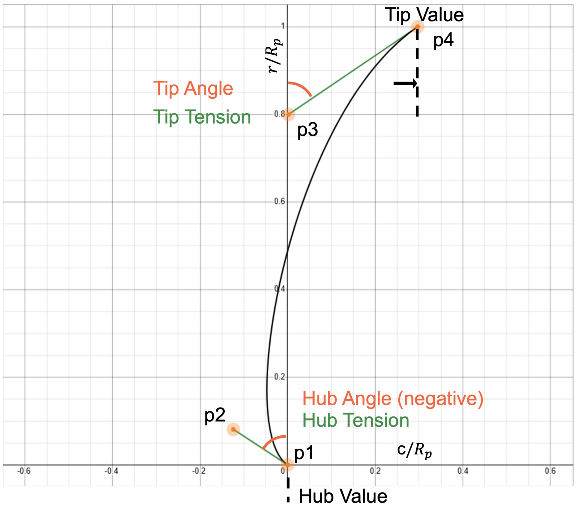

Figure 3.4: Parametrisation of parameter blade distribution Bézier curves

- N_s: Number of spanwise control points
- N_c: Number of chordwise control points

Figure 3.5 and Figure 3.6 illustrate the resulting blade and propeller geometries generated from these parameters. The latter figure demonstrates two distinct mesh types:

- A surface mesh for the Vortex Lattice Method (VLM) aerodynamic model, which neglects thickness effects
- An upper and lower surface mesh for the Euler-Bernoulli beam structural model, which incorporates thickness

The airfoil geometry is generated using a NACA-based parametric function that computes the camber line shape and the thickness distribution with the corresponding blade parameter distributions.

The Smartrotor framework, originally developed by Dr. G. Margalida, has been adapted to incorporate the Vortex Lattice Method implementation by Ir. J. Thielen. This integration enables coupled aerodynamic, aeroacoustic, and structural analysis, the aerodynamic modelling of which is detailed in the following chapter.

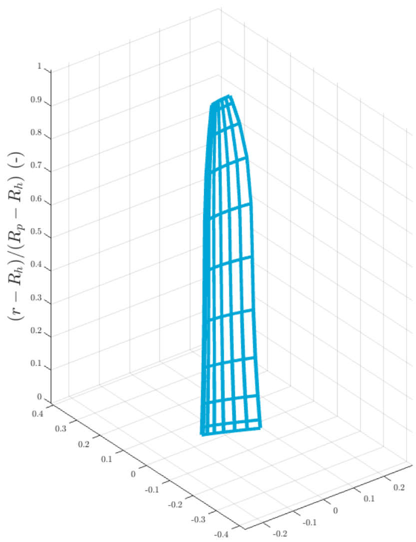

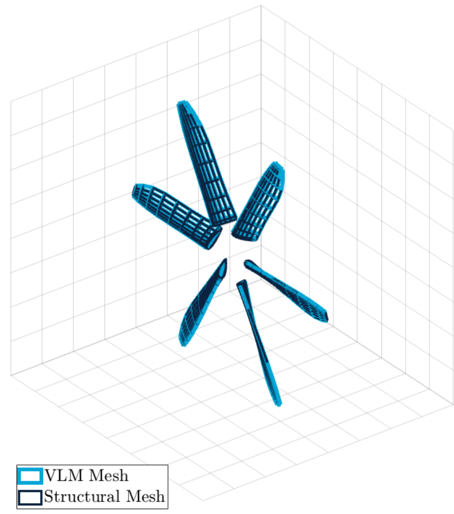

Figure 3.5: Exemplary blade discretisation of the XPROP blade, used for the VLM aerodynamic model

Figure 3.6: Exemplary propeller discretisation of the XPROP propeller for the aerodynamic and structural model

4

AERODYNAMIC MODELLING

Choosing an aerodynamic model requires balancing computational efficiency for optimisation and accurate sweep modelling. Since this study involves multiple optimisations with numerous function evaluations, only low-fidelity models with runtimes in the order of seconds to minutes are suitable. Consequently, high-fidelity methods such as Computational Fluid Dynamics (CFD) and Vortex Particle Methods (VPM) are excluded due to excessive computational costs. Blade Element Theory (BET), with a sweep correction, remains accurate only for high advance ratios and low sweep angles [45, 46]. While the Lifting-Line Method (LLM) provides a better representation of sweep effects, it cannot fully capture complex geometries at high sweep angles due to its inherently one-dimensional nature. Therefore, the Vortex Lattice Method (VLM) is chosen, as it can handle more intricate blade shapes and provide detailed two-dimensional load distributions along the blade.

4.1. VLM

The Vortex Lattice Method (VLM) for aerodynamic propeller analysis that is used in this study is developed by Ir. J. Thielen [15] by implementing the 3D panel method from Katz and Plotkin's "Low-Speed Aerodynamics" (Chapter 12) using the Smart Rotor Framework [13] as a foundation. Additional functionality is added to complete the propeller model from the model of a fixed wing. Extra velocity due to the propeller rotation and a wake model complete the propeller model.

The VLM is based on potential flow theory and operates under the following assumptions:

- Inviscid
- Incompressible
- Irrotational
- Steady-State flow field

The blade geometry is built out of an $N_S \times N_C$ lattice that can represent a complex geometry in a three-dimensional space through a 2D curved surface. This enables modelling of all blade geometric parameters that don't require blade thickness. This means that aerodynamically, blade thickness and airfoil shape (except for the camber line) cannot be modelled.

Each panel on the discretised propeller blade and wake elements contains vortex rings of strength Γ_k at all collation points with a vortex ring element that surrounds that panel. For propeller analysis, these rings consist of four straight vortex line segments with constant vorticity. Its location is shifted a quarter panel towards the trailing edge as shown in Figure 4.1 in order for a system to be made to impose the boundary conditions and calculate the potential flow.

The Neumann boundary condition is applied at all the collocation points, ensuring zero normal velocity at the camber line to ensure tangential flow along the airfoil. The normal velocity at each collocation point results from the freestream velocity and the induced velocities from the vortex rings. The freestream contribution consists of axial (U_∞) and tangential ($V_t = \Omega \times r$) components, while the induced velocity is derived

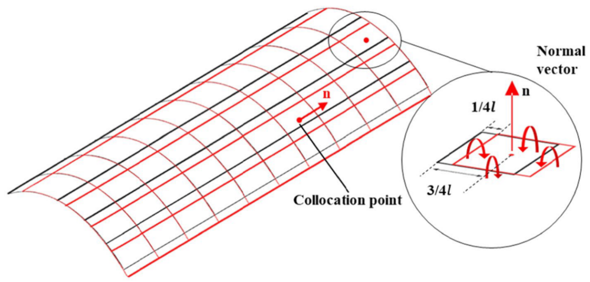

Figure 4.1: VLM vortex ring model for a cambered Lifting Surface [14]

from all vortex rings in the lattice. The governing equation at a collocation point is given by:

$$(\nabla\phi + \mathbf{V}) \cdot \mathbf{n} = 0 \tag{4.1}$$

To enforce the Kutta condition, ensuring zero vorticity at the trailing edge, a wake extends into the far field. A fixed-wake model is used where the wake panels are placed on helicoidal sheets determined by operating conditions (inflow and rotational velocities). In a more realistic model, the helicoidal sheet depends on the induced velocity, and such sheets tend to roll up near the blade tips. In this case, a fixed wake has been shown to be sufficient in symmetric flight. The circulation strength at the trailing edge vortex line defines the circulation of the wake panels such that the Kutta condition is met at the trailing edge.

A linear system is formed by applying the boundary condition at all collocation points, Equation 4.2. This system accounts for the influence of the circulation (Γ_k) every panel (i) on every other panel (j) by influence coefficient $\alpha_{i,j}$ as in Equation 4.3. The right hand side (RHS_k) equals the relative imposed airflow at that point in the direction of the panel normal vector shown in Equation 4.4. Solving this system yields the circulation distribution (Γ_1 to Γ_m). From the circulation, the (induced) lift and drag are then computed using the Kutta-Joukowski theorem.

$$\begin{bmatrix} a_{11} & a_{12} & \cdots & a_{1m} \\ a_{21} & a_{22} & \cdots & a_{2m} \\ \vdots & \vdots & \ddots & \vdots \\ a_{m1} & a_{m2} & \cdots & a_{mm} \end{bmatrix} \begin{Bmatrix} \Gamma_1 \\ \Gamma_2 \\ \vdots \\ \Gamma_m \end{Bmatrix} = \begin{Bmatrix} \text{RHS}_1 \\ \text{RHS}_2 \\ \vdots \\ \text{RHS}_m \end{Bmatrix} \tag{4.2}$$

$$a_{ij} = (\mathbf{V}_{\text{ind,bound}})_{ij} \cdot \mathbf{n}_i \tag{4.3}$$

$$\text{RHS}_i = -(\mathbf{V}_\infty + \mathbf{V}_{\text{ind,wake}} - \boldsymbol{\Omega} \times \mathbf{r})_i \cdot \mathbf{n}_i \tag{4.4}$$

4.2. VISCOSITY MODEL

Since the VLM does not use lift polars, only induced lift and drag are calculated when solving the system of equations. While this is not an issue for calculating load distributions, it becomes problematic when induced drag is not the dominant factor, and profile drag plays a significant role. This could particularly affect optimisations, where minimising power is used in an objective function in chapter 11. To address this, the VLM model incorporates a viscous model based on a semi-infinite flat plate [47]. The equation for this viscosity model is given in Equation 4.5.

$$C_D = 1.328\,\text{Re}^{-1/2} + 2.326\,\text{Re}^{-1} \tag{4.5}$$

4.3. BLADE DISCRETISATION

To determine the blade discretisation, appropriate values for the number of spanwise (N_s), chordwise (N_c), and wake (N_w) points must be selected to ensure sufficient resolution for both aerodynamic and aeroacoustic predictions.

Two discretisation levels are chosen: a low-resolution discretisation for the optimisation study, ensuring accurate estimation of thrust, noise, and blade loading for the structural model, and a high-fidelity discretisation for the parametric study. The latter allows for increased computational cost, as fewer simulations are required, while providing additional resolution to capture higher harmonics accurately, necessitating finer spanwise discretisation.

The choice of discretisation is based on the convergence of the thrust coefficient (C_T) and Overall Sound Pressure Level (OSPL), as shown in Figures 4.2 and 4.3. Additionally, the convergence of the Sound Pressure Level (SPL) of the highest harmonic is considered under conditions where achieving accuracy is most challenging, Figure 4.4.

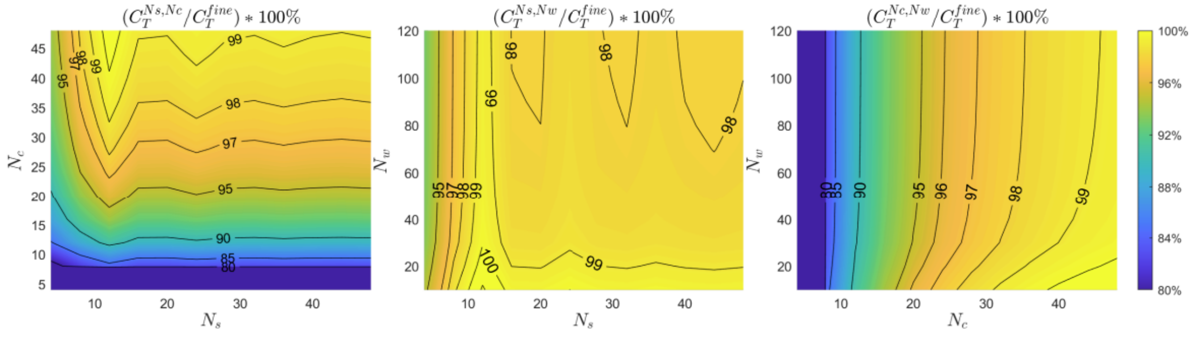

(a) N_s vs N_c (b) N_s vs N_w (c) N_c vs N_w

Figure 4.2: Grid convergence of the VLM tool for all three grid parameters [15]

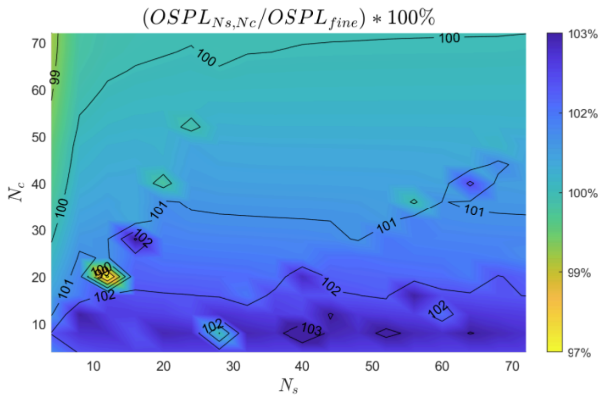

Figure 4.3: Grid convergence of the acoustic tool for N_s and N_c [15]

Discretisation choice

Purpose	N_s	N_c	N_w
Aeroacoustics	25	25	40

Table 4.1: Discretisation used in this study

It is crucial to obtain accurate load distribution, thrust coefficient, and noise prediction for the highest harmonic, which is determined by the aeroacoustic model. The highest harmonic dictates the number of control points along the span, as its total noise level of this harmonic results from the vector sum of noise contributions along the span, all with a different phase [6]. A graphical representation of two configuration choices is shown in Figure 4.4.

For aerodynamic accuracy, a 95% convergence threshold is considered acceptable, suggesting values of N_s = 10, N_c = 25, and N_w = 40 based on Figure 4.2. However, accurately capturing all harmonics requires a higher N_s. Therefore, N_s = 25 is chosen to ensure reliable results for the highest harmonic as shown in Figure 4.4.

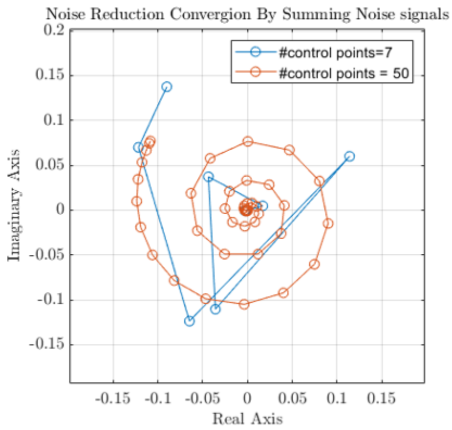

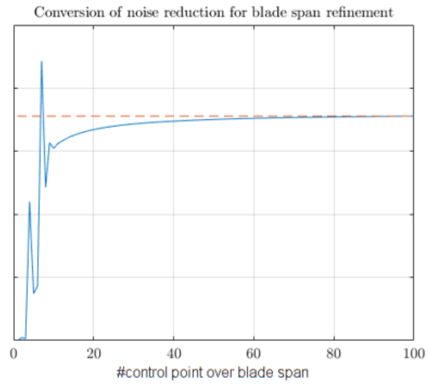

Figure 4.4: Left, graphical representation of noise reduction of the 7th harmonic. Right, the analytic solution to the noise level convergence of the 7th harmonic for determining the number of panels over the blade. Tip sweep = 45deg, Mt = 0.8, Mx = 0.2, B=6 [15]

4.4. ASSUMPTIONS AND LIMITATIONS OF THE VORTEX LATTICE METHOD

While the VLM offers computational efficiency and reasonable accuracy for certain applications, it is based on several simplifying assumptions that limit its applicability. The primary assumptions and their implications are outlined below:

- Incompressible Flow Assumption: The method presumes incompressible flow, which limits its accuracy at higher Mach numbers where compressibility effects become significant. This restricts its use to low-speed aerodynamic analyses.
- Irrotational and Steady Flow Assumption: VLM is based on potential flow theory, assuming the flow is irrotational and steady. It cannot capture unsteady aerodynamic phenomena such as dynamic stall or transient wake effects.
- Thin Lifting Surfaces: The method models lifting surfaces as infinitely thin, neglecting thickness effects. This simplification can lead to inaccuracies in predicting pressure distributions and aerodynamic forces for thick airfoils

With the discretisation chosen before, it provides sufficient accuracy for both aerodynamic analysis via VLM and aeroacoustic predictions using Hanson's tonal noise model. The aerodynamic results feed into this aeroacoustic model that is detailed in the next chapter.

5

Aeroacoustic Modeling

To model the noise produced by the propeller, Hanson's helicoidal surface model for far-field noise is used [39]. This model combines aerodynamic input from the VLM (Vortex Lattice Method) with the geometrical characteristics of the propeller to predict the sound pressure levels for each harmonic and direction. These predictions form the basis for calculating the overall sound pressure level (OSPL) and for incorporating human noise perception effects. By applying a frequency-dependent filter that mimics the human auditory response, the Perceived Noise Level (PNL) is obtained. A time integration over the event then yields the Effective Perceived Noise Level (EPNL), as defined in aircraft noise certification standards [2].

5.1. Hanson's Helicoidal Theory

Hanson's Helicoidal Noise Model, based on the Helicoidal Surface Theory (HST) [39], provides a method for predicting the acoustic noise generated by propellers. This theory models the blades as advancing helicoidal surfaces, where the blade surface is swept out by a radial line that both rotates at an angular speed Ω and translates with the freestream velocity. This motion results in the formation of a helical coordinate system in which the blade's path is determined by both its rotational speed and the translational motion through the air. This allows sweep, and other parameters that make use of so-called "non-compactness" to give an accurate insight into aeroacoustics and thus can be used to give results to this study. For clarity, parameters used in the equations in this model are listed below:

- $p(t)$: Pressure as a function of time
- P_{mN_b} : Fourier coefficient of pressure at the m-th harmonic of blade-passage frequency for a propeller with N_b blades
- Ω : Rotational speed of the propeller
- t : Time
- ρ : Air density
- c_0 : ambient speed of sound
- N_b : Number of blades in the propeller
- θ : Radiation angle
- M_x : Mach number of the aircraft
- r : Radial position on the blade
- D : Diameter of the propeller
- ϕ_0,ϕ_s : Phase shift due to respectively offset and sweep
- M_t : Tip rotational Mach Number

- M_r : Local relative Mach Number = $\sqrt{M_x^2 + (\frac{r}{R_p})^2 M_t^2}$
- $\Psi_V(k_x)$, $\Psi_D(k_x)$, $\Psi_L(k_x)$: Normalized source transforms of respectively thickness noise, drag noise and lift noise.
- J_{mN_b} : Bessel function of the first kind
- k_x, k_y : Local, dimensionless wave numbers where k_x is the chordwise wave number.
- FA : Face alignment, perpendicular distance between pitch change axis and chord line
- MCA : Mid-chord alignment, distance from pitch change axis to midchord
- C_D : Section drag coefficient
- C_L : lift coefficient
- $H(X)$: Normalized thickness distribution

The noise generated by these blades is calculated by considering the pressure wavefront experienced by an observer. In the model, this pressure is described using a Fourier series, which breaks down the acoustic signal into its harmonic components with frequency $N_b\Omega$ and amplitude P_{mN_b} with three different source components, P_{Vm}, P_{Dm}, and P_{Dm}, respectively, for thickness, drag and lift noise. The same can be done for components of thrust and torque noise as shown in Equation 5.2.

$$p(t) = \sum_{m=-\infty}^{\infty} P_{mN_b} e^{-imN_b\Omega t} \tag{5.1}$$

These components consist of an imaginary and a real part to take into account the phase of the sound waves. In this way, constructive and destructive interference can be predicted.

$$P_{mN_b} = P_{Vm} + P_{Lm} + P_{Dm} = P_{Vm} + P_{Tm} + P_{Qm} \tag{5.2}$$

The following equations show what calculations are done to output the noise components. Equation 5.3 shows the main equation to obtain them.

$$\begin{aligned} \begin{Bmatrix} P_{Vm} \\ P_{Dm} \\ P_{Lm} \end{Bmatrix} &= -\frac{\rho c_0^2 N_b \sin\theta \exp\left(imN_b\left(\frac{\Omega r}{c_0} - \frac{\pi}{2}\right)\right)}{\pi(y_0/D)(1 - M_x\cos\theta)} \int_0^1 M_r^2 e^{i\phi_0 + \phi_s} \\ &\times J_{mN_b}\left(\frac{mN_b(r/R)M_t \sin\theta}{1 - M_x\cos\theta}\right) \begin{Bmatrix} k_x^2 t_b \Psi_V(k_x) \\ ik_x \frac{C_D}{2} \Psi_D(k_x) \\ ik_y \frac{C_L}{2} \Psi_L(k_x) d\left(\frac{r}{R}\right) \end{Bmatrix} \end{aligned} \tag{5.3}$$

Equation 5.4 shows the Fourier transforms of the thickness and loading distributions in the chordwise direction. These distributions are normalised such that the maximum value is 1 and defined from -0.5 to +0.5 of the propeller pitch axis as shown in Figure 5.1 .

$$\begin{Bmatrix} \Psi_V(k_x) \\ \Psi_D(k_x) \\ \Psi_L(k_x) \end{Bmatrix} = \int_{-\frac{1}{2}}^{-\frac{1}{2}} \begin{Bmatrix} H(X) \\ f_D(X) \\ f_L(X) \end{Bmatrix} e^{ik_x X} dX \tag{5.4}$$

The phase lag due to offset and sweep, ϕ_o , ϕ_s are defined in Equation 5.6. Using the integral in Equation 5.3 the interference of same frequency sound by means of spacial dis-alignment of the sound waves. The wave number k_x, and k_y are calculated in Equation 5.8. The parameters can be used to measure non-compactness of the propeller sound, which can be used for noise reduction as well.

$$\phi_s = \frac{2mN_b M_T}{M_r(1 - M_x\cos\theta)} \frac{MCA}{D} \tag{5.5}$$

$$\phi_0 = \frac{2mN_b}{(r/R)M_r} \left(\frac{M_T^2\cos\theta - M_x}{1 - M_x\cos\theta}\right) \frac{FA}{D} \tag{5.6}$$

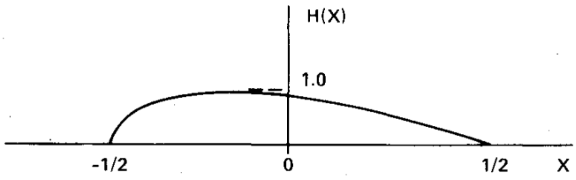

Figure 5.1: Normalized thickness distribution

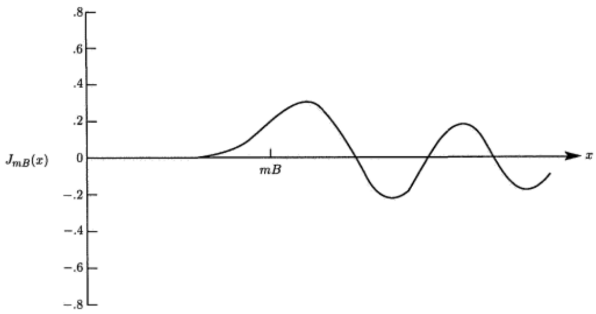

Figure 5.2: Bessel function behaviour in Hansons Helicoidal Model where $mB = mN_b$ is the harmonic number

$$k_x = \frac{2mN_b B_D M_t}{M_r(1 - M_x cos\theta)} \tag{5.7}$$

$$k_y = \frac{2mN_b B_D M_t}{(r/R)M_r}\left(\frac{M_r^2 cos\theta - M_x}{1 - M_x cos\theta}\right) \tag{5.8}$$

In Equation 5.3, the term J_{mN_b} represents the Bessel Function, with as argument, the term between brackets of which its behaviour is shown exemplary in Figure 5.2. It modulates how sound is radiated under the various observation angles.

5.2. CALCULATING (OVERALL) SOUND PRESSURE LEVEL

Calculating the Sound Pressure Level (SPL) and Overall Sound Pressure Level (OSPL) is done from the sound components, P by taking the base-10 logarithm of twice the absolute value divided by a reference pressure threshold of human hearing, p_{ref} (=2e-5[Pa]), Equation 5.11. The value is taken twice as the total amplitude of sound is calculated, while the value of P_{mN_b} only determines halve that value. In this way, only the SPL of a single frequency is obtained at one observer angle, (SPL_m).

$$\text{SPL}_m = 20\log_{10}\left(\frac{2|P_{mN_b}|}{p_\text{ref}}\right) \tag{5.9}$$

$$\text{OSPL} = 20\log_{10}\left(\sqrt{\sum_m \left(2\frac{|P_{mN_b}|^2}{p_\text{ref}}\right)}\right) \tag{5.10}$$

$$\tag{5.11}$$

To obtain the Overall Sound Pressure Level (OSPL) of the whole noise spectrum (at a single observation angle), the root mean square of all frequency sound levels are taken, shown in Equation 5.13. For the parameter study, the root mean square of the Overall Perceived Noise Level (OSPL) is used as a rough approximation of the time-integrated noise metric, EPNL, obtaining $OSPL^{RMS}$. The same calculations can be done for single-frequency noise levels, obtaining SPL_m^{RMS}. This is done in a similar way to computing the OSPL itself, where the noise levels are weighted by the fraction of directivity the signal adheres to.

$$P_{OSPL}^2 = \sum_i \sum_m 2^2 \frac{|P_{mN_b}|^2}{p_{ref}}(\theta_i)\frac{\Delta\theta}{\theta_{range}} \tag{5.12}$$

$$OSPL^{RMS} = 20log_{10}\left(2\frac{|P_{OSPL}|}{p_{ref}}\right) \tag{5.13}$$

A similar approach is used when calculating values of perceived noise level (PNL), which will be used in the following section.

5.3. EPNL CALCULATION

Effective Perceived Noise Level (EPNL) is the primary metric used for aircraft noise certification, as defined by ICAO Annex 16 Volume 1 [2]. It builds upon the Perceived Noise Level (PNL) by incorporating both the duration of the noise event and penalties for tonal components, which are more annoying to the human ear. EPNL is expressed in decibels (EPNdB) and provides a single-number measure that reflects how humans perceive aircraft noise during a flyover. In this study, the use of dB instead of EPNdB will be used for easier comparison. Calculating EPNL involves integrating the time-varying PNL over the duration of the noise event, applying duration corrections, and adding tone corrections when tonal content is detected.

NUMERICAL ANALYSIS OF EPNL

Calculating the effective perceived noise level for aircraft from a recording, a spectrum analysis is done for every 0.5 seconds of recording, with which the following 5 steps are taken to calculate the level of EPNL:

1. Convert 24 one-third octave band sound levels to perceived noisiness (noy), then to instantaneous perceived noise level PNL.
2. Calculate tone correction for each spectrum.
3. Add tone correction to obtain tone-corrected perceived noise levels to obtain PNLT and determine the maximum value PNLTM.
4. Compute the duration correction factor D by integrating PNLT over time for all noise higher than 10[dB] beneath PNLTM.
5. Calculate effective perceived noise level (EPNL) by adding the duration correction factor D to the maximum perceived noise level PNLTM.

The values of the perceived noise level (PNL) that are approximated have to be tone corrected for the spectral irregularities. As in this study, a numerical approach is taken, the frequencies are analytically determined by the harmonic number (and the Doppler effect), and thus no spectral irregularities are present. This means that no tone correction has to be done and a simpler approach can be taken, integrating the levels of PNL over any value of dt (which does not have to be the 0.5 seconds specified in regulations) [48].

An extra step that is introduced in this study for the calculation of the PNL is the interpolation of the conversion tables to convert levels of SPL to Perceived Noisiness in Noys. To calculate the PNL, in the first step, the noise spectra are all converted into 24 one-third octave bands, which is done to analyse continuous noise spectra. These bands will all have different weightings put to the sound levels according to the mid-frequency in the respective frequency band. As in this study, only sound spectra are present with discrete frequencies, the PNL conversion using these bands is avoided for two reasons. First, as an optimisation will be performed in this study, such discrete weightings to certain bands could mess with the optimisation gradients when, due to a change in harmonic number, an important frequency shifts to a band with another sound amplification weight. Secondly, this will provide a fairer outcome as the optimisation algorithm will not use such an analysis to its advantage, as in real life, an aircraft would not be able to.

With these two adjustments, a new set of steps is made to convert the levels of SPL to EPNL:

1. Interpolate conversion table data to fit the frequency and amplitude of the input sound wave.
2. Convert SPL first to Perceived noisiness (noy) with interpolated table data and then to PNL with Equation 5.14.

3. Determine maximum PNL value: PNLM.
4. Obtain the first and last time value , t_1, and t_2, with a PNL of higher than PNLM - 10[dB].
5. Calculate effective perceived noise level (EPNL) by integrating the PNL from t_1 to t_2 with Equation 5.15.

$$PNL(k) = 40 + \frac{10}{\log_{10}(2)} \cdot \log_{10}(N_k) \tag{5.14}$$

$$\text{EPNL} = 10 \log \frac{1}{t_0} \int_{t_1}^{t_2} 10^{0.1\,\text{PNLT}(t)} \, dt \tag{5.15}$$

5.4. ASSUMPTIONS AND LIMITATIONS

The noise modelling in this study relies on Hanson's Helicoidal Model for far-field noise prediction, which is used to estimate tonal noise components produced by the propeller, which comes with some limitations and assumptions that have to be made. In the calculation of Effective Perceived Noise Level (EPNL), several assumptions and limitations are inherent to the approach. They are the following:

Assumptions:

- Tonal noise is dominating the noise spectrum and consists of loading and thickness noise only
- Quadrupole sound will not be dominating and thus is not modelled
- Human noise perception can be modelled quantitatively through modification of the noise levels as written down in certification [49]

Limitations:

- Noise cancellation is over-predicted as shown in experimental studies.
- Near field noise prediction is not effective and not usable under a distance of 3-4 and lower harmonics [50].
- Broadband noise is not taken into account

This aerodynamic modelling provides accurate performance characteristics for the optimisation study in chapter 9, while requiring a complementary structural model to maintain blade stresses within acceptable limits. To do so, the structural formulation is developed in the subsequent chapter.

6

Structural Model

The structural tool used in this study is an Euler-Bernoulli (EB) beam model in combination with the Saint-Venant theory of torsion. It will be used to calculate the stresses on the blade resulting from the aerodynamic loading input of the Vortex Lattice Method and the inertial loading due to the blade rotation. This structural tool is used and worked out by J. Thielen [15] based on the work of Sodja et al. [51]. Deformations of the blade are not considered in this analysis. Instead, the calculation focuses solely on the stresses induced by the aerodynamic forces and inertial loads. Blade deformation is not explicitly taken into account, as its effects are assumed to be captured by the variation in blade twist in the optimisation.

6.1. Stress Prediction from Aerodynamic and Intertial Loads

The propeller blade experiences forces from both aerodynamic and inertial sources. The aerodynamic loads, denoted as $\mathbf{q}_a$, are obtained using the Vortex Lattice Method (VLM) model. These loads are distributed across the blade's chord at each radial station. The average is taken on the chordwise loads at each station, which yield a resultant force and its associated centre of pressure. The internal moments resulting from the aerodynamic loads, $\mathbf{M}_a(s)$, are calculated by integrating the cross-product of the aerodynamic force and the vector from the blade axis (centre of gravity) to the centre of pressure, as shown in Equation (6.1).

$$\mathbf{M}_a(s) = \int_s^l \left[\mathbf{r}_a(u) - \mathbf{r}_q(s) \times \mathbf{q}_a(u)\right] du \tag{6.1}$$

In addition to aerodynamic forces, centrifugal forces act on the blade due to its rotation. These forces depend on the section mass, radial position, and angular velocity. The centrifugal forces, q_c, are expressed by Equation (6.2), where the vector $\mathbf{e}_r$ points from the section's centre of gravity to the axis of rotation.

$$\mathbf{q}_c = \rho_b dV \Omega^2 r \mathbf{e}_r \tag{6.2}$$

The internal moment due to the inertial forces is calculated using Equation (6.3), where the integrand is the cross-product of the vector from the centre of gravity to the point u and the centrifugal forces at that point.

$$\mathbf{M}_c(s) = \int_s^l \left[\mathbf{r}_q(u) - \mathbf{r}_q(s) \times \mathbf{q}_c(u)\right] du \tag{6.3}$$

The total internal moment $\mathbf{M}(s)$ is then the sum of the aerodynamic moment $\mathbf{M}_a(s)$ and the inertial moment $\mathbf{M}_c(s)$, as shown in Equation (6.4).

$$\mathbf{M}(s) = \mathbf{M}_a(s) + \mathbf{M}_c(s) \tag{6.4}$$

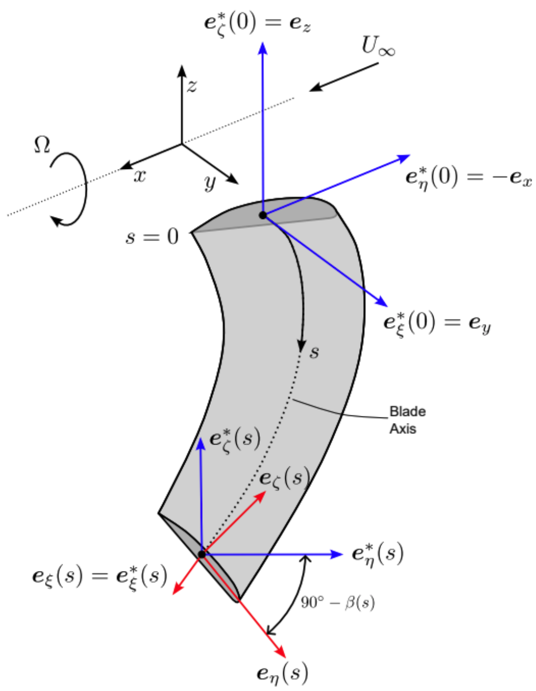

Figure 6.1: Coordinate System for use in the structural model

This internal moment $\mathbf{M}(s)$ is then decomposed into its components along the three principal axes of the blade's local coordinate system. These components are obtained by performing dot products with the unit vectors $\mathbf{e}_\xi$, $\mathbf{e}_\eta$, and $\mathbf{e}_\zeta$, as shown in Equation (6.7).

$$M_\xi(s) = \mathbf{M}(s) \cdot \mathbf{e}_\xi \tag{6.5}$$
$$M_\eta(s) = \mathbf{M}(s) \cdot \mathbf{e}_\eta \tag{6.6}$$
$$M_\zeta(s) = \mathbf{M}(s) \cdot \mathbf{e}_\zeta \tag{6.7}$$

The total normal stress and shear stress are calculated just as the Von Mises stress, which represents the total stress in the blade, is calculated using Equation (6.10).

$$\sigma = \frac{(\mathbf{q}_a + \mathbf{q}_c) \cdot \xi}{A_L} + \frac{M_\eta \eta}{I_\eta} - \frac{M_\zeta \zeta}{I_\zeta} \tag{6.8}$$
$$\tau = \frac{2M_\xi}{I_\xi} |\nabla \bar{U}| \tag{6.9}$$
$$\sigma_{VM} = \sqrt{\sigma^2 + 3\tau^2} \tag{6.10}$$

6.2. ASSUMPTIONS AND LIMITATIONS

- Deformation is not taken into account as the model will be used only for an optimisation constraint. Deformation adds complexity to the system, difficulty to the gradient calculation, and adds numerical expense.
- Blades should be an order of magnitude higher than the chord length in order for the structure to be accurately predicted by Euler-Bernoulli Beam theory
- Only a solid blade can be modelled, while propellers are usually made out of a combination of materials, including composites.

Having detailed the aerodynamic, aeroacoustic, and structural modelling framework, the following chapter goes over the validations of these models.

7
VALIDATION

The three models employed in this study are validated here to ensure accurate representation of the relevant physical phenomena. While Thielen [15] previously validated the Vortex Lattice Method (VLM) for performance predictions, the current implementation requires additional verification of the coupled aerodynamic-aeroacoustic solution. This validation is done through comparison with high-fidelity results obtained from lattice-Boltzmann very large eddy simulations coupled with Ffowcs Williams-Hawkings acoustic analogy, both comparing blade loading and aeroacoustic results. The structural model's predictive capability, particularly for von Mises stresses, is demonstrated through a comparison with an ANSYS FEM solution.

7.1. AEROACOUSTICS

To assess the validation of the combination of the VMl with Hanson's aeroacoustic model used in this study, a study is used that simulated propeller noise using high-fidelity models [16]. For aerodynamic predictions, a lattice-Boltzmann very large eddy simulation (LB-VLES) is used, and for noise radiation assessment, the Ffowcs Williams & Hawkings (FW-H) analogy is applied (referred to here as "LB"). This approach is assumed to be sufficiently accurate to validate the VLM-Hanson model used in this study.

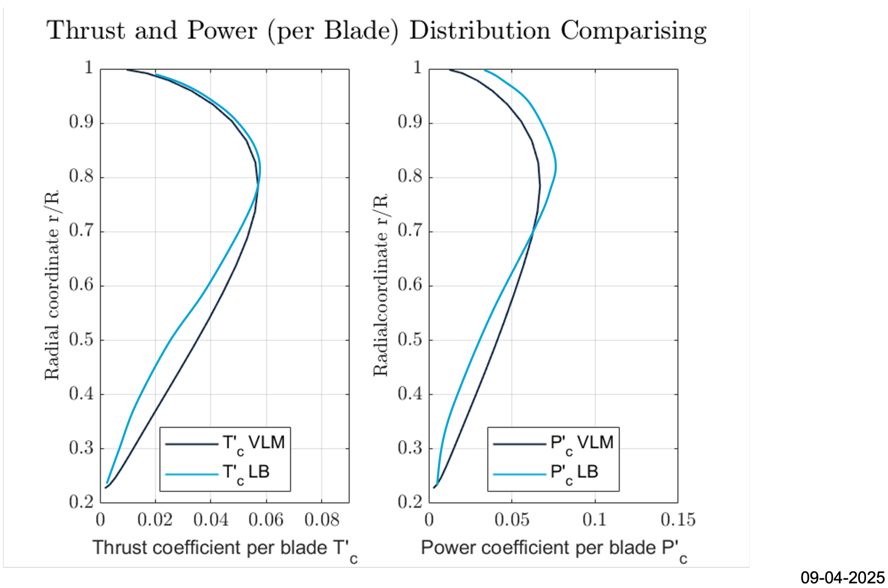

Figure 7.1: Thrust and power distribution comparison between VLM and LB-VLES models [16]

Figure 7.1 shows the blade loading comparison between the two models. This blade loading is the input for the aeroacoustic model and directly affects the aeroacoustic output. The blade loading for both thrust and

R_p [m]	N_b [-]	V [m/s]	Thrust [N]	Altitude [km]
1.7	4	55	55	16

Table 7.1: Propeller and operational parameters used for validation.

power is seen to be underpredicted at the root and slightly overpredicted at the tip. Figure 7.2 and Figure 7.3 show the total and thickness noise, as well as the decomposed loading noise, respectively. Interestingly, the noise is underpredicted by the VLM, as shown clearly in Figure 7.2. In Figure 7.3, it can be observed that the torque loading is overpredicted, likely due to the overprediction of the tip torque. Since this torque noise has a polarity 90 degrees from the thrust noise, the two components cancel each other out, resulting in lower loading noise and, consequently, lower total noise.

The symmetric thrust noise observed in the LB model is unexpected; however, these results are still considered reasonable for the final outcomes. Therefore, it can be concluded that the VLM-Hanson aeroacoustic model is suitable for use in this study.

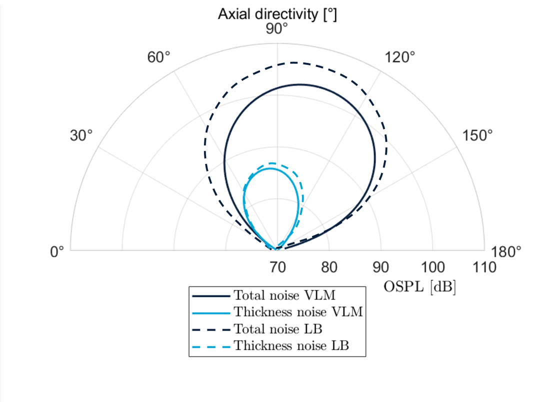

Figure 7.2: Noise directivity comparison of total and loading noise, comparing VLH-Hanson and LB-VLEM-FWH predictions [16]

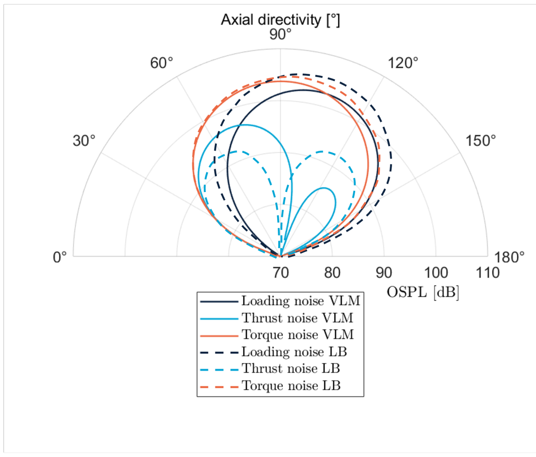

Figure 7.3: Noise directivity comparison of loading noise and its components, comparing VLH-Hanson and LB-VLEM-FWH predictions [16]

7.2. STRUCTURES

For validating the structural Euler-Bernoulli Beam (EB-Beam) model used to assess the maximum stress, a comparison is made with an Ansys FEM simulation [17]. The input parameters for both models are shown in Table 7.1, and the blade geometry and its parameter distributions are presented in Figure 7.4.

These parameters are used to simulate a similar blade configuration, combining the VLM and EB-Beam models. The results of interest are the maximum von Mises stresses, as these will also be used in the optimisation study presented in chapter 9. The blade geometry used for the simulation is shown in Figure 7.5.

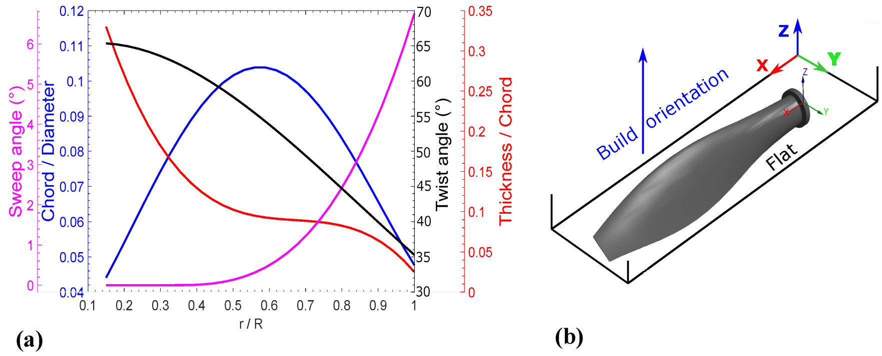

Figure 7.4: (a) Distribution of blade parameters. (b) Blade geometry input for CFD and FEM [17].

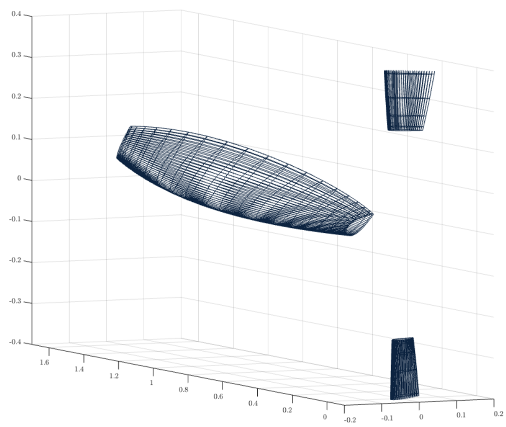

Figure 7.5: Blade geometry used as input for the EB-Beam structural model.

Figure 7.6 and Figure 7.7 show the von Mises stresses predicted by the Ansys FEM simulation and the EB-Beam model, respectively. By analysing the highest von Mises stress value on each blade section, it is observed that the maximum stress increases steadily until reaching closer to the hub, where it jumps sharply from around 3 to 5 MPa. This behaviour is consistent with both models until approximately $0.1R_h$ from the root, at which point the stress distribution diverges due to the blade-hub interface in the Ansys model. The blade distributions in Figure 7.4 only consider the aerodynamically active portion of the blade, while the cylindrical hub is not accounted for in the EB-Beam model.

In conclusion, these results show a close approximation to the Ansys model, indicating that the EB-Beam model is validated, at least for cases involving lower stress levels.

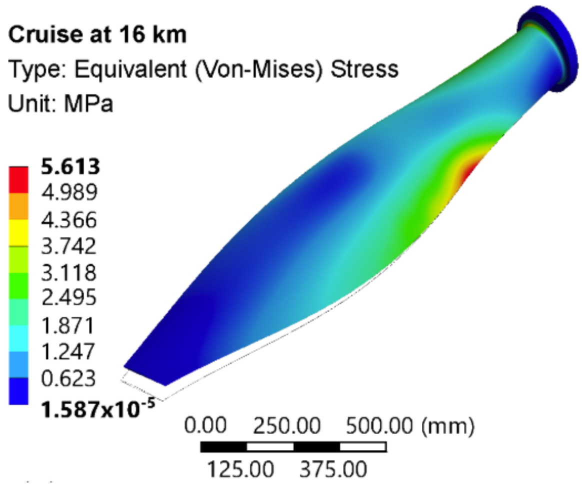

Figure 7.6: Von-Mises stresses obtained from the Ansys FEM simulation [17].

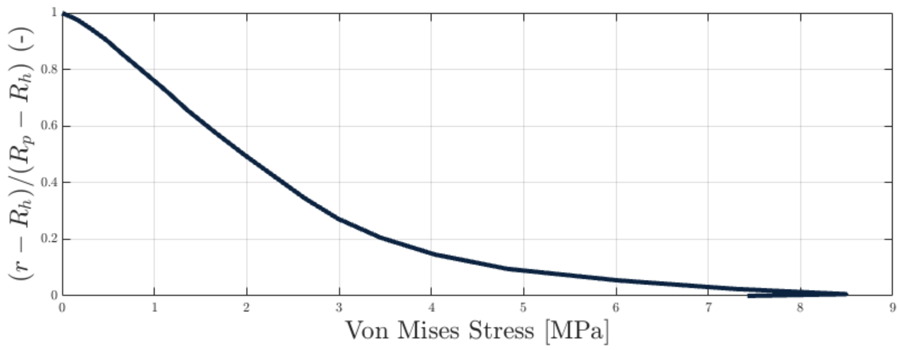

Figure 7.7: Maximum von Mises stress across radial blade sections predicted by the EB-Beam structural model.

Following the development and validation of the models, the next step is to use these models to reach the research objective. The upcoming sections outline the methodology used in the parametric and optimisation studies.

III

Study Methodology

8

PARAMETRIC STUDY

A parameter study is conducted to gain a better understanding of the impact on silent propeller design when considering noise perception, including which parameters are most dominant in perceived noise reduction and why. To determine which operating conditions most influence (perceived) noise reduction, a factorial design study will be performed, analysing the effects of these factors and their interactions. In this study, two distinct design matrices are created: one for Take-Off conditions and one for Cruise conditions, to explore potential differences between these flight phases and their implications. Response surfaces are used to clearly visualise how response variables change with varying factors. For a more detailed analysis, individual harmonics and noise sources are examined to assess their influence on both perceived and physical noise, particularly to identify when noise reduction due to added blade sweep is most effective. The book "Design and Analysis of Experiments" by Montgomery (2013) serves as a guide for this Design of Experiments, detailing methods such as factorial design, which is also the terminology applied here [52].

First, the setup of the general study is presented in section 8.1, after which it is better detailed in section 8.2. The way in which the results will be analysed is shown in section 8.3, and the chapter concludes with the assumptions and limitations of this study in section 8.4.

8.1. STUDY SETUP

This study employs a factorial design to identify the dominant factors influencing (the difference in) physical and perceived reduction through the introduction of blade sweep. Four parameters are selected, each expected to impact tonal noise and its reduction. These parameters are varied between "low" and "high" values. Each configuration is simulated twice, once with blade sweep and once without, allowing the calculation of noise reduction, generating $2 \times 2^4 = 32$ distinct experimental configurations for one flight condition. Perceived noise is also analysed using a filter applied to the harmonic content of the noise signal. To ensure fair comparison, all configurations are run through an implicit solver with an iteration scheme to calculate blade pitch, achieving consistent "high" or "low" thrust levels across all tests.

The study consists of two closely related sub-studies, each with its own design matrix: one for analysing the effects under Take-Off conditions and another for Cruise conditions. This distinction helps to explore how the factors' influence differs between these flight phases, addressing environmental noise and passenger comfort in the respective conditions of Take-Off and Cruise. By analysing these two conditions separately, the study aims to identify key differences and determine which conditions are relevant for the optimisation studies in the second part of the research, chapter 9. Both sub-studies follow the same methodological approach and are treated together in the analysis.

INPUTS

Through the literature study, several parameters have been identified as having a significant influence on noise generation and noise reduction through the addition of blade sweep. The factors selected for this study are:

- Flight Mach Number, M_x [−]

- Rotational Mach Number, M_t [−]
- Number of blades, N_b
- Thrust setting, T [N]

The flight Mach number is included because higher values enhance the effectiveness of sweep in reducing noise due to phase cancellation. Conversely, at a lower blade count and high rotational Mach number, harmonic content becomes more dominant, allowing sweep to still contribute to noise reduction even at low flight Mach numbers [6]. Additional studies support this reasoning, indicating that the rotational tip Mach number is the most influential parameter in noise reduction through blade sweep [3, 9]. Furthermore, a higher rotational Mach number increases the presence of harmonic noise, an effect also observed when the number of blades decreases [9]. Lastly, thrust is included as a factor to examine the relationship between loading and thickness noise in the context of noise reduction, as prior research has suggested its relevance [10].

OUTPUTS

To find out in which way the factor influences the (perceived) noise reduction by added blade sweep and analyse the harmonic content, the outputs will consist of four response variables for physical noise and perceived noise, respectively:

- Tonal noise in SPL and PNL
- Noise reduction in ΔSPL andΔPNL
- Harmonic Noise fraction, f_{harm}^{SPL} and f_{harm}^{PNL}

The calculation of these metric can be found in chapter 5). The tonal noise response will be used as a reference value to compare noise reduction for two reasons. First, the higher this total tonal noise level, the more significant the noise reduction would be. And secondly, if the level of perceived noise is significantly different from that of physical noise, different choices could be made for propeller design. The metric that is used for tonal noise level, SPL, will be used to refer to the root mean square of the Overall Sound Pressure Level, $OSPL^{RMS}$ but SPL is used to ensure conform and clear metric throughout the report as effectively $OSPL^{RMS}$ is approximately equal to the maximum value of SPL and thus most important for aircraft fly-over. The same goes for the levels of Perceived Noise Level and respective harmonic noise values. The response of the noise reduction is studied to analyse the influence of the operating condition, directly answering the first sub-question and determining what parameters to run the optimisation study for. The harmonic noise fraction and perceived noise reduction are analysed to examine the role of harmonics in reducing perceived noise through added blade sweep. This metric physically represents the difference in noise level between the tonal noise and the noise of only the fundamental frequency, which consequently measures how much the harmonics are represented in the tonal noise value. The harmonic noise fraction is used to assess the amount of noise generated by harmonics, which is compared to the difference in reduction of perceived noise and tonal noise to get a closer look at the role of harmonics in the difference between physical and perceived noise.

OUTPUTS

To determine how each factor influences (perceived) noise reduction through blade sweep and to analyse the harmonic content, four response variables are considered for both physical and perceived noise:

- Tonal noise in SPL and PNL
- Noise reduction in ΔSPL and ΔPNL
- Harmonic noise fraction, f_{harm}^{SPL} and f_{harm}^{PNL}

The calculations of these metrics are detailed in chapter 4.

Tonal noise serves as a reference value for comparing noise reduction for two key reasons. First, a higher overall tonal noise level implies that any noise reduction will have a greater impact. Second, significant differences between perceived and physical noise levels could lead to different propeller design choices. The metric used for tonal noise, SPL, corresponds to the Overall Sound Pressure Level ($OSPL$), but SPL is used throughout the report for consistency.

Noise reduction metrics (ΔSPL and ΔPNL) are analysed to assess the influence of operating conditions, directly addressing the first sub-question and informing the selection of parameters for the optimisation study.

The harmonic noise fraction metrics (f_{harm}^{SPL} and f_{harm}^{PNL}) are used to evaluate the role of harmonics in perceived noise reduction through the introduction of blade sweep. The harmonic noise fraction quantifies the difference between the total tonal noise and the noise of only the fundamental frequency, providing a measure of harmonic contributions to overall tonal noise. Comparing harmonic noise fractions with differences in perceived and physical noise reduction offers more profound insight into the role of harmonics in the difference between perceived and physical noise.

Factorial Design Matrix

Table 8.1 presents all runs with their respective low and high values, denoted by pluses and minuses. Using this design matrix structure, the factorial design is constructed by selecting values for each factor, considering both take-off and cruise conditions. The factor values are chosen based on nominal values from the reference aircraft, the ATR72-600, and its flight mission, supplemented by relevant literature. The difference between high and low values is selected to ensure a measurable effect on the response variables while avoiding physically infeasible designs or phenomena beyond the study's scope.

run	M_x	M_t	N_b	T
1	-	-	-	-
2	+	-	-	-
3	-	+	-	-
4	+	+	-	-
5	-	-	+	-
6	+	-	+	-
7	-	+	+	-
8	+	+	+	-
9	-	-	-	+
10	+	-	-	+
11	-	+	-	+
12	+	+	-	+
13	-	-	+	+
14	+	-	+	+
15	-	+	+	+
16	+	+	+	+

Table 8.1: Algebraic Signs for Generating the Design Matrix

Value Selection

The selection of low and high factor values is justified below and summarised in Table 8.4.

For the flight Mach number, the low value is based on the reference aircraft's Take-Off V2 airspeed (135 kts). For the Cruise study, both low and high values are chosen near the theoretical optimal flight Mach number of 0.55 for propeller aircraft [25].

For the rotational Mach number, reference values for M_r and M_{rt} are used while ensuring that the helicoidal tip Mach number M_{rt} remains sufficiently below Mach 1.

The high thrust value is determined based on the shaft horsepower per engine for maximum Take-Off and Cruise conditions for the ATR 72-600, which are 2,400 SHP and 2,088 SHP, respectively [53]. Assuming propulsive efficiencies of 80% for Take-Off and 90% for Cruise, the high thrust levels are computed using Equation 8.1. The calculation is shown in Table 8.3. The low thrust levels correspond to a 20% reduction from these high values.

$$T = \frac{P}{V_\infty} = \frac{\eta_{mech} P_s}{a M_x} \tag{8.1}$$

The number of blades is selected based on values found in relevant literature [3, 6, 9]. To maintain a consistent

Take-Off					
Factors		Resulting Parameters			
$M_x[-]$	$M_t[-]$	$M_{rt}[-]$	J[-]	$n[\frac{rev}{s}]$	$\beta_{0.7} = \beta_{0.7}^{geo}[°]$
0.15	0.6	0.62	0.79	16.2	19.7
0.22	0.6	0.64	1.15	16.2	27.6
0.15	0.8	0.81	0.59	21.6	15.0
0.22	0.8	0.83	0.86	21.6	21.4
Cruise					
Factors		Resulting Parameters			
$M_x[-]$	$M_t[-]$	$M_{rt}[-]$	J[-]	$n[\frac{rev}{s}]$	$\beta_{0.7} = \beta_{0.7}^{geo}[°]$
0.45	0.45	0.64	3.14	12.2	55.0
0.65	0.45	0.79	4.54	12.2	64.1
0.45	0.55	0.71	2.57	14.9	49.5
0.65	0.55	0.85	3.71	14.9	59.4

Table 8.2: Resulting Helicoidal Tip Mach Number, Advance Ratio, and Rotational Velocity for operational conditions

	Take-Off	Cruise
$P_s[HP]$	2400	2088
$\eta[-]$	0.8	0.9
$a[m/s]$	340	320
M_x	0.2	0.6
T[kN]	**14.74**	**6.57**

Table 8.3: Calculating max Take-Off and Cruise thrust

difference between the low and high values, the number of blades is varied by two, resulting in configurations with 4 and 6 blades.

Similarly, the sweep value for the swept blade is chosen based on its expected effectiveness in noise reduction. A tip sweep of 50° is selected, as shown in Figure 8.2. The straight blade in Figure 8.1 depicts the same blade that is used for the study without sweep.

All input values for the factors are shown in Table 8.4.

Take-Off	$M_x[-]$	$M_t[-]$	N_b	$T[kN]$
low	0.15	0.6	4	11.80
high	0.22	0.8	6	14.74

Cruise	M_x	M_t	N_b	$T[kN]$
low	0.45	0.45	4	5.25
high	0.65	0.55	6	6.57

Table 8.4: Low and high values of factors for Take-Off and Cruise study

DESIGN MATRIX

Table 8.5 presents the final factor values for all runs. While these values are used as inputs for the models, the blade pitch must first be determined to ensure the required thrust is achieved for each configuration.

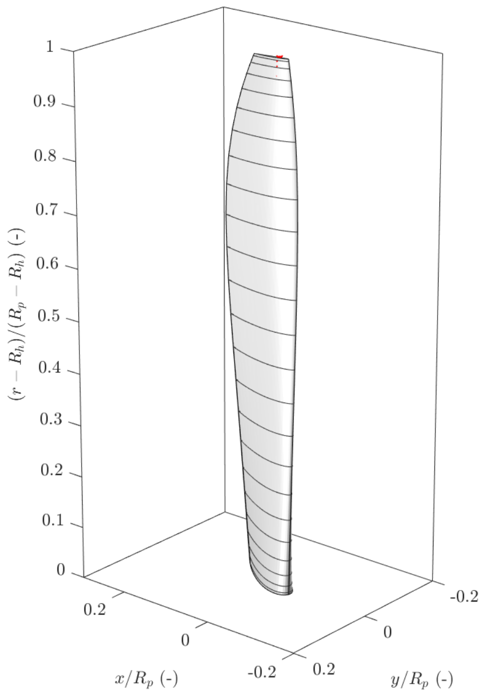

Figure 8.1: XPROP blade used to represent the low blade sweep (with no blade sweep)

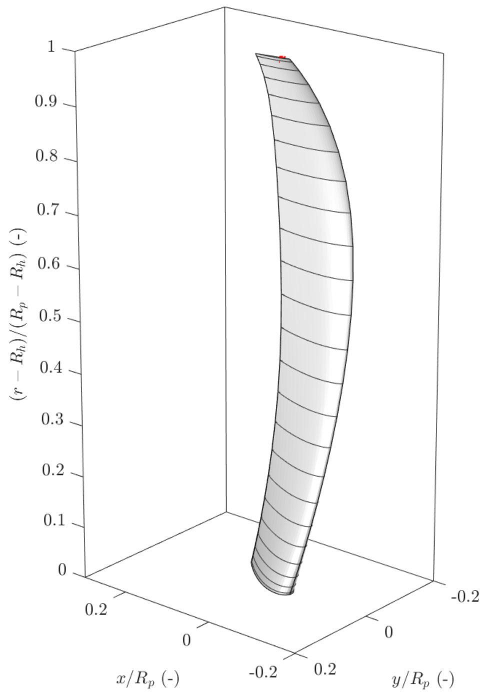

Figure 8.2: XPROP blade with 50° of sweep used to represent the blade with a high level of sweep

Take-Off					Cruise				
run	$M_x[-]$	$M_t[-]$	N_b	$T[kN]$	run	$M_x[-]$	M_t[-]	N_b	$T[kN]$
1	0.15	0.6	4	11.80	1	0.45	0.45	4	5.25
2	0.22	0.6	4	11.80	2	0.65	0.45	4	5.25
3	0.15	0.8	4	11.80	3	0.45	0.55	4	5.25
4	0.22	0.8	4	11.80	4	0.65	0.55	4	5.25
5	0.15	0.6	6	11.80	5	0.45	0.45	6	5.25
6	0.22	0.6	6	11.80	6	0.65	0.45	6	5.25
7	0.15	0.8	6	11.80	7	0.45	0.55	6	5.25
8	0.22	0.8	6	11.80	8	0.65	0.55	6	5.25
9	0.15	0.6	4	14.74	9	0.45	0.45	4	6.57
10	0.22	0.6	4	14.74	10	0.65	0.45	4	6.57
11	0.15	0.8	4	14.74	11	0.45	0.55	4	6.57
12	0.22	0.8	4	14.74	12	0.65	0.55	4	6.57
13	0.15	0.6	6	14.74	13	0.45	0.45	6	6.57
14	0.22	0.6	6	14.74	14	0.65	0.45	6	6.57
15	0.15	0.8	6	14.74	15	0.45	0.55	6	6.57
16	0.22	0.8	6	14.74	16	0.65	0.55	6	6.57

Table 8.5: Design Matrix for Take-Off and Cruise Factorial designs

8.2. FACTORIAL DESIGN PROCEDURE

From the design matrix onward, several steps must be taken to execute the study. To finalise the input for the simulation, a value for the pitch of the blade must be determined to ensure the correct thrust value. With these finalised input values, the simulation can proceed. Performing post-processing on the outcome of the aeroacoustic model by calculating the noise reduction and converting physical noise from Sound Pressure Level (SPL) to Perceived Noise Level (PNL), the effects of the factors on the response variable can be analysed, leading to the final results.

IMPLICIT SOLUTION OF PITCH FOR THE RIGHT THRUST

In this study, thrust is an output variable rather than an input, as it depends on the aerodynamic results of the model. To ensure the desired thrust level is achieved, blade pitch is adjusted accordingly. While both rotational velocity and blade pitch can typically be varied to control thrust, rotational velocity is already fixed by setting the rotational tip Mach number. Consequently, blade pitch will be used to regulate thrust for each run.

Since blade sweep also affects thrust, two pitch values must be determined for every run: one for the straight blade and one for the swept blade. This implicit calculation of pitch based on input thrust is performed using a Newton-Raphson method, as shown in Equation 8.4. In each iteration, the VLM model computes thrust, adjusting the pitch until the required thrust is met.

$$\beta_{n+1} = \beta_n - \frac{f_T(\mathbf{x}_n)}{f'_T(\mathbf{x}_n)} \tag{8.2}$$

$$f_T(\beta) = T(\beta) - T_{obj} \tag{8.3}$$

$$f'_T(\beta) = \frac{T(\beta + \Delta\beta)}{(\beta + \Delta\beta)} \tag{8.4}$$

If the convergence criterion, $|\frac{f_{T,n} - f_{T,n-1}}{T_{obj}}| < \varepsilon$, is met, the loop stops, and the computed pitch is stored for use as an input in the noise model.

A short sensitivity study is conducted to assess the influence of $\Delta\beta$ on the output of $f_T(\beta)$, ensuring that the chosen $\Delta\beta$ provides sufficient accuracy in the resulting thrust. A tolerance of $\varepsilon = 1\%$ is applied to achieve accurate pitch results, enabling reliable aerodynamic and aeroacoustic analysis.

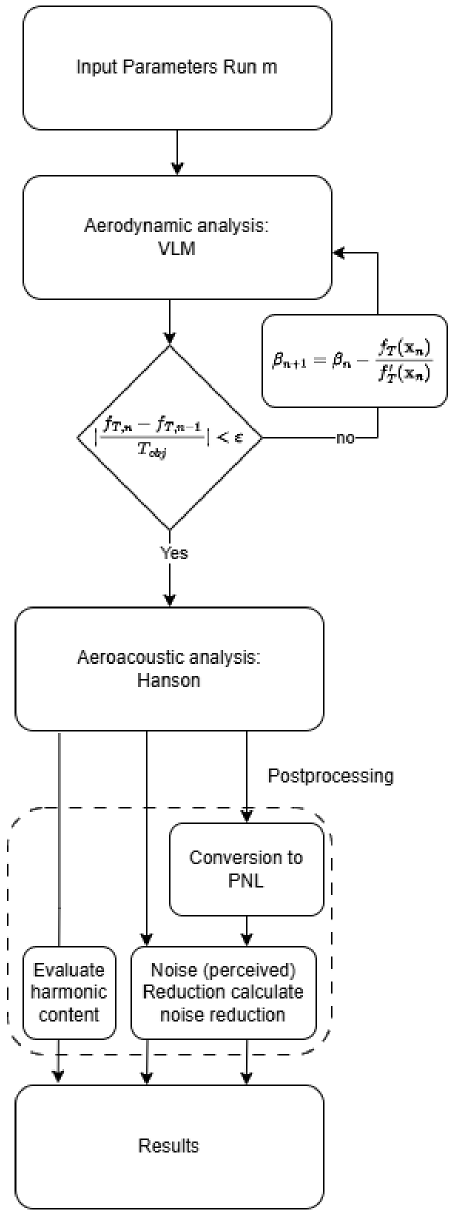

Figure 8.3: Flow diagram of factorial design procedure

AERODYNAMIC AND AEROACOUSTIC ANALYSIS INPUT

To obtain the aerodynamic results, which are also required for determining the right pitch as described in section Figure 8.2, the VLM is run as shown in chapter 4. For noise modelling, Hanson's Helicoidal Model is used, as detailed in the (citation of the noise model chapter). In table Table 8.6, the relevant input variables for the aeroacoustic modelling are provided.

For calculating the perceived noise per harmonic, the conversion to perceived noise uses a filter on discrete 1/3 octave bandwidths. Interpolation is applied to obtain precise estimates for each harmonic individually (citation of the noise model chapter). This approach enables a better analysis of the noise perception results, as it avoids discrete changes in the noise values of the harmonics.

	Take-Off	Cruise
Observer distance	$100R_p$	$3R_p$
Max Multiples of BPF	7	
Radiation angle	$30° - 150°$	

Table 8.6: Observation parameter for aeroacoustic model

In this application, the main objective is to analyse variations in the results, making a continuous function the most beneficial. The perceived noise per harmonic is also calculated to assess the harmonic content of the results of interest.

RESPONSE VARIABLES

To obtain the results needed for analysing the outcome, the aeroacoustic output must be post-processed. First, these outcomes are converted into the appropriate metrics for the desired response variables, of which the metrics that are introduced here can be found in Table 8.7. Detailed assessment of the calculation of the Overall Sound Pressure Level OSPL chapter 5 .

Category	Name	Metric	Calculation
Noise	Harmonic Fraction of Noise	$f_{harm}^{SPL}[dB]$	$OSPL[dB] - SPL_{m=1}[dB]$
	Noise Reduction	$\Delta SPL[\Delta dB]$	$OSPL_{straight}[dB] - OSPL_{swept}[dB]$
Perceived Noise	Harmonic Fraction of Perceived Noise	$f_{harm}^{PNL}[dB]$	$PNL[dB] - PNL_{m=1}[dB]$
	Perceived Noise Reduction	$\Delta PNL[\Delta dB]$	$PNL_{straight}[dB] - PNL_{swept}[dB]$

Table 8.7: Noise and Perceived Noise Metrics

Even though perceived noise PNL is in units of $[PNLdB]$ instead of $[dB]$. A different exact definition is used here by using $[dB]$ to allow for better comparison of the metrics.

8.3. ANALYSIS OF THE RESULTS

The results will be presented in several ways, ranging from an overview of all results to a more detailed analysis of the harmonic content.

- **Total results:** The results are presented by showing the values of the factors and response variables for every individual run.
- **Main and interaction effects:** A table is provided with the values of the main and interaction effects of the response variable due to the factors.
- **Response surfaces:** The main and interaction effects are graphically represented by a surface, which also includes the average value of the response variables.
- **Harmonic content:** Graphs are presented showing the physical and perceived noise level of all harmonics (including the fundamental frequency) to analyse what causes the noise decrease or increase.
- **Noise sources:** Directivity plots of the different noise sources are shown, with a particular focus on the ratio between loading and thickness noise to clarify which noise reduction mechanism is dominant.

An interesting observation can be made about the response variables that show noise reduction. In this study, two types of noise reduction are differentiated. The first type of noise reduction is achieved within individual runs by sweeping the blade. This is the primary noise reduction method that is the focus of this study. The second type of noise reduction is observed between individual runs by changing the operating conditions and the number of blades.

MAIN AND INTERACTION

To analyse the sensitivity of the factors to the response variables, the effect is divided into the main effect and the interaction effect. As an example, the response y to factors A and B is used. The main effect (of one factor) is the average response of the response variable to that factor. The magnitude of the interaction effect (of multiple factors) is the average difference of a factor on that other factor. Equation 8.5 shows how these effects are calculated.

$$\beta_f = \frac{\sum_{n=1}^{m} c_{f,n} y_n}{m/2} \tag{8.5}$$

- E_f is the main or interaction effect. E_A for example is the main effect of A on the response variable y and E_{AB} is the interaction effect of A and B on y.
- m is the maximum number of runs, 4 in this example case
- $x_{f,n}$ are the factor values on a coded scale (from -1 to $+1$) where f is the factor(s) of the main of interaction effect for each run n. The values for an interaction effect between A and B for example is then $x_{AB,n} = x_{A,n} \cdot x_{B,n}$ as shown in Table 8.8.
- y_n are the values of the response value for each run n.

$$E_{AB} = \frac{\sum_{n=1}^{4} x_{AB,n} y_n}{4/2} = \frac{1 \times 1 - 1 \times 6 - 1 \times 2 + 1 \times 4}{4/2} = -1.5 \tag{8.6}$$

The interaction effect can be calculated for multiple factors at the same time, but only the interaction effect of two factors at a time is assessed. That is because it is assumed that no clear evidence is present that the interaction effect of three factors at a time is substantial, and if these values are present in a marginal way, their interaction is not relevant for this study.

n	x_A	x_B	x_{AB}	y
1	-1	-1	1	1
2	1	-1	-1	6
3	-1	1	-1	2
4	1	1	1	4

Table 8.8: Example of factorial study results

	β_A	β_B	β_{AB}		Min	Zero	Max
y	3.50	0.50	-1.50				

Table 8.9: Example of main effects (A, B) and interaction effect (AB)

The main effect and interaction effect will be studied for every four factors for every six response variables and two flight conditions, Take-Off and Cruise. This means that for the main effect, $4 \times 6 \times 2 = 48$ values are obtained and for the interaction effect, as all factors are crossed, $(3+2+1) \times 6 \times 2 = 72$.

RESPONSE SURFACE

Analysing the results of the response variables through looking at the values of the main effect and interaction effect can be hard because there are $48 + 72 = 120$ values that are obtained. To look at the data in a more intuitive way, response surface plots are made with the sensitivity values that are deemed interesting. With these three-dimensional plots, the response of two factors can be shown such that the main effect, the interaction effect, and the absolute values are represented graphically by a surface. This can be used very effectively to see trends, draw conclusions from, and see what phenomena to have a closer look at. A response surface plot is made by using the parameters from the regression model representation as shown in Equation 8.7. $\hat{\beta}_0$ is the average value of the response variable and the other values of $\hat{\beta}$ are half the value of main and interaction values of β as they the difference between the minimum and maximum value in the coded scale is 2 $(= 1 - -1)$.

$$\hat{y} = \hat{\beta}_0 + \hat{\beta}_1 x_1 + \hat{\beta}_2 x_2 + \hat{\beta}_{12} x_1 x_2 \tag{8.7}$$

$$\hat{\beta}_0 = \frac{\sum_{n=1}^{m} y_n}{m} \tag{8.8}$$

$$\hat{\beta}_1 = \beta_1/2 \tag{8.9}$$

$$\hat{\beta}_2 = \beta_2/2 \tag{8.10}$$

$$\hat{\beta}_{12} = \beta_{12}/2 \tag{8.11}$$

The same example data is used inFigure 8.4 to show the outcome of such a response surface plot.

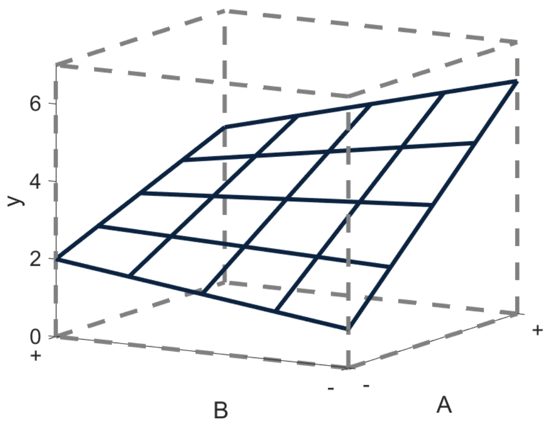

Figure 8.4: Example Response Surface

8.4. ASSUMPTIONS AND LIMITATIONS

Assumptions:

- Aeroacoustic phenomena of interest are modelled with sufficient accuracy to draw conclusions about the sensitivity of the response variables to the imposed factors.
- The interaction effect of more than two factors at a time is considered negligible.
- Only two values per factor are used as inputs, meaning that only first-order linear trends can be demonstrated in the response variables.
- Thrust is kept constant by adjusting the pitch. Different results could arise if the blade were optimised specifically for each case.
- No statistical analysis is performed, and as such, the variance is not precisely determined. However, the results are checked to ensure that high variance does not invalidate the conclusions.
- Mach shifting is not included in the study, so the harmonics are analysed separately. This effect is not significant during cruise and has a lesser impact during take-off.
- The definition of Mid-Chord-Alignment, used to apply blade sweep, results in the blade loading being shifted outward. This generally does not contribute positively to noise reduction.

9

Propeller Optimisation

Based on this knowledge from the parameter study in chapter 10, an optimisation study is conducted to assess the differences in the resulting propeller blade in multiple trade-offs between the reduction of Effective Perceived Noise Level (EPNL) and the required power penalty to achieve that. These trade-offs are performed by making various Pareto fronts with different propeller design choices and varying the design vector to differentiate between multiple phenomena that reduce (perceived) noise. These optimisations are also run with Sound Pressure Level (SPL) as the minimisation objective to assess the difference between optimising a propeller for EPNL and for SPL.

The final analysis will focus on the resulting blade geometries, harmonic content, and blade loading.

First, an overview of the optimisation study is presented in section 9.1, followed by a more technical discussion of the optimisation problem and workflow in section 9.2. Then in section 9.3, it is explained how the noise metrics are calculated, which will be used as an objective to be minimised. The following part contains all the optimisation inputs together with the choices that are made regarding this process in section 9.4.

9.1. Optimisation Study Overview

This study focuses on optimising a 6-bladed propeller for take-off conditions, as the parameter study indicated that both the impact of sweep and the difference between physical and perceived noise are most pronounced during this flight phase. A 6-blade configuration was selected due to its favourable noise characteristics.

The optimisation process consists of multiple steps to investigate the trade-off between Effective Perceived Noise Level (EPNL) and power required. All optimisations are conducted at take-off conditions using the reference ATR-72 propeller geometry and thrust requirement, while ensuring structural feasibility through a Von Mises stress constraint. Multiple optimisations are done while using a physical noise equivalent of EPNL, namely Effective Specific Noise level (ESPL), to analyse the difference in resulting blade geometry when optimising the propeller for physical noise.

During the initial trade-off study, it was observed that increased blade curvature, introduced through sweep, led to an unintended increase in blade length. This increased blade length reduces the sectional blade loading, which in turn contributes significantly to noise reduction. However, this geometric effect of added blade length began to dominate the noise reduction performance, making it difficult to isolate and study the impact of sweep alone. To address this, the optimisation study was split into two parts: one where the blade radius was kept constant, allowing for natural changes in blade length, and another where blade length was constrained to remain constant. This separation enables a more accurate assessment of the specific contribution of sweep to noise reduction, independent of the beneficial but confounding effect of increased blade length.

The first step is to find the minimum required power operating point by optimising only the advance ratio (J) and pitch angle (β) for the baseline XPROP blade. This results in an initial operating condition that is then used in a full design optimisation—including pitch, advance ratio, sweep distribution ($\boldsymbol{\gamma}$), and twist distribution (MCA), to minimise required power. This yields the MPROP blade with constant blade length, serving as the baseline for all subsequent noise optimisations.

From MPROP, multiple Pareto fronts are constructed. Each front comprises three points, representing a trade-off between noise and required power. The first point is MPROP itself. The second and third points are obtained by optimising for EPNL, while allowing 1% and 2% increases in power consumption, respectively. These power penalties provide flexibility in altering the blade geometry to achieve noise reduction.

Two types of Pareto fronts are generated:

- One with a fixed blade radius, ranging from MPROP$^{\textbf{c-rad}}$ to PMPROP$^{\textbf{c-rad}}$.
- One with a fixed blade length, ranging from MPROP$^{\textbf{c-len}}$ to PMPROP$^{\textbf{c-len}}$.

Additionally, two supporting optimisation processes are performed with reduced design vectors to isolate the effects of pitch and sweep:

- A constant blade length optimisation using only J and β.
- A constant blade length optimisation using J, β, and $\boldsymbol{\gamma}$.

These allow a clearer understanding of how sweep and blade loading individually contribute to noise reduction.

9.2. OPTIMISATION PROBLEM AND WORKFLOW

For obtaining this trade-off of EPNL and power required as seen in Figure 9.1 the definition is used below.

$$\begin{aligned}
&\text{Minimise the objective function:} && f(x) \\
&\text{subject to the inequality constraint:} && g(x) \leq 0 \\
&\text{and the equality constraints:} && h_j(x) = 0, \quad j = 1, \ldots, p \\
&\text{and the move limit bounds:} && x^l \geq x_i \geq x^u
\end{aligned} \tag{9.1}$$

Through using such an optimisation definition, Pareto fronts will be generated to do a quantitative assessment of these trade-offs. Figure 9.1 shows an example of such a Pareto front. The first optimisation that is done is one to obtain the optimum operating conditions, pitch, and advance ratio to minimise required power. From this point the last initializing optimisation is done which minimises required power put uses the total design vector, containing pitch, advance ratio, twist distribution and sweep distribution, $\mathbf{x} : (J, \beta, \boldsymbol{\gamma}, \mathbf{MCA})$. The following MPROP will be the starting point of the Pareto front, which will contain three points. The second two points will consist of two optimisations that minimise the EPNL through varying a power penalty, which is the extra power required for the propeller to use in order for the optimisation algorithm to have more freedom in changing the propeller geometry. First, the propeller is given 1% power penalty and for the last point, a 2% power penalty is given. These numbers are chosen based on reference material [36], [7].

Table 9.1 shows the exact optimisations that are done in this study with the corresponding design vector, $\mathbf{x}$, constraints, and objective function. The second inequality constraint $g_1(\mathbf{x})$ is only active for the minimisation of EPNL, as this will add the power penalty. The value of P^{MPROP} is the required power of the MPROP$^{\textbf{c-len}}$ optimisation, which is the optimisation that keeps the blade length constant. This reference point is taken as most Pareto fronts will have this propeller as a starting point, and ensures that a fair comparison of the results can be made later on.

The following propellers (and operating conditions) are optimised as starting points for the rest of the optimisations.

- **XPROP**: Baseline propeller used as the starting point for all optimisations. An optimisation is done while only optimising the pitch and advance ratio to have an operating condition with the minimum required power with the XPROP blade, which is then a good starting point to do the required power minimisations to obtain **MPROP**$^{\textbf{c-rad}}$ and **MPROP**$^{\textbf{c-len}}$.
- **MPROP**$^{\textbf{c-rad}}$: Propeller optimised for minimum required power (P_{req}) with a constant blade radius. The design vector includes J, β, $\boldsymbol{\gamma}$, and MCA. This is the starting point of the Pareto front using a constant blade radius, which ends in the PMPROP$^{\textbf{c-rad}}$.

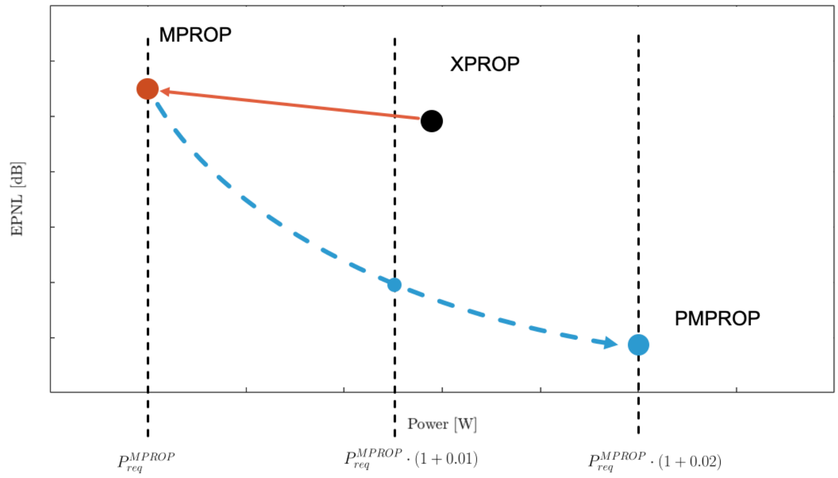

Figure 9.1: Example of a single Pareto front

- **MPROP$^{\textbf{c-len}}$**: Propeller optimised for minimum required power (P_{req}) with a constant blade length. The design vector includes J, β, $\boldsymbol{\gamma}$, and MCA. Start point of all Pareto fronts using a constant blade length (every Pareto front except for the one ending on PMPROP$^{\textbf{c-rad}}$

The following propellers will be the end stations with the maximum required power penalty of 2% and will thus correspond to the four different Pareto fronts.

- **PMPROP$^{\textbf{c-rad}}$**: Propeller optimised for minimum Effective Perceived Noise Level (EPNL) with a 2% allowable power penalty, maintaining constant blade radius. The design vector includes J, β, $\boldsymbol{\gamma}$, and MCA.
- **PMPROP$^{\textbf{c-len}}$**: Propeller optimised for minimum Effective Perceived Noise Level (EPNL) with a 2% allowable power penalty, maintaining constant blade length. The design vector includes J, β, $\boldsymbol{\gamma}$, and MCA.
- **Constant blade length optimisation with Design Vector $\mathbf{x}$** : (J, β): Constant blade length optimisation focusing on adjusting advance ratio (J) and blade pitch (β) to assess noise reduction through blade loading modifications.
- **Constant blade length optimisation with Design Vector $\mathbf{x}$** : $(J, \beta, \boldsymbol{\gamma})$: Constant blade length optimisation incorporating advance ratio (J), blade pitch (β), and blade sweep ($\boldsymbol{\gamma}$) to evaluate noise reduction via other sweep-induced noise reducing effects.

Start Prop	Resulting Prop	Objective	Design Vector			Constraints	
				$f(\mathbf{x})$	$h(\mathbf{x})$	$g_1(\mathbf{x})$	$g_2(\mathbf{x})$
–	XPROP	P_{req}	J, β	P_{req}	$T = T_{TO}$	$\sigma_{v-m}(\mathbf{x}) \leq \sigma_{v-m}^{max}$	—
XPROP	MPROP$^{\textbf{c-len}}$	P_{req}	$J, \beta, \boldsymbol{\gamma}$, **MCA**	P_{req}	$T = T_{TO}$	$\sigma_{v-m}(\mathbf{x}) \leq \sigma_{v-m}^{max}$	—
XPROP	MPROP$^{\textbf{c-rad}}$	P_{req}	$J, \beta, \boldsymbol{\gamma}$, **MCA**	P_{req}	$T = T_{TO}$	$\sigma_{v-m}(\mathbf{x}) \leq \sigma_{v-m}^{max}$	—
MPROP$^{\textbf{c-len}}$	-	EPNL	J, β	$EPNL$	$T = T_{TO}$	$\sigma_{v-m}(\mathbf{x}) \leq \sigma_{v-m}^{max}$	$P \leq 1.01 P^{MPROP}$
MPROP$^{\textbf{c-len}}$	-	EPNL	J, β	$EPNL$	$T = T_{TO}$	$\sigma_{v-m}(\mathbf{x}) \leq \sigma_{v-m}^{max}$	$P \leq 1.02 P^{MPROP}$
MPROP$^{\textbf{c-len}}$	-	EPNL	$J, \beta, \boldsymbol{\gamma}$	$EPNL$	$T = T_{TO}$	$\sigma_{v-m}(\mathbf{x}) \leq \sigma_{v-m}^{max}$	$P \leq 1.01 P^{MPROP}$
MPROP$^{\textbf{c-len}}$	-	EPNL	$J, \beta, \boldsymbol{\gamma}$	$EPNL$	$T = T_{TO}$	$\sigma_{v-m}(\mathbf{x}) \leq \sigma_{v-m}^{max}$	$P \leq 1.02 P^{MPROP}$
MPROP$^{\textbf{c-len}}$	-	EPNL	$J, \beta, \boldsymbol{\gamma}$, **MCA**	$EPNL$	$T = T_{TO}$	$\sigma_{v-m}(\mathbf{x}) \leq \sigma_{v-m}^{max}$	$P \leq 1.01 P^{MPROP}$
MPROP$^{\textbf{c-len}}$	PMPROP$^{\textbf{c-len}}$	EPNL	$J, \beta, \boldsymbol{\gamma}$, **MCA**	$EPNL$	$T = T_{TO}$	$\sigma_{v-m}(\mathbf{x}) \leq \sigma_{v-m}^{max}$	$P \leq 1.02 P^{MPROP}$
MPROP$^{\textbf{c-rad}}$	-	EPNL	$J, \beta, \boldsymbol{\gamma}$, **MCA**	$EPNL$	$T = T_{TO}$	$\sigma_{v-m}(\mathbf{x}) \leq \sigma_{v-m}^{max}$	$P \leq 1.01 P^{MPROP}$
MPROP$^{\textbf{c-rad}}$	PMPROP$^{\textbf{c-rad}}$	EPNL	$J, \beta, \boldsymbol{\gamma}$, **MCA**	$EPNL$	$T = T_{TO}$	$\sigma_{v-m}(\mathbf{x}) \leq \sigma_{v-m}^{max}$	$P \leq 1.02 P^{MPROP}$

Table 9.1: Optimisation inputs for generating all four Pareto Fronts

For both optimisation workflows, MATLAB's FMINCON is used [54]. The `fmincon` function in MATLAB is a numerical solver designed to handle nonlinear constrained optimisation problems. It minimises a scalar objective function while satisfying various types of constraints, including bounds on variables, linear inequalities or equalities, and general nonlinear constraints.

Figure 9.2 and Figure 9.3 show respectively the workflows of the MPROP optimisation, minimising power required, and the rest of the optimisations, optimising EPNL and ESPL. They both use the VLM for aerodynamic modelling and the EB-beam model for the stress requirement. The difference between the two optimisation workflows is the objective function and the added analysis of EPNL/ESPL for minimum generated noise.

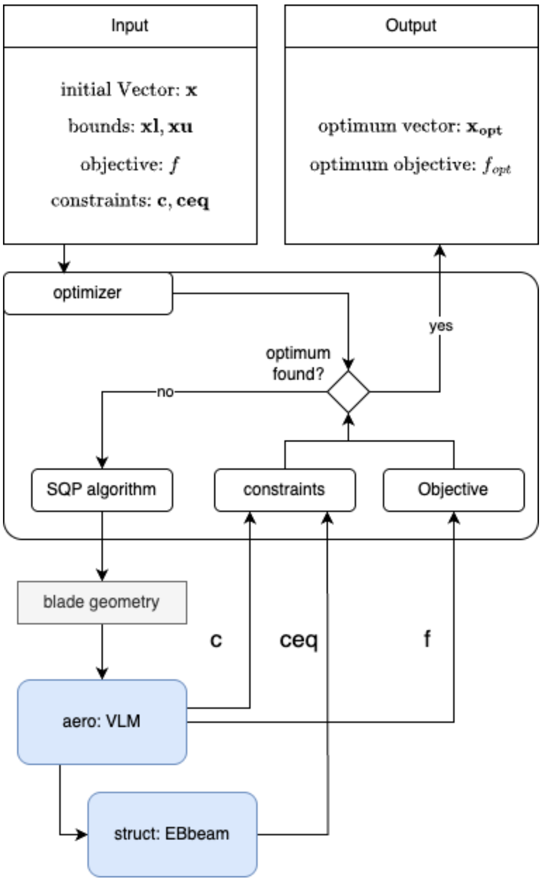

Figure 9.2: Optimisation flow for minimising power required

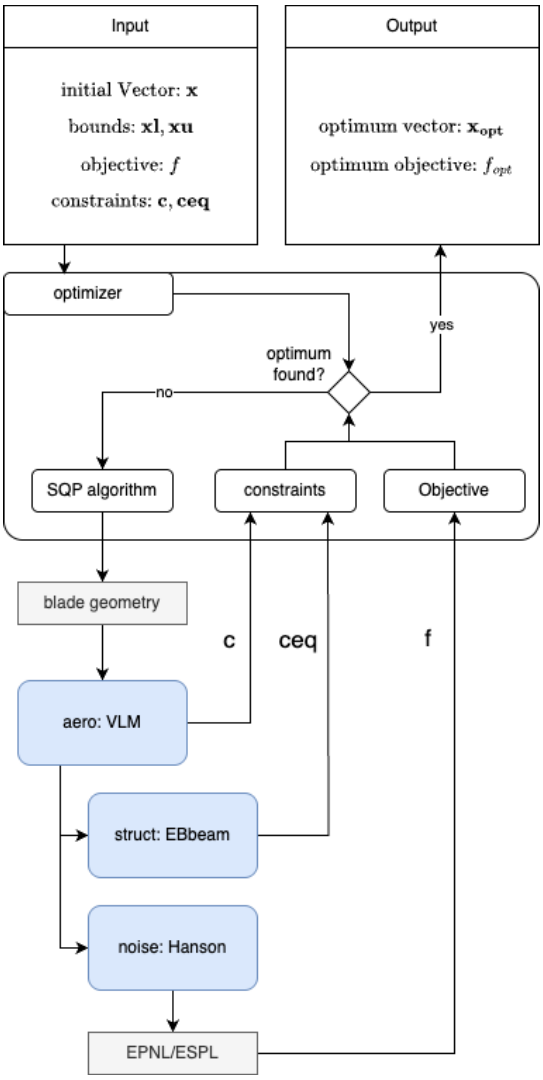

Figure 9.3: Optimisation flow for minimising noise

9.2.1. DESIGN VARIABLES AND PARAMETER INPUT VALUES

From the insights of the parameter study, the design variables used to do the optimisation have to accommodate a few things. These design variables are shown in Table 9.2. They use operational conditions, blade sweep, and blade twist to make sure these insights are taken care of. Blade twist is added in addition to blade MCA to give the optimiser a way to control the blade loading, as this is seen to have a great influence on the produced noise. The choice is made to include only three parameters of Sweep and the full 5 variables (6 minus one because pitch controls the last degree of freedom) controlling the twist distribution. This is done to let the optimisation have more freedom in determining the optimal blade loading to make sure that the blade sweep won't be used much for the control over blade loading.

	Operational Conditions		Hub Twist		Tip Twist			Tip MCA		
Design Variables	J	β	$d\gamma$	γ_k	γ	$d\gamma$	γ_k	Λ	$d\Lambda$	Λ_k

Table 9.2: Design Variables including the operational conditions, blade twist distribution and blade MCA distribution

OPERATIONAL CONDITIONS

As the rotational tip Mach number M_t has been shown to be a very important parameter to reduce noise, especially perceived noise, this parameter is included by using the advance ratio J as a design variable. M_t will be used for reporting, as this variable has a better physical representation in this context. The blade pitch (at 0.7 blade radius) $\beta = \beta_{0.7}$ is included as well to ensure that the take-off thrust constraint is met.

BLADE SWEEP

As the main reason for this study is to study the resulting blade sweep, this is taken into account by using three variables to change the sweep distribution.

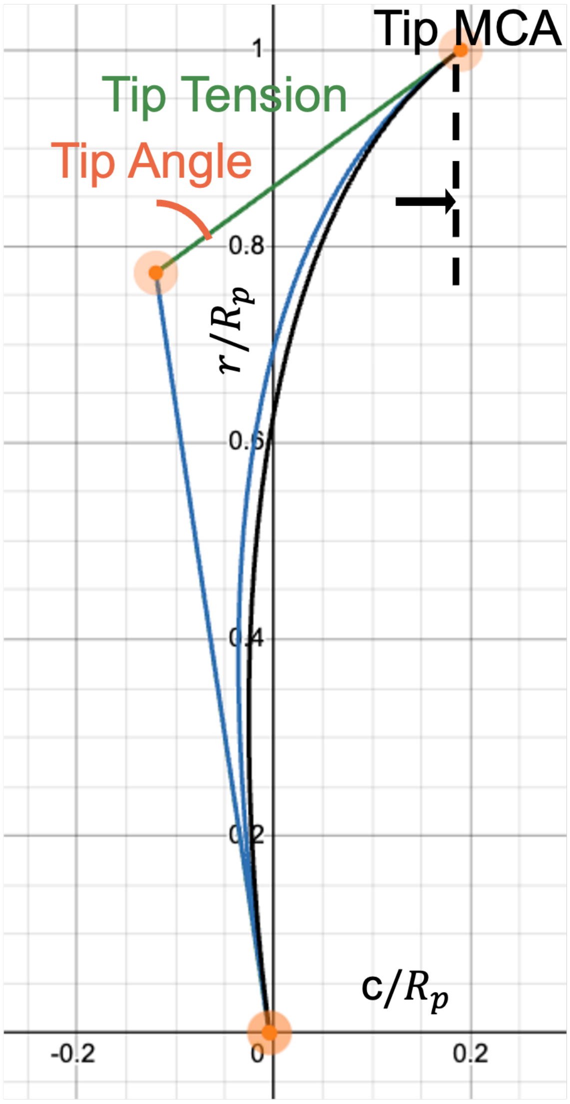

Figure 9.4: Blade Sweep parametrisation

BLADE TWIST

From the parameter study, the load distribution for noise reduction has shown its significance. To ensure efficient noise reduction by the blade sweep, three variables are added to shift the load distribution. While chord distribution can be used as well to change the load distribution, using the twist to do this would change the blade in a more subtle way. The change in load comes from a change in angle of attack, which can be adjusted more easily by changing the twist, which would result in an inefficient blade when done by changing the chord.

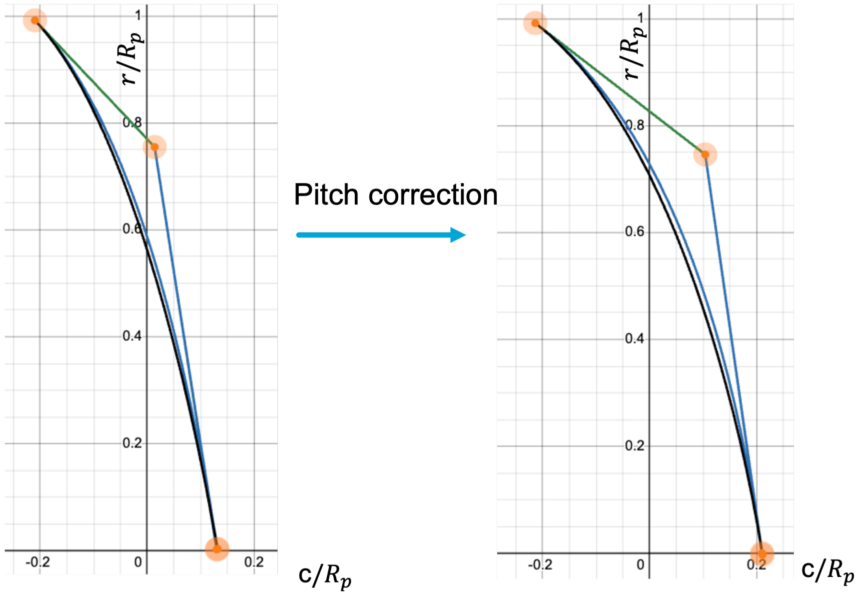

Figure 9.5: Blade twist parametrisation and correction for assuring pitch

9.3. NOISE CALCULATIONS

The noise calculated for the objective functions, EPNL, is done as handled in chapter 5, together with a simplified Take-Off trajectory that is explained here. For an equal comparison of perceived and physical noise, an EPNL equivalent metric is made using the Sound Pressure Level (SPL), deemed ESPL (Effective Sound Pressure Level). For the correct input values of PNL and SPL for calculating EPNL and ESPL corrections, the noise level must be corrected to take into account the Doppler Shift.

1. Hanson's Helicoidal Model
2. Trajectory Corrections
   (a) Amplitude, varying the observer distance
   (b) Frequency shift due to the Doppler effect
3. EPNL/ESPL calculation

The trajectory that is used is such that it approaches the Take-Off trajectory as described in certification for propeller aircraft [49]. While a 4° flight path is written in certification, for simplicity, a flat flight path is assumed, also because the most noise is produced when the aircraft is right above the observer, which is when the angle of the flight path matters least. The flight velocity for the trajectory is V_2 plus an extra margin of 19.1 [km/h]. V_2 is 116 KCAS for the reference aircraft [53]. This means that the final velocity used will be:

$$U_\infty = 116 \times 0.514444 + \frac{19.1}{3.6} \approx \boxed{65\,\mathrm{m/s}}$$

The height that is used according to certification for propeller aircraft:

$$h = \boxed{650\,\mathrm{m}}$$

To calculate the variables of the trajectory needed for obtaining the final levels of EPNL/EPNL. As with the Hanson's model that is used in this study, the values of noise level are calculated for a certain directional spacing (e.g. one value each degree), these points will be the input of the trajectory from which for every points, different values have to be obtained to calculate the noise level at all of those points in the trajectory. The variables that have to be obtained are:

- dt for every angle θ
- Observer distance

The following equations are used as graphically shown in Figure 9.6.

$$r_{obs} = h \cdot sin\theta \tag{9.2}$$

$$\begin{aligned} dx &= \frac{d\theta \cdot h}{\sin\theta} \\ dt &= \frac{dx}{U_\infty} \\ dt &= \frac{d\theta \cdot h}{U_\infty \cdot \sin\theta} \end{aligned} \tag{9.3}$$

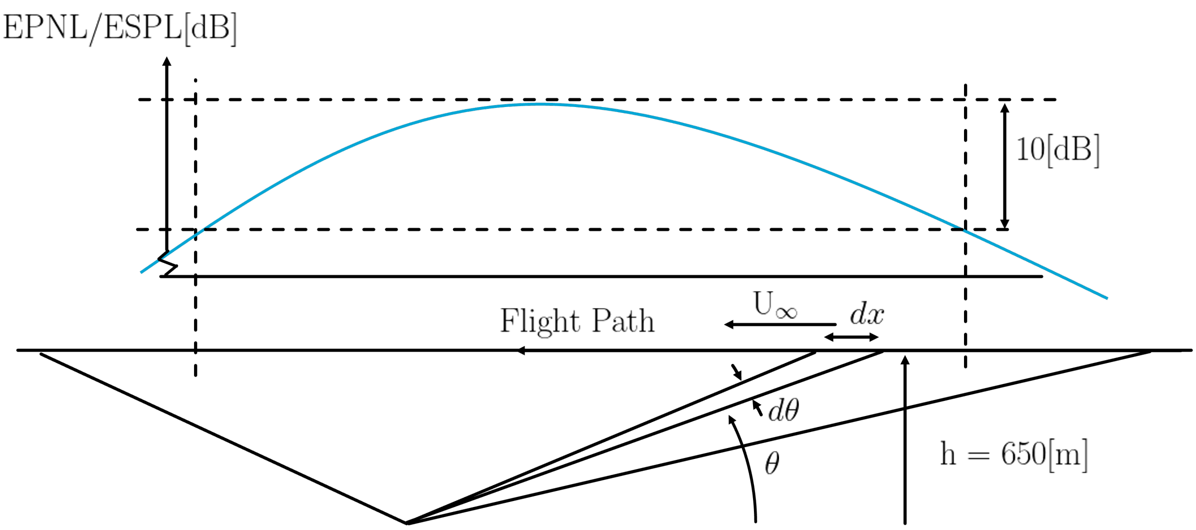

Figure 9.6: EPNL & ESPL calculation

With this trajectory, the values of SPL and PNL are corrected to have the correct amplitude and frequency for the observer distance and relative flight velocity at every point in the trajectory. The frequency is shifted with Equation 9.4 through the Doppler effect.

$$f_d = \frac{f}{1 - cos\theta} \tag{9.4}$$

Using these corrections, the final values are obtained for PNL and SPL for the entire trajectory. Together with the values for dt on all points on the trajectory, EPNL and ESPL can be calculated. As stated in the certification, only the data points are taken into account that are above a noise level of 10 decibels below the maximum noise level, also shown graphically in Figure 9.6.

$$\text{EPNL} = 10\log\frac{1}{10}\int_{t_{\textbf{max noise -10 [dB]}}}^{t_{\textbf{max noise}}} 10^{0.1\,\text{PNLT}(t)}\,dt \tag{9.5}$$

$$\text{ESPL} = 10\log\frac{1}{10}\int_{t_{\textbf{max noise -10 [dB]}}}^{t_{\textbf{max noise}}} 10^{0.1\,\text{SPL}(t)}\,dt \tag{9.6}$$

9.4. INPUT PARAMETERS

The parameter values with the optimisation runs will use some constant variables, varying power constraints, and an input design vector, the changes of which occur for every run. Regarding this design vector, only the first run, to obtain both MPROPs, will be predetermined, as the rest of the optimisation will start out with output variables of one of the previous runs.

DESIGN VECTOR

As the optimisation starts with the XPROP, the design vector variables concerning the propeller blade will also correspond to those of the XPROP, as shown in Table 9.3. The operational conditions, J and β, are obtained by optimising for power with only these two variables in the design vector.

	Operational Conditions		Hub Twist		Tip Twist			Tip MCA		
Design Variables	$J[-]$	$\beta[°]$	$d\gamma[°]$	$\gamma_k[-]$	$\gamma[°]$	$d\gamma[°]$	$\gamma_k[-]$	$\Lambda[°]$	$d\Lambda[°]$	$\Lambda_k[-]$
Value	0.89	23.1	35	0.2	-8.5	10	0.375	0	0	0.3

Table 9.3: Initialising design variables corresponding to the XPROP blade, including the operational conditions, blade sweep distribution and blade twist distribution

To make sure that the gradients $d(d\Lambda)/dx$ and $d\Lambda_k/dx$ are positive, the value of Λ_k is set to 0.3 when the input vector contains an unswept blade. This variable represents the "tension" of the Bezier curve parametrisation at the tip of the blade. This won't change the geometry as the angle $d\Lambda$ is zero itself but this does make sure that when the optimizer starts exploring gradients, there will be a geometric change in the blade when changing one of both $d\Lambda$ or Λ_k as when they are both zero, putting changing only one of those variables at a time, no change in parameter is present.

BLADE MATERIAL AND STRUCTURES

For determining the blade material and respective structural constraint, a rough educated estimation will suffice, as this model is used primarily to put a constraint on unrealistic blade shapes.

For the weight estimation, a value between the density of carbon fibre and that of titanium ($\rho = 2.4\,\mathrm{g/cm^3}$) is adopted as a representative value.

In a similar fashion, a maximum von Mises stress is chosen. To get an idea of the value for the maximum allowable stress, a combination of very rough approximations of maximum tensile, compression, and shear stress is used in combination with a safety factor, but also through doing some tests of what kind of blade geometries are obtained when varying the maximum Von Mises stress constraint. Starting with some very rough approximations:

- **Tensile strength (along fibres):** 1000-1500 MPa
  - Failure mode: fibre fracture
- **Compressive strength (along fibres):** 500-1000 MPa
  - Failure mode: fibre microbuckling or kinking
- **Shear strength (in-plane):** 70-120 MPa
  - Failure mode: matrix shear or fibre/matrix interface failure

Using a safety factor of 5 to take into account fatigue loads, dynamic loading, and other structural phenomena that are not taken into account, a value of around $\sigma_{\max} = 60\,\mathrm{MPa}$ is obtained by means of an educated approximation. While trying some different values of this stress constraint around this value, a final stress constraint $\sigma_{\max} = 40\,\mathrm{MPa}$ is chosen as a conservative way to take care of the structural discipline without doing much research on these phenomena, as this is not in the scope of this study.

Table 9.4 shows the final values used in the optimisation.

Parameter	$\rho[g/mm^2]$	σ_{v-m}^{max}
Value	2400	40MPa

Table 9.4: Design Variables, including the operational conditions, blade sweep distribution, and blade twist distribution

CONSTRAINTS

Table 9.5 shows the values for the constraints. The exact value of the Take-Off requirement is taken as already used in chapter 8. The value of the inequality constraint concerning the power will be used when optimising

EPNL or ESPL. This value is based on the required power for the XPROP with optimised operational conditions, J and β. This inequality constraint will vary for different optimisations with a different power penalty.

Constraints	$h(\mathbf{x}) = T_{TO}[kN]$	$g_1(\mathbf{x}) \leq \sigma_{v-m}^{max}[MPa]$	$g_2(\mathbf{x}) \leq P_{req}[kW]$
Value	14.72	40	$P_{req}^{MPROP} \times (1 + \text{penalty})$

Table 9.5: Values of the constraints, used in the optimisation, represent the power penalty that is used at various levels for all runs that use the MPROP as input.

A structural constraint is used to make sure that no impossible shapes will be used, which might aeroacoustically lead to reduced noise. To do so, an inequality constraint is put on the maximum Von-Mises Stresses. Figure 9.7 shows an example of this constraint. The maximum value of these stresses cannot exceed the inequality constraint.

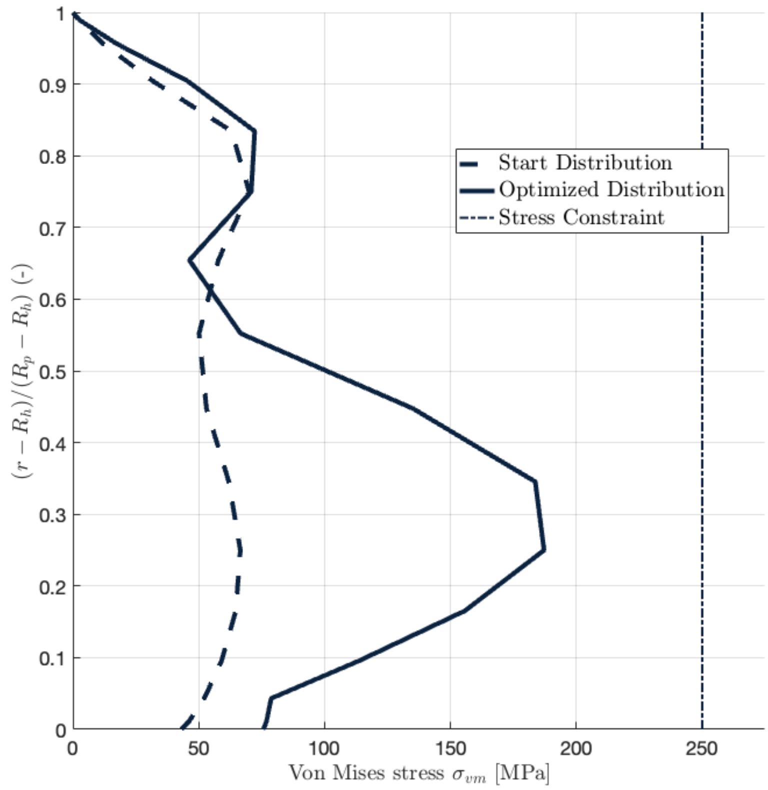

Figure 9.7: Example of a (Satisfied) stress Constraint of the start and end of an optimisation; $\sigma_{v-m}(\mathbf{x}) \leq \sigma_{v-m}^{max} = 250[MPa]$

IV

Results

10

Parameter Study Results

In this chapter, the results of the parameter study conducted in chapter 8 are presented. A factorial design study was performed to analyse the influence of operating conditions and the number of blades on (perceived) noise reduction. Two parallel batches of simulations were carried out: one for take-off conditions and one for cruise conditions. This approach was chosen to determine whether trends differ between the two scenarios and to identify when it is most relevant to incorporate noise perception in blade optimisation. A decision is made to exclude the cruise condition case from detailed analysis, as its outcomes are deemed less relevant. Therefore, the main results focus on the take-off conditions, which are analysed in greater detail and used to address the majority of the research questions.

First, the overall results showing the effects of the factors on all response variables are presented in section 10.1. Subsequently, in section 10.2 a selection of data is made for representation in regression surfaces, which are used to analyse the main trends in section 10.3. In the latter section, additional tools, such as harmonic content plots and directivity plots of different noise sources, are employed to provide further detail.

10.1. Response Variables Results

The results of the parameter study are presented in Table 10.1. The table displays the main effects of individual factors on the six response variables, as well as the interaction effects of two factors on the response variables. The response variable "SPL/PNL Red" is defined to be the sweep-induced noise reduction, which is the noise reduction through applying blade sweep while maintaining a constant thrust through changing the propeller pitch as explained in chapter 8. The main effect represents the average difference in response between the high and low values of a factor, while the interaction effect indicates the average difference in the main effect due to a change in another factor. For both take-off and cruise conditions, the response variables are shown with the physical noise response and the perceived noise response listed beneath each other for an easy comparison between the two.

Not all data is relevant or significant; therefore, a selection is made to determine which data to analyse further. This ensures that all factors are represented in the results and that all interesting phenomena are captured in the surfaces. Table 10.1 is used to guide this selection. Combinations of variables that are not displayed have minimal interaction effects, and their dominant main effects are already captured in the presented surfaces. The factors on the two bottom axes of the response surface graphs will be the following:

- M_t, M_x
- M_t, N_b
- M_t, T

All variables are plotted alongside M_t because significant interaction effects are observed for these combinations, while the remaining interactions are negligible. An additional advantage of the surfaces is that they display the average response rather than just the effects, thereby showing absolute values. Therefore, the surfaces provide a reference frame and offer a more comprehensive understanding of the observed phenomena.

Takeoff	Mx	Mt	T	N	Mx Mt	Mx T	Mx N	Mt T	Mt N	T N
SPL	2.54	11.40	1.57	-5.07	-0.51	0.00	0.00	-0.43	2.85	-0.25
Harmfrac	0.01	1.37	-0.10	-0.13	0.01	0.00	0.00	-0.10	-0.04	0.01
SPL Red	0.03	-0.18	0.08	0.00	0.00	-0.01	0.00	-0.08	0.16	-0.02
PNL	3.09	18.52	1.80	-1.91	-0.82	-0.01	-0.09	-0.79	1.90	-0.31
Harmfrac	-0.03	2.77	-0.27	-0.57	-0.03	0.01	0.05	-0.30	-0.35	0.07
PNL	0.00	0.13	0.06	-0.05	-0.01	-0.01	0.02	-0.14	0.22	-0.01

Cruise	Mx	Mt	T	N	Mx Mt	Mx T	Mx N	Mt T	Mt N	T N
SPL	8.44	7.28	1.76	-8.22	0.49	-0.04	1.01	-0.30	2.34	-0.17
Harmfrac	0.18	0.23	-0.02	-0.07	0.14	-0.01	-0.01	-0.02	-0.04	0.00
SPL Red	0.01	0.04	0.04	-0.08	0.04	-0.01	-0.01	-0.02	0.06	0.01
PNL	8.80	9.00	1.73	-5.68	0.74	-0.06	0.95	-0.34	2.68	-0.16
Harmfrac	0.76	0.48	-0.05	0.35	0.40	-0.04	-0.04	-0.04	-0.25	-0.01
PNL	0.06	0.10	0.03	-0.07	0.10	-0.01	0.00	-0.03	0.07	0.01

Table 10.1: Main and interaction effects of the parameters on the response variables in dB. More saturated blue is a higher main or interaction effect, the more saturated yellow, the higher that value in a negative direction. "SPL/PNL Red" is the sweep-induced noise reduction, and "Harmfrac" is the harmonic fraction (chapter 5).

10.2. Result Analysis

First, some general trends in the response of noise reduction and noise level are presented.

10.2.1. Comparing Cruise and Take-Off

In Figure 10.1, the response of physical noise reduction and perceived noise reduction is compared for Take-Off and Cruise conditions. A significant difference in response is observed for these two conditions. Both the absolute value of noise reduction and the difference between physical and perceived noise are notably larger for Take-Off compared to Cruise conditions. In Cruise conditions, both noise reduction and perceived noise reduction average around 0.2 [dB] and exhibit minimal variation. This trend is also reflected in the values for the main and interaction effects in Table 10.1.

In contrast, the graphs for Take-Off conditions reveal more interesting and distinct results for the two noise metrics, suggesting a potential reason for incorporating noise perception in propeller design. Consequently, the decision is made to exclude the Cruise condition results from further analysis, and the focus is placed on the Take-Off condition results.

The next sections will only deal with the results of the Take-Off conditions study.

10.2.2. Noise Level

Figure 10.2 illustrates the response of physical and perceived noise levels for a straight blade. The graph reveals the factor combinations that result in the lowest overall (perceived) noise level, as well as the conditions under which the difference between physical and perceived noise is the greatest. When this difference is largest, it indicates that incorporating noise perception into propeller design becomes particularly relevant.

Examining the influence of the factors, the most significant effect observed is the increase in noise with an increase in the Rotational Tip Mach Number (M_t), as shown in Figure 10.2. As M_t increases, noise radiates more efficiently. Although the pitch decreases to maintain the same thrust, the absolute noise level rises significantly with higher M_t. The fundamental frequency and low harmonics receive less weight in the conversion to perceived noise due to their low frequency. However, as the Blade Passing Frequency (BPF) increases, the perceived noise level approaches the physical noise level as all frequencies increase and so do their weights. This is achieved not only by increasing M_t but also by increasing the Number of Blades (N_b). Consequently, noise perception becomes more relevant at lower values of both M_t and N_b.

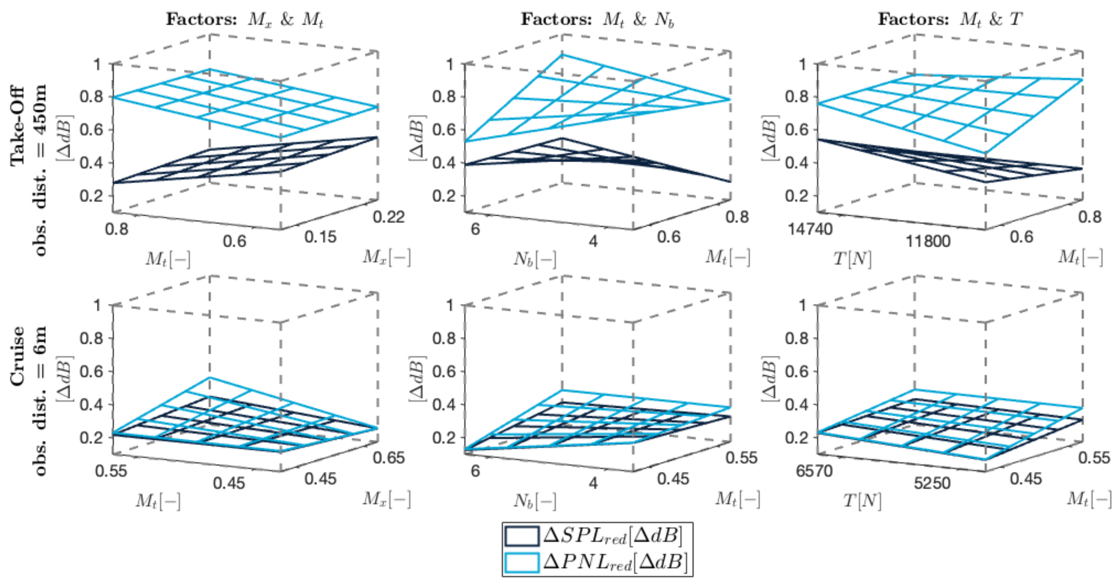

Figure 10.1: Response surfaces of (perceived) noise reduction to $[M_t, M_x]$, $[M_t, N_b]$ and$[M_t, T]$ for take-off and cruise. $\Delta SPL/SPL_{red}$ is the sweep-induced noise reduction

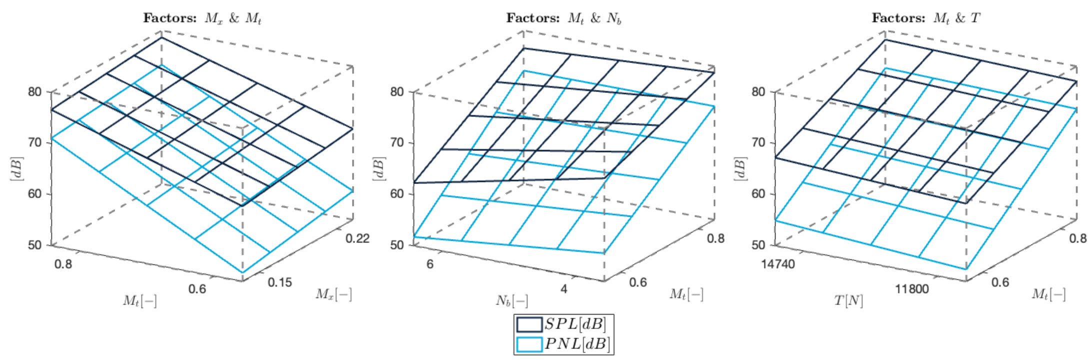

Figure 10.2: Response surfaces of (perceived) noise to $[M_t, M_x]$, $[M_t, N_b]$, and $[M_t, T]$ for take-off conditions.

While a lower M_t corresponds to a lower noise level, the opposite is true for N_b: an increase in N_b leads to a reduction in noise level. Therefore, a combination of low M_t and high N_b would result in the quietest propeller. This trend is observed for both physical and perceived noise levels.

However, it is important to note that the interaction effect between N_b and M_t differs for physical and perceived noise. Increasing N_b reduces the noise level for both metrics, but this effect is less pronounced for perceived noise than for physical noise. This implies that when designing a propeller for perceived noise, increasing the number of blades is less beneficial compared to designing for physical noise. This effect becomes more pronounced at higher M_t values, where increasing N_b does not significantly reduce the perceived noise level.

The Flight Mach Number (M_x) and thrust (T) have less significant effects on noise levels. An increase in either of these factors leads to a higher noise level, which is consistent for both physical and perceived noise, as expected.

10.3. NOISE REDUCTION

Looking at the response surfaces of sweep-induced noise reduction in Figure 10.2, some interesting behaviour is observed. Specifically, the focus is on the differences in behaviour between metrics related to physical noise and perceived noise. Generally, it is observed that noise reduction due to blade sweep is always higher for perceived noise compared to physical noise. This is due to the combination of the higher weighting of high-frequency noise in perceived noise metrics and the fact that high-frequency noise is generally reduced more effectively when introducing blade sweep. Blade sweep is more effective at phase-cancelling noise with wavelengths closer to the value of the difference in blade mean chord alignment (MCA), where noise radiation is most prominent [6].

For the swept blade used in this study (Figure 8.2), the difference in MCA at the tip of the blade—where noise radiation is most prominent—is approximately $0.15R = 0.3\,[\mathrm{m}]$. This means that noise components with frequencies around $\frac{320\,[\mathrm{m/s}]}{0.3\,[\mathrm{m}]} = 1067\,[\mathrm{Hz}]$ are cancelled most effectively. However, the blade passing frequencies (BPF) for all runs in this study are below 100 [Hz], and thus all harmonics contributing significantly to the total noise are below the frequency of most effective phase cancelling. Consequently, in all cases examined in this study, the higher the frequency, the more effective the phase cancelling due to blade sweep, resulting in a greater reduction in perceived noise compared to physical noise.

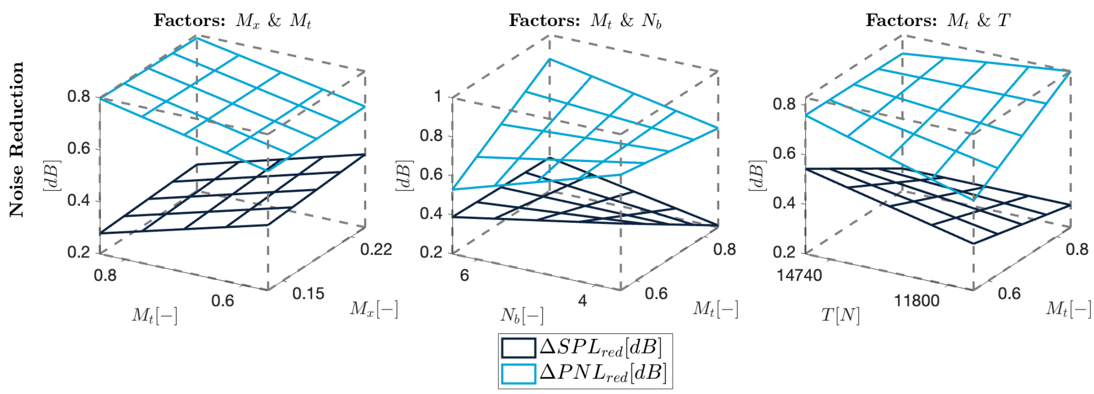

Figure 10.3: Noise reduction response due to $[M_t, M_x]$, $[M_t, N_b]$, and $[M_t, T]$ in take-off conditions. $\Delta SPL/SPL_{red}$ is the sweep-induced noise reduction

Furthermore, when comparing the trends of physical and perceived noise in Figure 10.3, some opposite trends are observed in the response of noise reduction to the Rotational Tip Mach Number (M_t). As M_t increases, the sweep-induced perceived noise reduction increases, while the sweep-induced physical noise reduction decreases.

Other opposing effects are observed for the number of blades (N_b) and thrust (T) when comparing the trends in sweep-induced noise reduction response at high and low values of M_t. A significant interaction effect is present for both physical and perceived noise. To analyse this behaviour, plots comparing the harmonic content of single runs, as well as plots comparing noise sources, are used.

10.3.1. NOISE REDUCTION RESPONSE TO ROTATIONAL TIP MACH NUMBER

Opposite main effects are observed in the response of physical and perceived sweep-induced noise reduction to the Rotational Tip Mach Number (M_t), as clearly shown in the left graph of Figure 10.3. Examining the main effect of M_t on physical and perceived noise reduction reveals two distinct trends. Increasing M_t decreases the physical noise reduction while simultaneously increasing the perceived noise reduction. This indicates that as M_t increases, noise reduction (achieved by introducing blade sweep) becomes more effective for perceived noise but less effective for physical noise.

Several factors contribute to this behaviour. As M_t increases, the Blade Passing Frequency (BPF) also increases, making phase cancellation more effective. This effect can be seen in Figure 10.5 by comparing the difference in total noise levels (straight versus swept blade results) between the to runs Additionally, the contribution of harmonics to the total noise level increases with rising M_t which can be seen in the same figure when comparing the decline in noise amplitude with rising multiple of BPF.

Furthermore, Figure 10.4 shows a more general result of the contribution of harmonics to the total noise level through the response of the Harmonic Fraction, which quantifies the proportion of noise that consists of harmonic components. At low values of M_t, the harmonics contribute 0 [dB] and 2 [dB] to physical and perceived

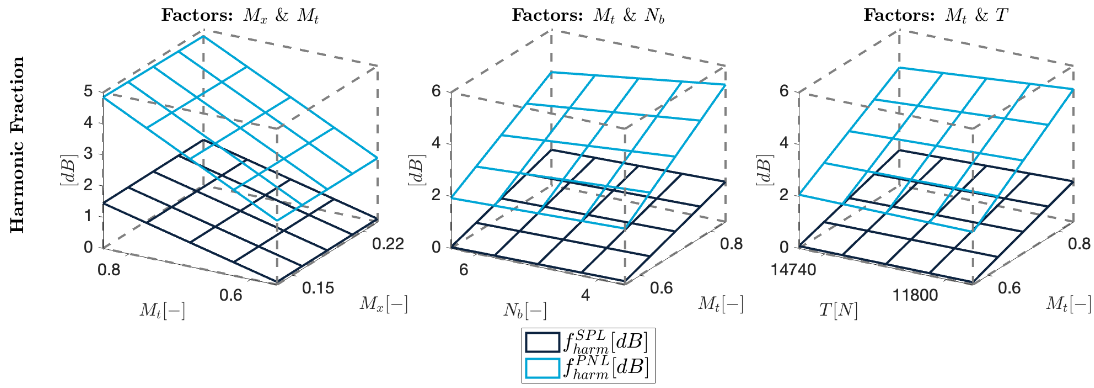

Figure 10.4: Harmonic Fraction Response due to $[M_t, M_x]$, $[M_t, N_b]$ and$[M_t, T]$ in in take-off conditions

noise, respectively. At high values of M_t, these contributions increase to 1.5 [dB] and 5 [dB], respectively. This demonstrates that at higher M_t levels, harmonics constitute a significantly larger portion of the total tonal noise, making them more effectively reduced through phase cancellation.

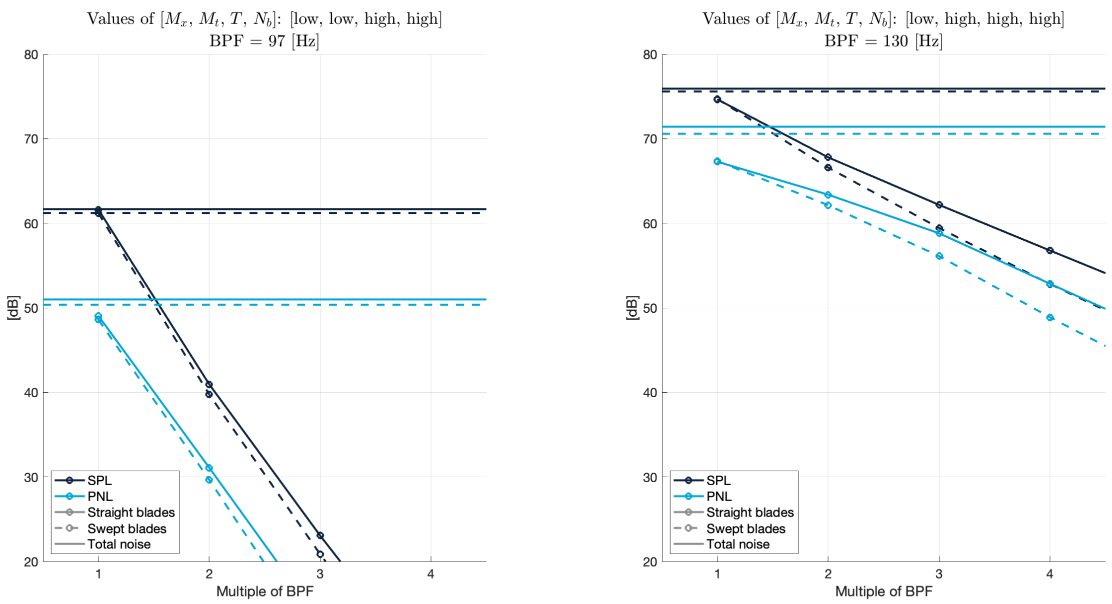

(a) Low Rotational Tip Mach Number

(b) High Rotational Tip Mach Number

Figure 10.5: Harmonic content and total noise values, comparing physical and perceived noise, straight and swept blades

Although these effects apply to both physical and perceived noise, a third effect counteracts sweep-induced the noise reduction. Due to the way sweep is defined through mean chord alignment (MCA), the blade loads shift toward the tip as the level of backwards sweep increases [55]. As the blade is swept, the angle of attack increases with higher MCA values. This means that while blade sweep achieves noise reduction, it does so less effectively because the blade loading is shifted toward the tip, where noise radiates more efficiently. Therefore, the reduction of noise by introducing blade sweep is a combination of sweep-induced noise reduction through phase cancellation and noise increase due to added loading noise.

With an increase in M_t, the perceived noise reduction is greater because phase cancellation outweighs the added loading noise. In contrast, for physical noise, the opposite is true. The noise reduction reduces as the contribution of higher frequency noise is lower, while noise in this spectrum gets reduced more effectively with blade sweep.

Although a different definition of blade sweep might lead to different values of noise reduction, the difference between physical and perceived noise would likely remain the same or increase. This implies that at higher levels of M_t, the significance of noise perception is expected to be greater.

10.3.2. NOISE REDUCTION RESPONSE TO NUMBER OF BLADES AND ROTATIONAL MACH NUMBER

The effect of the number of blades (N_b) on sweep-induced noise reduction shows opposite trends for low and high Rotational Tip Mach Number (M_t), which is consistent for both physical and perceived noise. This can be observed in the middle graph of Figure 10.2. While the main effect of N_b on physical and perceived sweep-induced noise reduction is almost negligible, the interaction effect is significantly more substantial, as clearly shown in the figure. This means that the main effect of N_b (at a constant M_t) on noise reduction significantly reduces at low M_t and increases at high M_t.

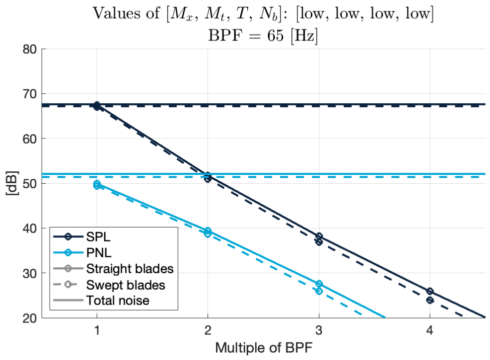

(a) M_t, N_b = Low, Low

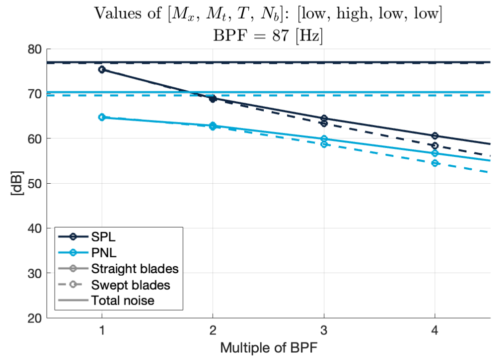

(b) M_t, N_b = High, Low

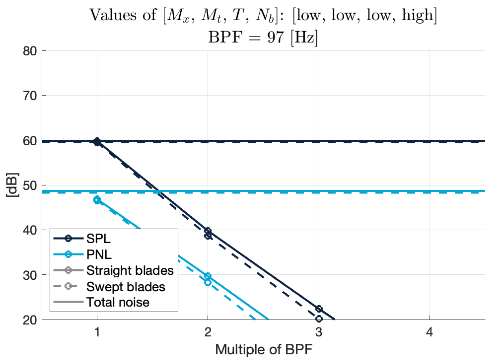

(c) M_t, N_b = Low, High

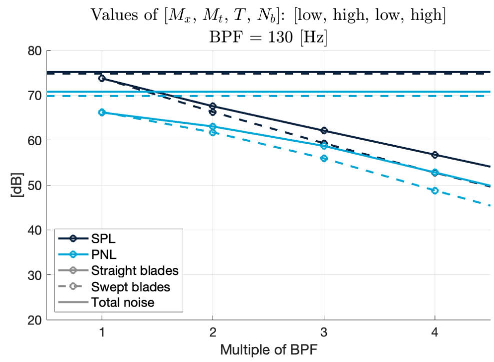

(d) M_t, N_b = High, High

Figure 10.6: Harmonic content and total noise values, comparing physical and perceived noise, straight and swept blades

With an increase in the number of blades, two opposing effects come into play. First, as N_b increases, the Blade Passing Frequency (BPF) also increases, making blade sweep more effective at reducing noise. However, an increase in N_b also steepens the harmonic content, reducing the amount of harmonic noise that can be effectively reduced through blade sweep. This effect is clearly illustrated in Figure 10.6.

In cases with low M_t, the total noise reduction is almost entirely dependent on the reduction of the fundamental frequency noise. The reduction of harmonics, which are more effectively cancelled, plays a less significant role. As a result, the total noise reduction decreases with an increase in N_b when M_t is low. Conversely, at high Rotational Tip Mach Numbers, the harmonics contribute significantly to the total noise, as seen in Figure 10.4. This means that the increase in BPF makes noise reduction more effective in these cases.

10.3.3. NOISE REDUCTION RESPONSE TO THRUST AND ROTATIONAL MACH NUMBER

The right graph in Figure 10.3 shows an increase in noise reduction with increasing thrust at low values of M_t, while at high levels of M_t, the noise reduction remains roughly constant. This interaction is influenced by several phenomena, including changes in noise levels and the ratio of thickness noise to loading noise.

Sweep-induced noise reduction is influenced by two main factors: a shift in blade loading and phase cancellation. At both high and low values of M_t, a similar shift in blade loading is expected. However, phase cancellation becomes significant only at high levels of M_t. This phase cancellation is effective for both loading noise and thickness noise.

Regarding the shift in blade loading, this effect impacts only the loading noise and does not affect the thickness noise. This means that when thickness noise dominates, phase cancellation drives changes in the noise level, and thus, this change in loading noise will not affect the total level of tonal noise. Conversely, when loading noise dominates, the shift in blade loading due to sweep will alter the noise level.

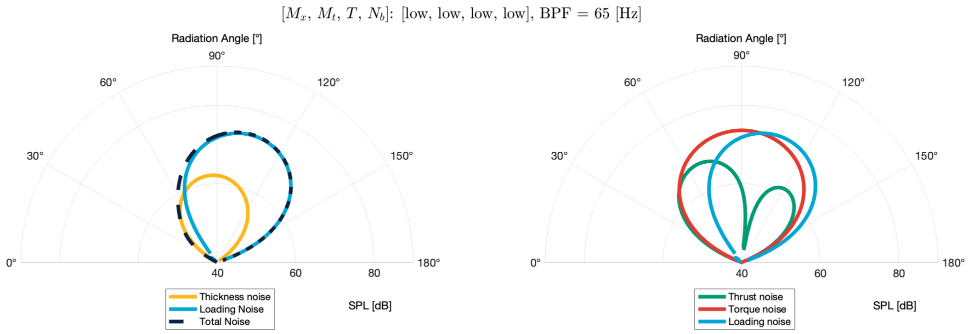

(a) Low M_t

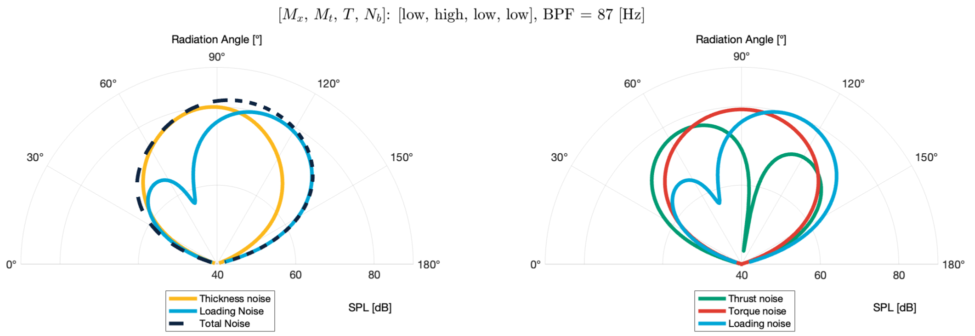

(b) High M_t

Figure 10.7: Comparison of Noise Sources of Straight Blade Runs with varying levels of Rotational Tip Mach Number (M_t)

As shown in Figure 10.7, the ratio of the two noise sources (thickness noise and loading noise) changes significantly with the value of M_t. At low values of M_t, the shift in blade loading causes change in the total noise reduction which can be noticed when comparing Figure 10.8 to Figure 10.7b. However, at high values of M_t, loading noise no longer dominates the total noise, and noise reduction is primarily driven by the effect of phase cancellation. While the Thrust thus changes the noise reduction at a low value of M_t, the Rotational Tip Mach Number still remains the dominant factor influencing the mechanisms of noise reduction. Note that in these figures, the total loading noise is at some range in the directivity lower than the torque or thrust noise, as these noise sources cancel each other at a directivity of more than 90° as seen in chapter 7 as well.

With the conclusion of the parameter study, significant knowledge has been gained regarding noise perception in propeller design. The next chapter builds on this foundation, and while doing so, it determines the starting conditions for executing the trade-off between reducing perceived noise and the additional power required to achieve it.

$[M_x,\ M_t,\ T,\ N_b]$: [low, high, high, low], BPF = 87 [Hz]

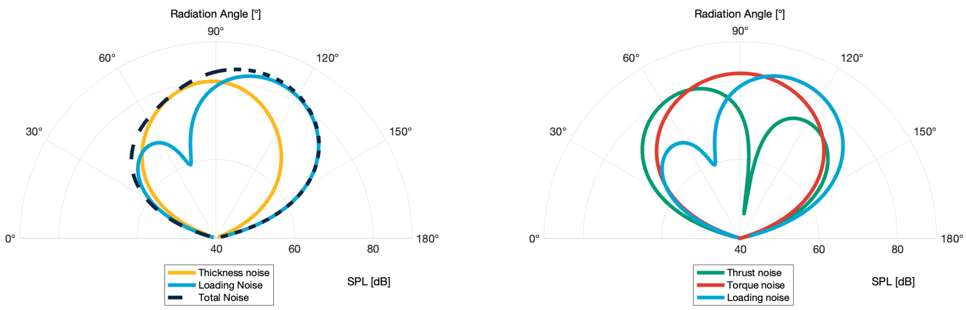

Figure 10.8: Comparison of Noise Sources of Straight Blade Runs with a high level of Thrust (T
)

11

OPTIMISATION

In this chapter, the results of the optimisation study are analysed and presented. The first two similar optimisations are done, resulting in propellers with a minimum required power. The difference in both runs is that one keeps the blade radius the same while the other keeps the blade length the same, which has been shown to produce quite different results. Starting from these two optimised propellers MPROP$^{\textbf{c-rad}}$ and MPROP$^{\textbf{c-len}}$, multiple trade-offs are done by means of Pareto fronts, analysing the relation between Effective Perceived Noise Level (EPNL) and a power penalty for reducing the EPNL. A first Pareto front is made, keeping the blade radius constant instead of the blade length. The extra length the blade obtained by increasing blade sweep reduces the noise significantly by reducing the blade loading. As this mechanism dominates the noise reduction with respect to phase cancellation, the rest of the analysis is done with a constant blade length to keep the blade loading constant. Three Pareto fronts are constructed with the constant length blade with different design vectors, starting only with the advance ratio and pitch, then twist distribution is added, and lastly sweep distribution. This is done to differentiate between different effects of reducing the noise to get a good understanding of the dominating mechanisms to reduce the EPNL. The same optimisations are also done with a physical noise equivalent metric, Effective Specific Noise Level, ESPL, as the objective to compare the resulting blades from optimising for perceived and physical noise. These optimisations and Pareto fronts provide much information regarding the mechanism used for reducing the EPNL, and also regarding the difference or lack of difference between optimising for physical versus perceived noise.

This chapter starts off with the results from the trade-offs that are done to provide insight into what reduction in EPNL can be achieved for a penalty in power required section 11.1. The different noise reduction mechanisms are looked at in section 11.2 to get a better view on how the optimisation algorithm uses different tools for noise reduction. section 11.3 shows results regarding the difference, or lack thereof, in optimising for physical noise and perceived noise by performing multiple optimisations with both EPNL and ESPL, which are objective to minimise. Then the most relevant optimisations are analysed in terms of resulting propeller geometry, parameter distributions, and blade stresses in section 11.4. The same is done for the resulting blade loading and harmonic content in section 11.5 to get a better understanding of why the Pareto fronts look as they do.

11.1. TRADE-OFF RESULTS

The results are of all the trade-offs that are done are shown in Figure 11.1, which also include the values of Effective Specific Noise Level (ESPL) which is the physical noise equivalent of EPNL as explained in chapter 9. In total, 4 Pareto fronts are constructed that all contain 3 points. The first point of all Pareto fronts is minimised P_{req} with the full design vector $\mathbf{x}: (J, \beta, \boldsymbol{\gamma}, \mathbf{MCA})$, optimised starting from the XPROP propeller. Respectively, for the constant length and constant radius propellers, the results are MPROP$^{\textbf{c-len}}$ and MPROP$^{\textbf{c-rad}}$. This approach is taken to differentiate between two noise-reducing effects when introducing blade sweep: blade sweep adds blade length when keeping the blade radius constant, thus lowering the blade loading, and secondly, when the blade length is constant, phase cancellation to reduce noise. From the MPROP$^{\textbf{c-rad}}$, one Pareto front is constructed, which uses the full design vector to minimise EPNL with constant blade radius, for which the PMPROP$^{\textbf{c-rad}}$ is the resulting propeller with the 2% power penalty. A similar Pareto

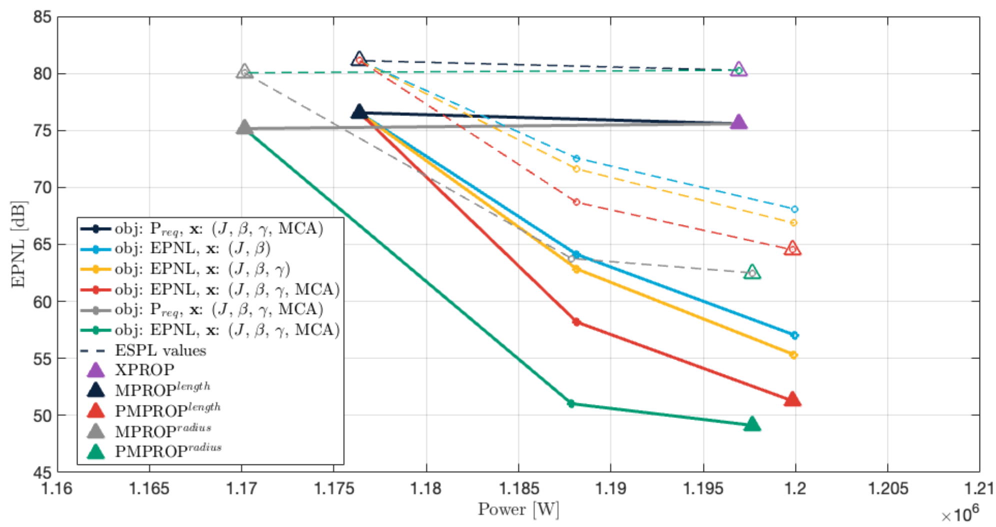

Figure 11.1: Pareto fronts for all optimisations, including respective ESPL values

front is constructed with a constant blade length, for which PMPROP$^{\textbf{c-len}}$ is the result, also with the 2% power penalty. The latter approach is taken to create two additional Pareto fronts to differentiate between two different mechanisms to reduce noise. The first is changing blade loading more inboard to reduce noise radiation efficiency, and the second is using the phase cancellation effect when applying blade sweep. The difference between the Pareto fronts using design vectors $\mathbf{x}:(J,\beta)$ and $\mathbf{x}:(J,\beta,\boldsymbol{\gamma})$ to asses the noise reduction through loading and the difference between the Pareto fronts using design vectors $\mathbf{x}:(J,\beta,\boldsymbol{\gamma}$ and $\mathbf{x}:(J,\beta,\boldsymbol{\gamma},\mathbf{MCA})$ to asses the noise reduction by applying blade sweep.

Start Prop	Resulting Prop	Objective	Design Vector	P_{req} $[MW]$	P_{req}/P_{req}^{MPROP}	Noise Reduction $\Delta EPNL$ [dB]	Noise Reduction $\Delta ESPL$ [dB]	Constraint activity $g_1(\mathbf{x}) \leq \sigma_{v-m}^{max}$	Constraint activity $g_2(\mathbf{x}) \leq P_{req}$
–	XPROP	P_{req}	J,β	1.1969	1.017	-1.0	-0.8	Inactive	NA
XPROP	MPROP$^{\textbf{c-len}}$	P_{req}	$J,\beta,\boldsymbol{\gamma},\mathbf{MCA}$	1.1764	1.000	0.0	0.0	Active	NA
XPROP	MPROP$^{\textbf{c-rad}}$	P_{req}	$J,\beta,\boldsymbol{\gamma},\mathbf{MCA}$	1.1701	0.995	-1.4	-1.1	Inactive	NA
MPROP$^{\textbf{c-len}}$	-	EPNL	J,β	1.1881	1.010	-12.4	-8.5	Active	Active
MPROP$^{\textbf{c-len}}$	-	EPNL	J,β	1.1999	1.020	-19.5	-13.0	Active	Active
MPROP$^{\textbf{c-len}}$	-	EPNL	$J,\beta,\boldsymbol{\gamma}$	1.1882	1.010	-13.7	-9.5	Active	Active
MPROP$^{\textbf{c-len}}$	-	EPNL	$J,\beta,\boldsymbol{\gamma}$	1.1999	1.020	-21.2	-14.3	Active	Active
MPROP$^{\textbf{c-len}}$	-	EPNL	$J,\beta,\boldsymbol{\gamma},\mathbf{MCA}$	1.1882	1.010	-18.4	-12.4	Active	Active
MPROP$^{\textbf{c-len}}$	PMPROP$^{\textbf{c-len}}$	EPNL	$J,\beta,\boldsymbol{\gamma},\mathbf{MCA}$	1.1998	1.020	-25.3	-16.6	Active	Active
MPROP$^{\textbf{c-rad}}$	-	EPNL	$J,\beta,\boldsymbol{\gamma},\mathbf{MCA}$	1.1879	1.010	-25.5	-17.4	Active	Active
MPROP$^{\textbf{c-rad}}$	PMPROP$^{\textbf{c-rad}}$	EPNL	$J,\beta,\boldsymbol{\gamma},\mathbf{MCA}$	1.1977	1.018	-27.4	-18.6	Active	Inactive

Table 11.1: Results of optimisation runs

Table 11.1 presents the results from all the optimisation runs that are present in the Pareto fronts. The MPROP$^{\textbf{c-len}}$ is used as the reference noise levels, as most Pareto fronts use this propeller as a starting point. From these results, a big difference is found between the perceived noise and physical noise, represented respectively by ESPL and EPNL. Looking at the results for the constant blade radius optimisation, the reduction in EPNL for PMPROP$^{\textbf{c-rad}}$ is 27.4 dB, while for ESPL, this is only 18.6 dB. For the rest of the results, a similar difference is found.

11.2. NOISE REDUCTION MECHANISMS

Figure 11.2 presents a more detailed look at the difference in noise reduction. With this information, an assessment can be made of what noise reduction mechanisms are dominating for the trade-offs that are performed.

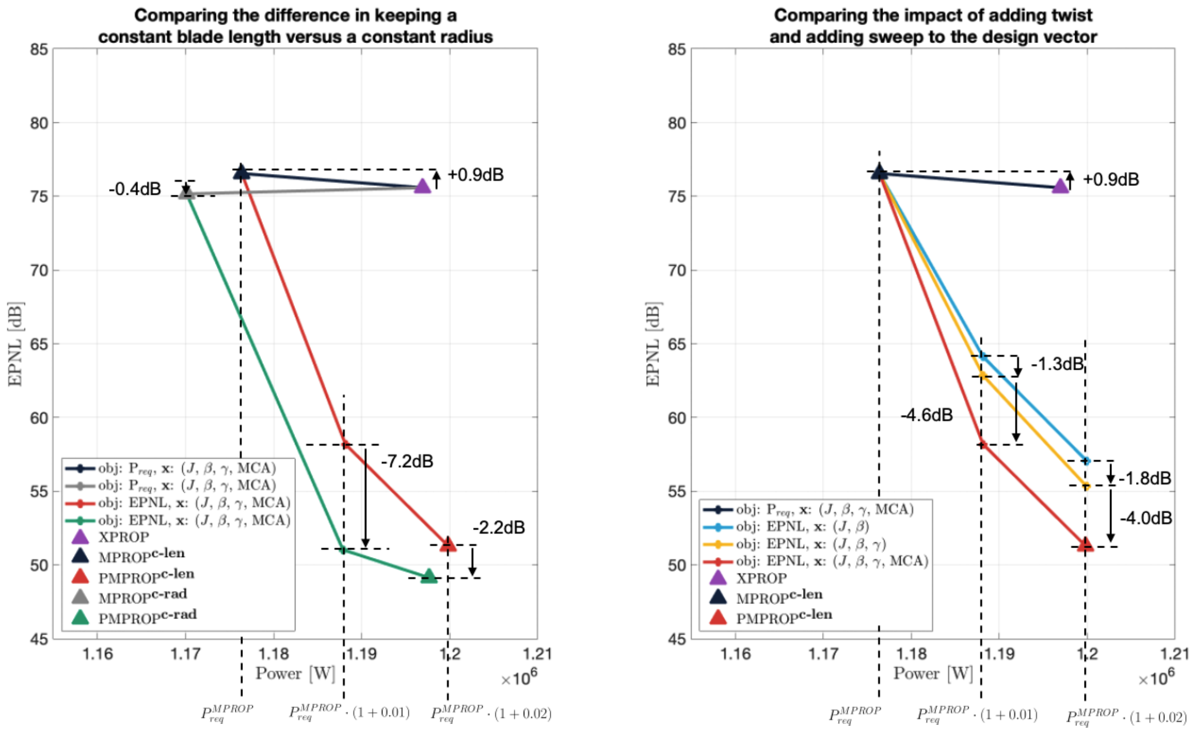

Figure 11.2: Pareto fronts and the reduction that is achieved due to different noise reduction mechanisms by a different blade constraint (left) and different design vectors (right)

11.2.1. CONSTANT BLADE LENGTH VERSUS CONSTANT BLADE RADIUS OPTIMISATIONS

Working from the starting XPROP to the optimisations with the maximum power penalty, an immediate difference appears between the constant blade radius and constant blade length optimisations. While MPROP**c-rad**, which maintains a constant blade radius, already shows a noise reduction of -0.4 dB with respect to the XPROP while MPROP**c-len** shows a slight increase of 0.9 dB.

Looking at the actual trade-offs through the Pareto fronts that are present in the left on Figure 11.2 the constant radius optimisation show a -7.2 dB noise reduction for a similar power penalty (w.r.t. the required power of the MPROP**c-rad**) when compared to the constant blade length optimisation. Further increasing the power penalty, the resulting EPNL of the PMPROP**c-len** approaches that of the PMPROP**c-rad** but remains significant. Important to note is that in the optimisation of the MPROP**c-rad** the required power inequality is not active as shown in Table 11.1 meaning that applying an extra penalty would not enhance noise reduction.

11.2.2. DIFFERENT DESIGN VECTORS FOR CONSTANT BLADE LENGTH OPTIMISATIONS

On the right of Figure 11.2 the Pareto fronts are shown where different design vectors are used to result in multiple trade-offs which can be used to differentiate between multiple noise reduction mechanisms when including blade sweep in propeller design. Comparing For both a power penalty of 1% and 2%, similar results are present. Comparing the Pareto front with design vectors $\mathbf{x}:(J,\beta)$ and $\mathbf{x}:(J,\beta,\boldsymbol{\gamma})$ the difference is only 1.3 dB to 1.8 dB in noise reduction when adding twist distribution to the design vector. This shows that in the trade-off between EPNL and required power, changing only the operating settings (J,β) is enough to realise the biggest part of the noise reduction. Comparing this to optimising with the full design vector, $\mathbf{x}:(J,\beta,\boldsymbol{\gamma},\mathbf{MCA})$ which results in PMPROP**c-len** , a bigger difference is seen. A difference of -4.6 dB to -4 dB for respectively +1% and +2% required power shows that adding a sweep to the propeller blade can result in a significant noise reduction, even more so than optimising the loading distribution.

11.3. OPTIMISING EPNL VERSUS ESPL

To analyse the difference in the optimisation result when designing a propeller for perceived noise or physical noise, the most relevant points in the Pareto fronts, which are optimised for minimum EPNL, are optimised for the physical noise equivalent Effective Specific Noise Level (ESPL). The points that are taken to do so are the optimised propellers with the maximum power penalty of 2% on the Pareto fronts with the constant blade length optimisations. These points are taken as the maximum difference in resulting blade geometry is expected for optimising PMPROP$^{\textbf{c-len}}$ for EPNL. The reason for this is that the respective propeller optimised for constant blade radius shows a dominating effect of lengthening the blade for minimum blade loading as discussed in section 11.5 and thus with a constant blade length, other noise reducing mechanisms can be better observed which can lead to a difference in results for this part of the study. The other two comparisons with the other, smaller, design vector are done to get a better understanding at this subject.

Design vector (and resulting prop)	Objective	P_{req} $[MW]$	$EPNL[dB]$	$ESPL[dB]$
$\mathbf{x}:(J,\beta)$	EPNL	1.199	57.05	68.11
	ESPL	1.199	57.04	68.10
$\mathbf{x}:(J,\beta,\boldsymbol{\gamma})$	EPNL	1.199	55.33	66.86
	ESPL	1.199	55.34	66.86
$\mathbf{x}:(J,\beta,\boldsymbol{\gamma},\mathbf{MCA})$,PMPROP$^{\textbf{c-len}}$	EPNL	1.199	51.28	64.53
	ESPL	1.199	51.21	64.47

Table 11.2: Comparison of noise optimisation when optimising EPNL versus the physical noise equivalent ESPL for the constant blade length configurations with the maximum power penalty.

Table 11.2 shows the results for optimising both EPNL and ESPL for the different design vectors. The difference between the optimised EPNL and ESPL is very small and can be deemed insignificant. A clear remark can be made about these results, which is that it does not matter for which of these metrics the propeller is optimised; the results are the same. However, the values of EPNL are reduced more than the values of ESPL, as shown before, but it does not matter for which of those specific metrics the propeller is optimised for. A note has to be made that this could be local optima and for now, no certain proof can be given, but multiple other optimisations have been performed that minimise ESPL from different starting points, and the results have not once confirmed a different resulting blade geometry or different aeroacoustic results.

11.4. RESULTING PROPELLERS

To get a better understanding of the different Trade-Offs and aeroacoustic effects, the following four pages contain the resulting propellers, blade parameter distribution, and blade stress of the optimisations that are most relevant to analyse. The first page withFigure 11.3 shows the power optimisation with the constant blade radius propeller. After that, the propeller optimisation is shown from MPROP$^{\textbf{c-rad}}$ to PMPROP$^{\textbf{c-rad}}$ and then the constant blade length optimisation is shown from MPROP$^{\textbf{c-len}}$ to PMPROP$^{\textbf{c-len}}$. The last page contains the optimised blades' twist distribution for the runs with different design vectors $\mathbf{x}:(J,\beta)$ and $\mathbf{x}:(J,\beta,\boldsymbol{\gamma})$.

Comparing the blade shapes, which are changing because of a different sweep distribution, the geometries of PMPROP$^{\textbf{c-rad}}$ and PMPROP$^{\textbf{c-len}}$ are quite different. While they both try to maximise blade sweep such that the stress constraints are active, they do so in different ways. In the constant radius optimisation,Figure 11.4, the sweep is maximised over the entire blade, with a maximum MCA at about half of the span while the twist is increased at the hub. In the constant blade length optimisation in Figure 11.5, the sweep is maximised at the tip while the twist distribution is very similar to the optimised twist in Figure 11.6 where only the blade twist is optimised.

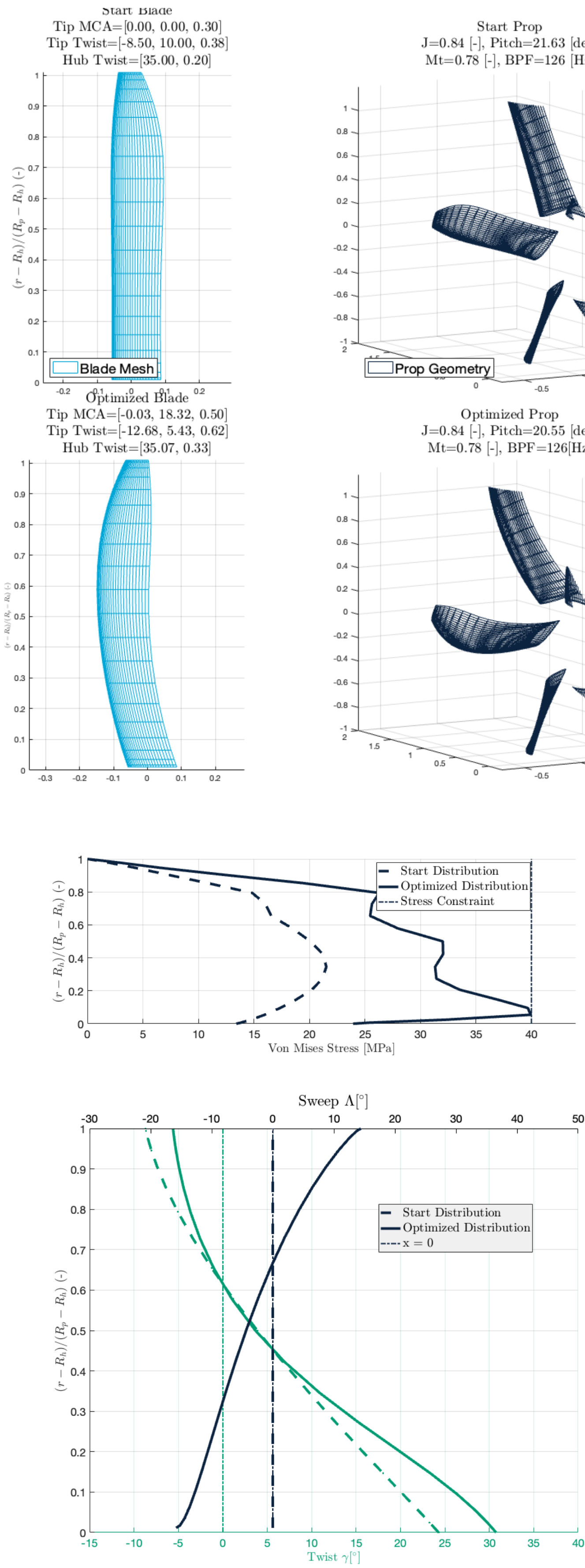

Figure 11.3: XPROP to MPROP$^{\textbf{c-rad}}$ optimisation. Objective is minimising power required. (Top) blade and propeller geometries, (middle) maximum sectional Von Mises Stresses, (bottom) Sweep and twist distributions

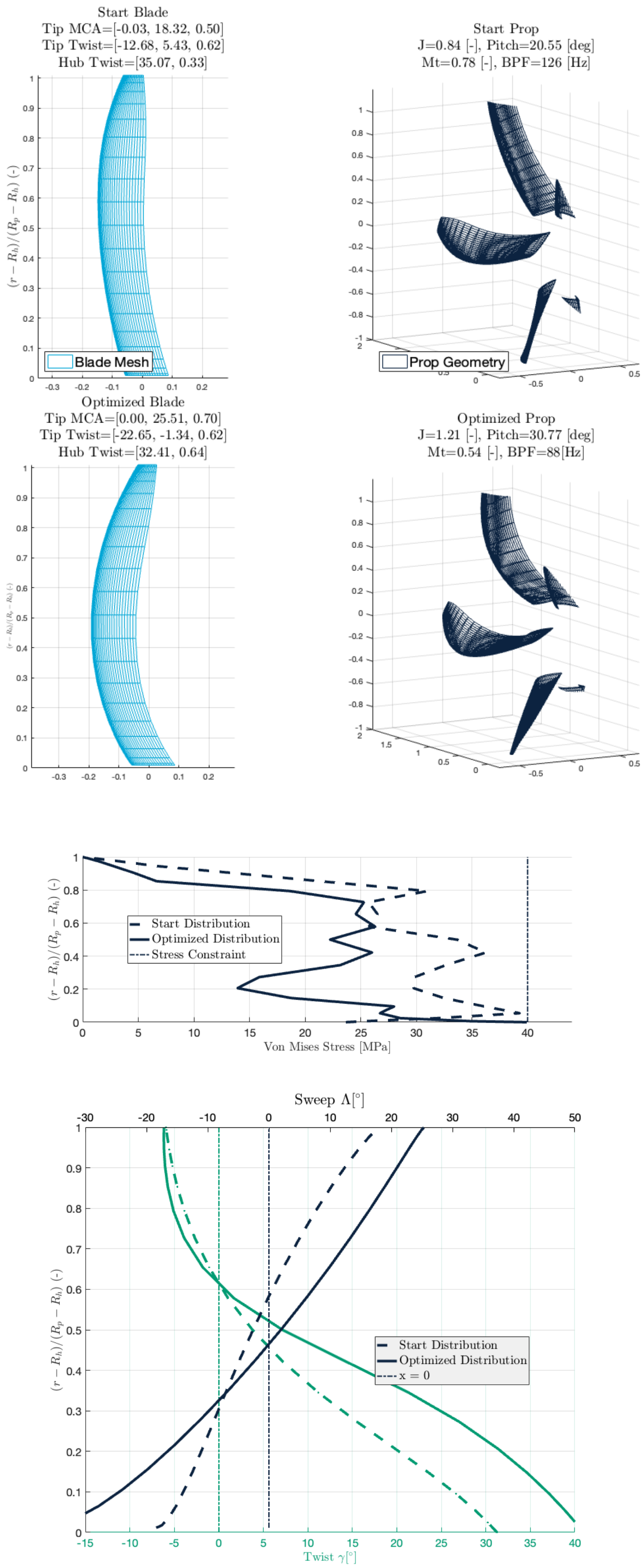

Figure 11.4: MPROP**c-rad** to PMPROP**c-rad** optimisation. Objective is minimising EPNL. (Top) blade and propeller geometries, (middle) maximum sectional Von Mises Stresses, (bottom) Sweep and twist distributions

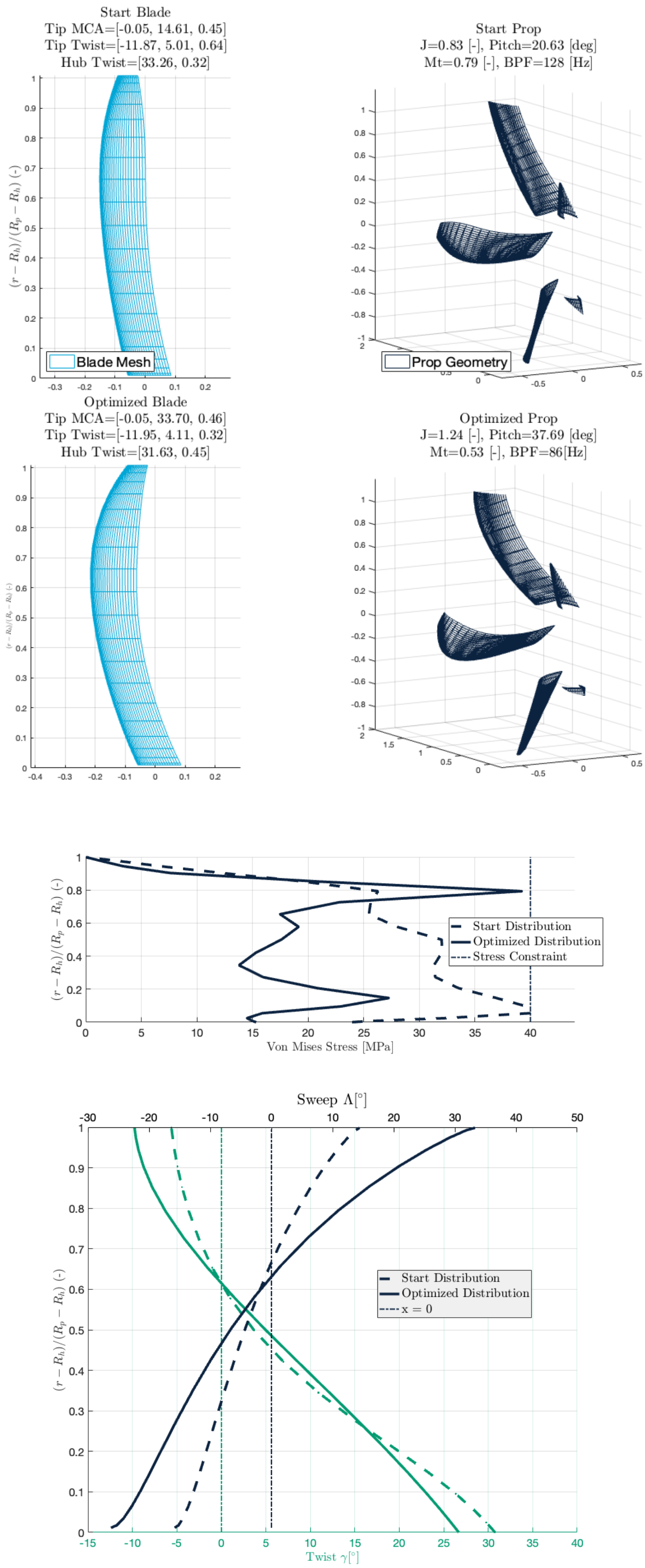

Figure 11.5: MPROP$^{\textbf{c-len}}$ to PMPROP$^{\textbf{c-len}}$ optimisation. Objective is minimising EPNL. (Top) blade and propeller geometries, (middle) maximum sectional Von Mises Stresses, (bottom) Sweep and twist distributions

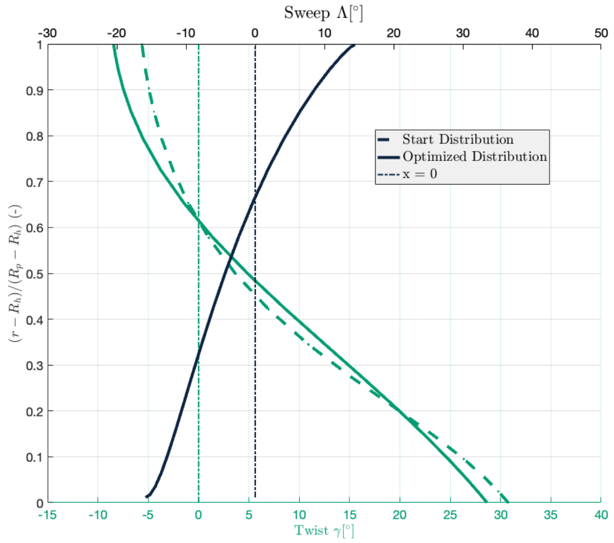

Figure 11.6: Twist distributions for the different optimisation runs for design vectors $\mathbf{x}:(J,\beta)$ as the "start" and $\mathbf{x}:(J,\beta,\boldsymbol{\gamma})$ as the "optimised" distribution for the +2% power penalty

11.5. Detailed aeroacoustics

To get a view on how the optimised propellers reduce EPNL, this section assesses the detailed aeroacoustics. More specifically, the harmonic content of all optimised propeller results is shown as well as the blade loading.

Figure 11.7 shows the resulting blade loading for all the relevant optimised propellers. The most significant difference can be seen when comparing the sectional thrust per blade of the constant blade radius (MPROP$^{\textbf{c-rad}}$ and PMPROP$^{\textbf{c-rad}}$) with the constant blade length (MPROP$^{\textbf{c-len}}$ and PMPROP$^{\textbf{c-len}}$) in the lower left figure. Because the absolute thrust level is constant across all the propellers, the integration over the sectional thrust over the blade span gives the thrust per blade. The constant blade radius optimisation increases blade length with additional blade sweep and can lower the sectional thrust in this way. As a result, the maximum sectional thrust (and also torque) is significantly lower when allowing the blade length to vary which explains the increased noise reduction for PMPROP$^{\textbf{c-rad}}$ when compared to PMPROP$^{\textbf{c-len}}$ in section 11.1. Interesting to note is that the shape of the blade loading graphs are similar for the optimised power and optimised EPNL for constant blade length case which explains why changing only the advance ratio and pitch can already reduce noise in an efficient way and little change has to be done to the twist distribution for the additional minimisation of noise.

Figure 11.8 show the difference in harmonic content for comparison of the two trade-offs with constant blade radius and length together with the harmonic content of the XPROP and minimised required power propellers MPROP$^{\textbf{c-rad}}$ and MPROP$^{\textbf{c-len}}$. Two significant effects dominate these results. First, minimising the rotational velocity is the main way of reducing noise; the minimised EPNL results both show that the Blade Passage Frequency (BPF) is significantly reduced. As this reduces noise radiation, the amplitude of the harmonics decreases, and because lower harmonics have a lower weight through the conversion of physical to perceived noise, the difference between the PNL and SPL levels increases. The latter is clearly noticed in the difference in Pareto front between the ESPL and EPNL values in section 11.1. What is also noteworthy is that the optimal BPF of the PMPROP$^{\textbf{c-rad}}$ is higher than that of the PMPROP$^{\textbf{c-len}}$. Connecting the remark about blade loading that has just been made, a higher rotational velocity can provide a higher blade sweep, and thus blade length, as the stress constraint is easier to meet with a higher rotational velocity.

The second significant effect is that because the rotational velocity decreases, the harmonic envelope steepens and thus the fundamental frequency becomes more important, even though the higher harmonics are weighted higher. This causes a direct decrease in the noise reduction that sweep can wield on the total noise reduction as sweep-induced noise reduction increases for lower wavelengths. Figure 11.9 shows the harmonic content from the constant blade length optimisations with varying design vector. The results show a similar trend as present in Figure 11.8. Comparing the harmonic content of the run with the design vector

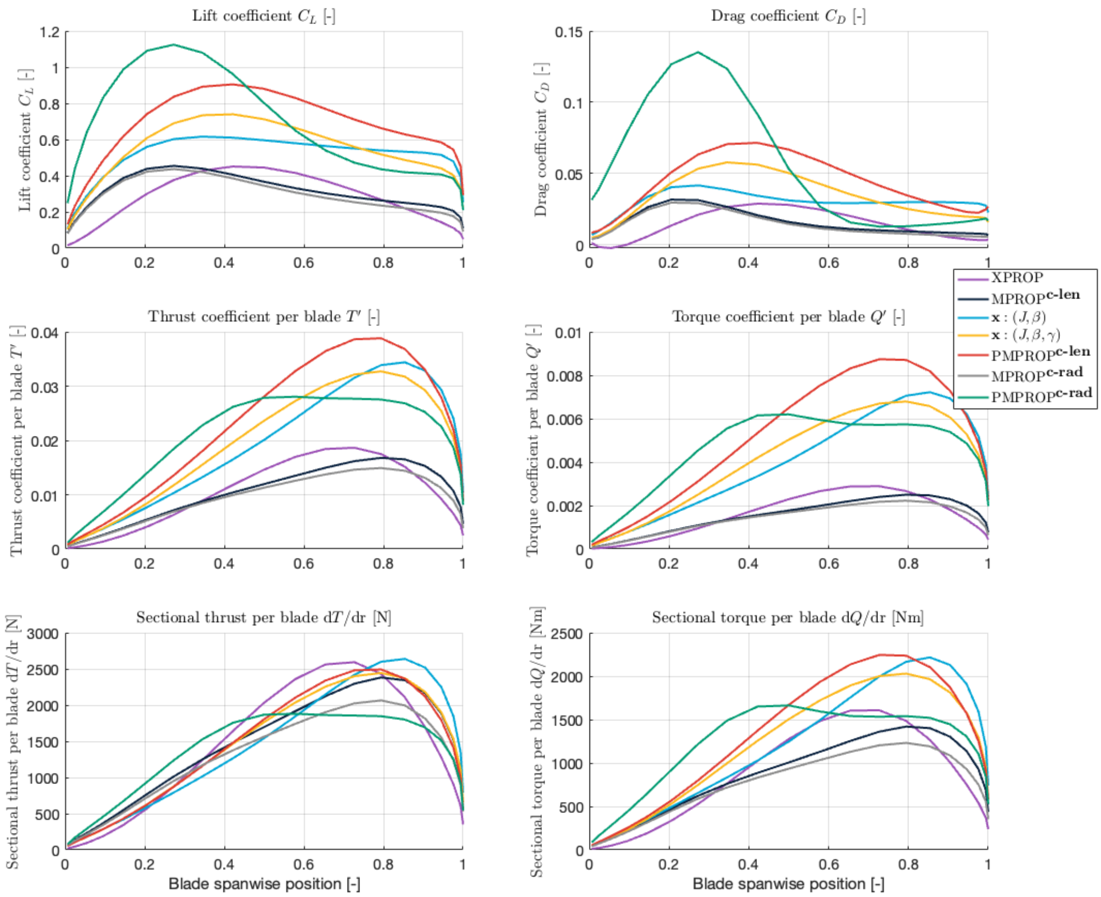

Figure 11.7: Comparison of blade loading of the starting propeller (XPROP), both power optimised propellers (MPROP$^{\textbf{c-len\&c-rad}}$) and all final EPNL optimised propellers with a power penalty of 2%

$\mathbf{x}:(J,\beta,\boldsymbol{\gamma})$ shows very little difference, where only the amplitudes across all harmonics decrease slightly by the same fraction. Looking at the optimisation with the total design vector, which results in PMPROP$^{\textbf{c-len}}$, it is interesting to see that the rotational velocity can be decreased even further, which, together with the phase cancellation, reduces the noise by a significant amount.

Building on the knowledge gained in the parameter study in chapter 8, the results from this optimisation study yield key takeaways that support propeller research in general and provide lessons applicable to propeller design. The following part does so while addressing the research questions and concludes the study.

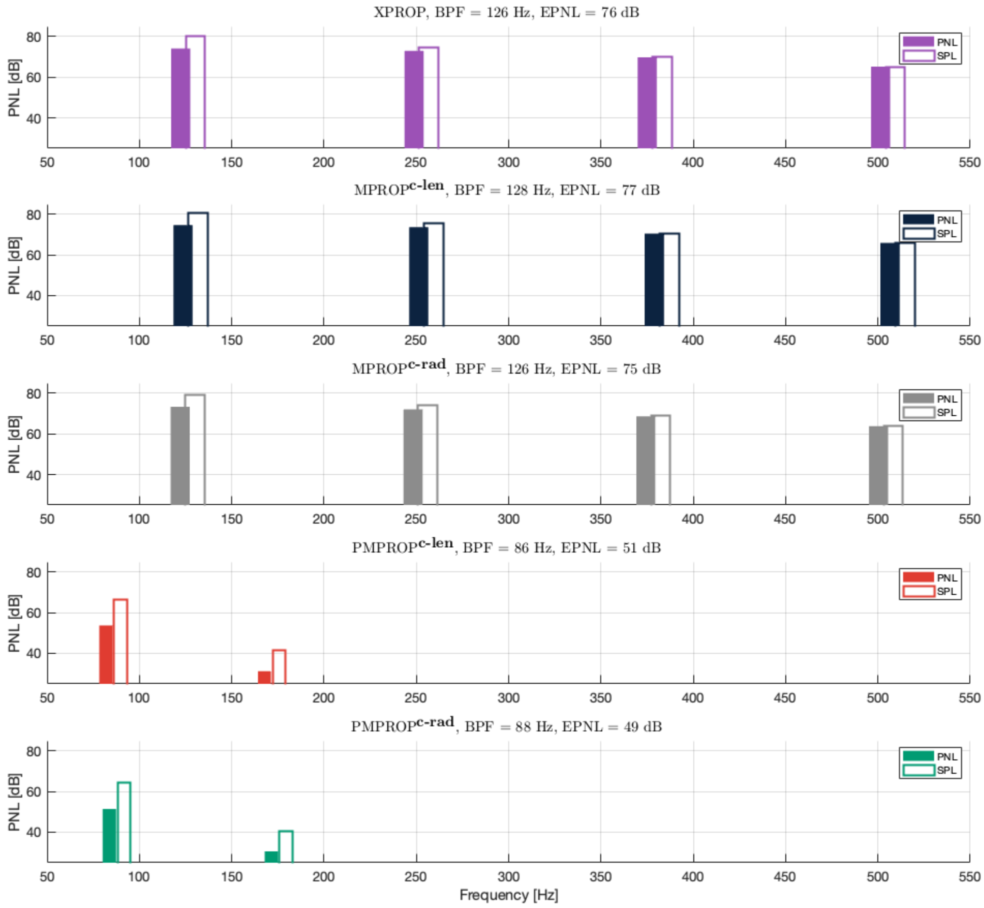

Figure 11.8: Physical noise and perceived noise levels of harmonic content, comparing the starting propeller (XPROP), both power optimised propellers (MPROP$^{\textbf{c-len\&c-rad}}$) and both final EPNL optimised propellers (PMPROP$^{\textbf{c-len\&c-rad}}$)

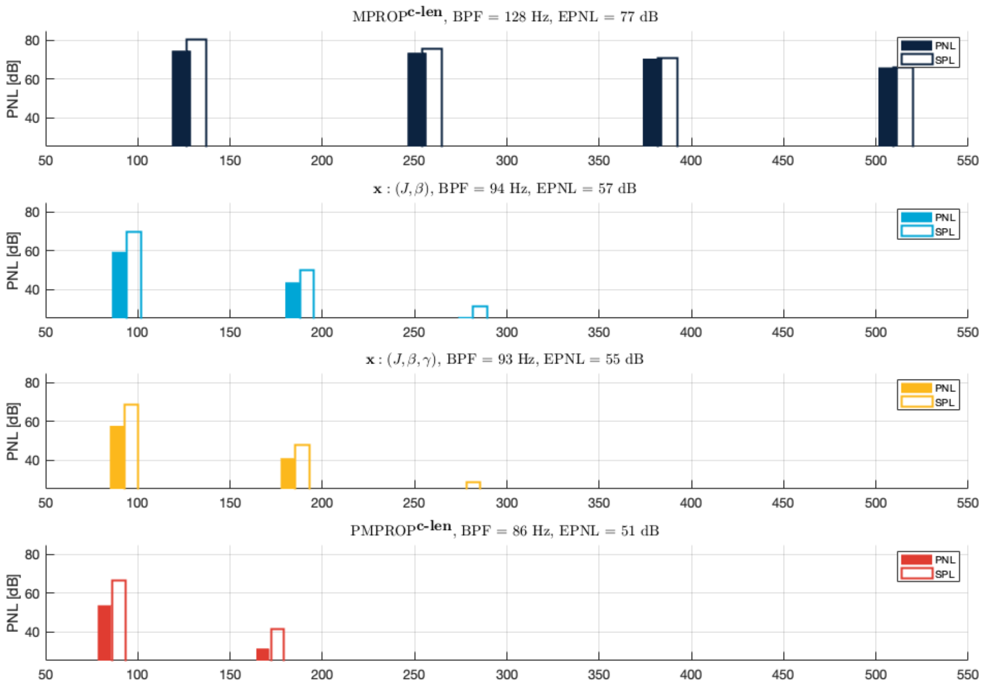

Figure 11.9: Physical noise and perceived noise levels of harmonic spectrum, comparing the power optimised propellers(MPROP$^{\text{c-len}}$) and final EPNL optimised propellers with a power penalty of 2%

V

KEY FINDINGS AND RECOMMENDATIONS

12

Conclusions

The conclusions are divided into two parts to obtain the key findings that contribute to the research objective. First, the research questions are addressed with thorough justification, as they represent the direct goals of the study. In addition, several findings emerged that, while not directly answering the research questions, contribute valuable insights to the broader field and may be used in future propeller design and research. For clarity, the research objective is reiterated, and the research questions are presented before being answered.

> Research Objective
>
> **Quantify the impact of optimising blade sweep for minimised perceived noise**

12.1. Answering Research Questions

To establish a foundation for achieving the research objective, the following research questions are addressed to guide the first part of this study. Noted are two things: the first research question focuses the study specifically on take-off conditions, and therefore, the answers to the subsequent research questions also apply to those conditions.

> Research Question 1
>
> **How do operating conditions (and blade count) influence the sweep-induced reduction of perceived noise?**
> This question will be addressed through the following sub-questions:
> 1. At which flight condition is including noise perception in propeller design the most relevant?
> 2. Which parameters have the most influence on sweep-induced (perceived) noise reduction, and what is the most significant difference in response between physical and perceived noise?
> 3. What role does harmonic noise play in these trends?

1. Comparing the most relevant flight conditions for noise reduction—take-off and cruise—it is found that incorporating noise perception during take-off has the most significant impact. During take-off, the higher rotational velocity leads to a more substantial presence of harmonics in the harmonic content. At the same time, blade sweep is more effective at reducing high-frequency noise, thereby having a greater impact under these conditions. Since noise perception assigns more weight to higher frequencies, a significant difference emerges between sweep-induced reductions in physical and perceived noise during take-off, whereas in cruise conditions, this difference is negligible. Subsequently, the rest of the study thus focuses specifically on take-off conditions to maintain relevance.

2. The parameters found to have the most significant influence on sweep-induced perceived noise reduction are the tip Rotational Mach number and the number of blades, both of which also strongly affect the absolute noise levels, an effect that dominates over the sweep-induced noise reduction. This dominance will show great significance in the optimisation study. The other two parameters examined in

this study—thrust and flight Mach number—were found to have an insignificant effect on both sweep-induced noise reduction and absolute noise levels, and show little difference in trends when comparing physical and perceived noise.
Increasing the rotational velocity enhances sweep-induced perceived noise reduction when blade sweep is introduced (with pitch adjusted to maintain constant thrust). This kind of noise reduction is referred to as sweep-induced noise reduction. In contrast, physical noise reduction diminishes due to a less favourable load distribution. Although this unfavourable loading also affects sweep-induced perceived noise reduction, the dominant mechanism in the perceived noise case is the reduction of high-frequency harmonic noise, weighted more heavily in perceived noise, which wins over the negative impact of the load distribution. While the difference between perceived and physical noise reduction increases with higher rotational velocity, the absolute level of noise increases, both with and without blade sweep, which is an effect an order of magnitude higher than sweep-induced noise reduction. Regarding blade count, both perceived and physical noise reduction follow similar trends: at a high tip rotational Mach number, increasing the number of blades improves sweep-induced noise reduction, whereas at a low tip rotational Mach number, it reduces it. This is because a higher blade count increases the effectiveness of sweep in attenuating noise, but only with a high tip rotational Mach number when high-frequency harmonics make up a significant portion of the total noise. Looking at absolute noise levels, a higher number of blades is favourable for lower noise due to a lower blade loading.

3. The role harmonic noise plays in sweep-induced noise reduction depends on how heavily they are represented in the harmonic content and the value of the Blade Passage Frequency (BPF). The more the harmonics are represented in the total noise, the higher the difference between sweep-induced reduction of perceived and physical noise. The higher the Blade Passage Frequency, and thus the frequency of all harmonics, the more effectively blade sweep can reduce the harmonic noise, and thus reduce the total (tonal) noise level. A higher tip rotational Mach number (with a constant thrust) increases harmonic noise and increases the BPF, which both lead to more effective sweep-induced noise reduction. Increasing the number of blades only increases sweep-induced noise reduction when the harmonics are well represented in the harmonic content. On the one hand, an increase in the number of blades causes an increase in BPF, which is favourable for sweep-induced noise reduction; however, it reduces the presence of harmonic noise, which has an opposite effect. Generally, the number of blades increases sweep-induced noise reduction for perceived noise (when compared to physical noise) and also at a higher tip Rotational Mach number.

These conclusions from the first part of this study provide knowledge that acts as a toolbox and starting point to use in the optimisation study that followed. Because in take-off conditions, a significant difference has been found between perceived noise and physical—especially in the sweep-induced reduction thereof—propeller optimisation is done conform to perceived noise certification in ICAO Annex 16, Volume I at take-off. As expected from past research, the number of blades reduces the absolute (tonal) perceived noise level; a number of six blades is used to ensure a relevant study is performed.

Subsequently, the next research questions are addressed.

Research Question 2

How does blade sweep contribute to the trade-off between Effective Perceived Noise Level and required power?
This question will be addressed through the following sub-question:
1. What is the difference in the resulting sweep distribution when optimising Effective Perceived Noise Level and the physical noise equivalent?
2. In the trade-off between Effective Perceived Noise Level and required power, what is the difference in contribution of blade sweep and blade loading (distribution)?

1. Looking at designing a propeller for reduced Effective Perceived Noise Level (EPNL) or a physical noise equivalent metric, Effective Sound Pressure Level (ESPL, defined in this study), the difference in the resulting propeller geometry is negligible. The main tool to reduce noise is to reduce the rotational speed, after which the blade sweep begins to play a significant role. With a lower rotational velocity and thus Blade Passage Frequency, the harmonic envelope steepens and the relative importance of the fundamental frequency significantly increase. While for perceived noise, the fundamental frequency

is weighted less, as humans perceive such frequencies as being less loud and thus increasing the relevance of higher frequencies, the steepening of the harmonic envelope is the dominating effect. This means that for optimising both minimised EPNL and ESPL, the main tool to reduce both metrics is to reduce the amplitude of the fundamental frequency, for which the mechanisms to do so are the same in both cases. Thus, this results in the same blade geometries when using EPNL or ESPL as an objective to minimise. While there is no difference in optimising the propeller for minimised perceived or physical noise, the trade-off between reduced EPNL and ESPL with required power is indeed different to each other. Reducing the rotational velocity of a propeller decreases the Blade Passage Frequency (BPF), which in turn lowers the frequency of the tonal noise components. Since human hearing is less sensitive to lower frequencies, this reduction leads to a more significant decrease in perceived noise compared to physical noise. Consequently, for a 1% increase in required power, the additional reduction in perceived noise is on average (in this study) 5.55 dB, and for a 2% power increase, the reduction is about 7.72 dB.

2. In the trade-off between EPNL and required power, the optimisation algorithm exploits multiple noise reduction mechanisms. The different types of mechanisms analysed in this research are changing the sweep distribution to reduce noise and changing the blade loading to reduce noise, which is done by giving freedom over the blade twist. To differentiate between the effect of blade sweep and blade loading, three Pareto fronts were built with constant blade length and afterwards an additional Pareto front with constant blade radius, as with a constant radius, increasing blade sweep effectively elongates the blade, which reduces blade loading. In the constant blade length optimisations, the first Pareto front has freedom over only the advance ratio and pitch, the next adds blade twist distribution to have freedom over blade loading, and the last front adds blade sweep, which results in the total design vector used in this study. The first Pareto front, having freedom over advance ratio and pitch, achieves a perceived noise reduction of -12.4 dB to -19.5 dB with a power penalty of respectively 1% and 2%-from a power optimised propeller as reference—achieved by increasing blade loading to reduce rotational velocity which has already proven to be a very successful mechanism in reducing noise. Adding the freedom in blade twist distribution only reduced the noise by -1.3 db and -1.8 db, respectively. This is done by shifting the load more inboard and reducing the rotational velocity. Adding blade sweep to the design vector enhances further noise reduction by -4.6 dB to -4 dB with a power penalty of respectively 1% and 2%. This shows that adding blade sweep can prove to be more effective at reducing noise than adjusting the blade loading (from an already power-requiring minimised propeller).

   The last Pareto front does the same optimisation process with the whole design vector—advance ratio, pitch, twist distribution and sweep distribution—with a constant blade radius, which leaves room for the blade length to increase with added sweep distribution. This has been shown to have a significant effect on noise reduction. As the blade sweep can be used to reduce noise with the mechanisms already explored in the constant blade length runs, the sweep is also used to increase the blade length, which directly reduces the blade load. The resulting extra noise decrease compared to the constant blade length Pareto front is -7.2 dB and -2.2 dB, respectively, for the power penalties of 1% and 2%.

12.2. OTHER KEY REMARKS

While doing this study, some extra conclusions can be made that don't necessarily answer the research questions. These findings are mentioned below:

- When changing the sweep distribution while leaving the rest of the blade geometry the same, an unfavourable load distribution leads to less effective noise reduction. The rest of the blade geometry has to be optimised as well in order for the sweep to be efficiently introduced. Using the blade twist has proven to be an efficient way of doing so.

- In propeller design for noise reduction, a key decision involves constraining either the blade radius or the blade length. If the blade length is allowed to vary while the radius remains fixed, both the required power and blade noise can be reduced with respect to the constant blade case. However, a more curved blade through sweep distribution makes it harder to meet structural constraints—which become the dominant limitation when accepting higher power penalties for noise reduction. Alternatively, keeping the blade length constant still allows for significant noise reduction, though to a lesser degree. Since this approach primarily relies on tip sweep, it eases structural constraints. As a result, accepting a higher power penalty for noise reduction becomes a more efficient strategy—not only lowering noise but also reducing blade weight.

- As the Pareto fronts in this study contain three points, their shape can be approximated. Doing so, it can be seen that more noise is reduced at the start of the Pareto fronts. This means that more noise can be reduced
- When thickness noise dominates the tonal noise over the loading noise, phase cancellation becomes the main noise reducing mechanism as the tonal noise level cannot be (significantly) reduced when changing the load distribution.

12.3. DISCUSSION

This section reflects on the key findings from the parameter and optimisation studies, with a focus on their implications for propeller design. Some comparison is made with the referenced work, putting some of the conclusions that were made before in the frame of reference.

The optimisations in this study are done while predicting the required power for take-off conditions. This means that the results do not give a fair comparison to a full flight mission, but rather provide an optimal scenario when optimising the propeller for take-off. A comparison can be made with past literature to gain insight into how the results in this research can be used to approximate results for a full flight mission. The work of Margalida [36] does so while conducting similar optimisations, which also use a Pareto front which varies the advance ratio and pitch. For a power penalty of 1% in this study, a noise reduction of -8.5 dB is shown, whereas optimising for the full flight mission yields a reduction of -5 dB. Using Margalida's work, a reference framework is provided for this work to be used in a more broadly applicable way.

A second remark can be made regarding the second Pareto front executed in Margalida's work, as he adds freedom to the chord and twist distribution. Comparing our work, it can be speculated that freedom over the blade chord significantly enhances noise reduction when compared to using blade twist to do so. Additionally, modifying blade sweep alters the effective chord length measured orthogonally to the mid-chord line. If a reduced chord length is as beneficial for noise reduction as Margalida has proven, blade sweep becomes a tool to not only lengthen the blade but also effectively reduce chord length. While in this study, tonal noise is considered the only source of noise, broadband noise can significantly change such optimisations. Especially when the rotational velocity increases, the broadband noise can take over as the dominant source of noise [9].

While this work focuses solely on tonal noise, no information has been obtained regarding the effect of blade sweep on broadband noise. Although blade sweep has been shown in this study to reduce tonal noise, its influence on broadband noise remains unknown. A similar limitation arises when translating results from this analytical study to experimental testing. As previously observed, a propeller optimised for reduced noise does not necessarily result in a significantly lower noise level in wind tunnel experiments [40].

Regarding the aerodynamic modelling in this work, the Vortex Lattice Method (VLM) has not been thoroughly validated for imposing great amounts of blade sweep. Therefore, while the obtained results should not be considered accurate enough to do actual blade design with, they are sufficient to support the conclusions drawn in this study.

Looking at the results obtained in the optimisation study, no analysis was done to check whether the found optima were indeed the global optima. While the conclusions in this study hold regardless, details in the blade geometry could vary, and so could the aeroacoustic results.

13

Recommendations

Some recommendations for future research and propeller design are presented below, followed by specific suggestions for a potential optimisation study.

In the parameter study, the tip rotational Mach number is used to determine the rotational velocity to ensure constant tip velocities and non-divergent compressibility effects; however, in further study, the advance ratio is advised to be used, especially when taking propeller diameter into account.

This ensures a better comparison and a broader applicability of such a study. For further research, when comparing either Perceived Noise Level (PNL) or Effective Perceived Noise Level (EPNL) to physical noise, it is advised to use maximum Overall Specific Pressure Level (OSPL) as the metric of choice. While this study uses other metrics, OSPL gives a better comparison to existing literature and is a good representative of the noise level that one would want to design a propeller for.

While this study demonstrates multiple mechanisms to reduce (perceived) noise specifically for aircraft propellers, some of these approaches can also be applied to quadcopter or other types of drone propellers. A follow-up study is recommended to investigate perceived noise reduction for smaller drone-type propellers, building upon the findings of this research.

When considering noise perception in propeller design, an increase in the Number of Blades results in less perceived noise reduction compared to the reduction observed for physical noise. This could justify choosing fewer blades for a propeller, especially at higher rotational velocity. Additional propeller optimisation research could further study this.

As this particular study focused acquiring knowledge about including noise perception in propeller design and did an optimisation study specifically regarding take-off conditions a next study is recommended to do a more thorough optimisation and design research that includes an entire flight mission. The following points give recommendations about such research:

- While this study only focuses on take-off conditions, it would be interesting to see how these conclusions would hold up when optimising a propeller for an entire flight mission.
- In general, an optimisation study that encompasses more design freedom can give a better view of propeller design choices, resulting in noise reduction, for example, including freedom in propeller diameter, number of blades and number of propellers, chord length distribution, etc.
- In such a study, different design choices could be investigated regarding a constant radius or constant length propeller blade.
- A simplified yet sufficiently accurate structural model is recommended for future optimisation studies to reduce computational effort and complexity. Another option would be to use a structural model similar to the one employed in this study, but with more thorough validation for complex blade shapes and adaptation to make it more suitable for optimisation algorithms.

- Further work is required as well to investigate the global optimality of such optimisation results. A more comprehensive exploration of the design space and additional validation of the optimisation strategy are advised.

Bibliography

[1] P. Alves, M. Silvestre, and P. Gamboa, *Aircraft Propellers—Is There a Future?* Energies **13**, 4157 (2020), number: 16 Publisher: Multidisciplinary Digital Publishing Institute.

[2] F. A. Administration, *AC 36-4D - Noise Standards: Aircraft Type and Airworthiness Certification*, Tech. Rep. (Federal Aviation Administration (FAA), 2017).

[3] A. Parry and D. Crighton, *Asymptotic theory of propeller noise. I - Subsonic single-rotation propeller,* AIAA Journal **27**, 1184 (1989).

[4] Tomas Sinnige, *Aerodynamic and Aeroacoustic Interaction Effects for Tip-Mounted Propellers An Experimental Study*, Ph.D. thesis, TU Delft, Delft (2018).

[5] B. Magliozzi, D. B. Hanson, and R. K. Amiet, *Aeroacoustics of Flight Vehicles: Theory and Practice*, Tech. Rep. Volume 1: Noise Sources (NASA, 1991) this is a report related to the aeroacoustics of flight vehicles, specifically noise sources.

[6] D. B. Hanson, *Influence of Propeller Design Parameters on Far-Field Harmonic Noise in Forward Flight,* AIAA Journal **18**, 1313 (1980).

[7] A. Pagano, L. Federico, M. Barbarino, F. Guida, and M. Aversano, *Multi-Objective Aeroacoustic Optimization of an Aircraft Propeller,* in *12th AIAA/ISSMO Multidisciplinary Analysis and Optimization Conference* (American Institute of Aeronautics and Astronautics, Victoria, British Columbia, Canada, 2008).

[8] David A. McCurdy, *Annoyance Caused by Advanced Turboprop Aircraft Flyover Noise*, Tech. Rep. NASA Technical Paper 2782 (NASA Langley Research Center, Hampton, Virginia, 1988).

[9] D. C. Akiwate, P. Joseph, A. Parry, and C. Paruchuri, *On the balance between the tonal and broadband noise of isolated propellers,* International Journal of Aeroacoustics **23**, 122 (2024), publisher: SAGE Publications.

[10] Dongwen Xue, Qun Yan, Zhuohan Li, and Kai Wei, *Multidisciplinary Optimization Design of Low-Noise Propellers,* MDPI Aerospace (2023).

[11] A. J. Evans and G. Liner, *A Wind-tunnel Investigation of the Aerodynamic Characteristics of a Full-scale Sweptback Propeller and Two Related Straight Propellers,* (1951), nTRS Author Affiliations: NTRS Report/Patent Number: NACA-RM-L50J05 NTRS Document ID: 19930090397 NTRS Research Center: Legacy CDMS (CDMS).

[12] O. Gur and A. Rosen, *Comparison between Blade-Element models of propellers,* The Aeronautical Journal **112**, 689 (2008).

[13] R. T. H. I. Airport, *Smart rotors,* (2023), accessed: 2024-08-24.

[14] J. Katz and A. Plotkin, *Low Speed Aerodynamics - From Wing Theory to Panel Method*, Cambridge Aerospace Series (Cambridge University Press, Cambridge, United Kingdom, 2001).

[15] Thielen, *Effects of Elasticity on Aeroacoustic Performance of Low-Noise Swept Propellers | TU Delft Repository,* (2024).

[16] J. Goyal, F. Avallone, and T. Sinnige, *Isolated propeller aeroacoustics at positive and negative thrust,* Aerospace Science and Technology **147** (2024), 10.1016/j.ast.2024.109021, publisher: Elsevier Masson s.r.l.

[17] A. Malim, N. Mourousias, B. G. Marinus, and T. D. Troyer, *Structural design of a large-scale 3d-printed high-altitude propeller: Methodology and experimental validation,* Aerospace **10**, 256 (2023).

[18] O. Zaporozhets, V. Isaienko, and K. Synylo, *Trends on current and forecasted aircraft hybrid electric architectures and their impact on environment,* Energy **211**, 118814 (2020).

[19] M. Nöding and L. Bertsch, *Application of Noise Certification Regulations within Conceptual Aircraft Design,* Aerospace **8**, 210 (2021).

[20] E. J. H. Lynam and H. A. Webb, *The emission of sound by airscrews*, Tech. Rep. R. & M. No. 624 (Advisory Committee for Aeronautics, London), 1919).

[21] F. Metzger, *An assessment of propeller aircraft noise reduction technology*, Tech. Rep. (NASA, Hampton, Viginia, 1995).

[22] K. Johnson, *How Aviation Weathered the Fuel Crisis of the 1970s,* (2022).

[23] C. Mikkelson, A. Mitchell, and J. Bober, *Summary of Recent NASA Propeller Research,* (1984).

[24] J. Banke, *Beauty of Future Airplanes is More than Skin Deep - NASA,* (2010).

[25] E. Torenbeek, *Advanced aircraft design: conceptual design, analysis, and optimization of subsonic civil airplanes*, Aerospace series (John Wiley & Sons Inc, Chichester, West Sussex, United Kingdom, 2013).

[26] H. Swift, *A Review of the Literature Related to Potential Health Effects of Aircraft Noise*, Tech. Rep. PARTNER-COE-2010-003 (Partnership for AiR Transportation Noise and Emissions Reduction (PARTNER), Ray W. Herrick Laboratories, Purdue University, 2010) this work was funded by the U.S. Federal Aviation Administration Office of Environment and Energy under Cooperative Agreement 07-C-NE-PU, Amendments No. 002, 010, 017, 029. The project was managed by Mehmet Marsan. The author acknowledges the help provided by Dr. Larry Finegold, for providing access to a large body of literature on health effects of noise, which made initiation of this project much easier, and for his careful editing of the report and suggestions for improvements.

[27] S. Khalid, J. Wojno, A. Breeze-Stringfellow, D. Lurie, T. Wood, K. Ramakrishnan, and U. Paliath, *Open rotor designs for low noise and high efficiency,* (2013).

[28] A. Filippone, *Aircraft noise prediction,* Progress in Aerospace Sciences **68**, 27 (2014).

[29] B. Marinus, M. Roger, and R. Van Den Braembussche, *Aeroacoustic and Aerodynamic Optimization of Aircraft Propeller Blades,* in *16th AIAA/CEAS Aeroacoustics Conference* (American Institute of Aeronautics and Astronautics, Stockholm, Sweden, 2010).

[30] W. Dongchen, S. Bifeng, J. Jun, and W. Haifeng, *High-altitude airship propulsion system optimal design and experiment based on energy balance,* Proceedings of the Institution of Mechanical Engineers, Part G: Journal of Aerospace Engineering **237**, 3 (2023), number: 1 Publisher: SAGE Publications Ltd.

[31] J. Ruijgrok., *Elements of airplane performance (second edition) | TU Delft Repository* (VSSD, Delft, 2009).

[32] Q. Wald, *The aerodynamics of propellers,* Progress in Aerospace Sciences **42**, 85 (2006).

[33] B. Magliozzi, D. B. Hanson, and R. K. Amiet, *Propeller and Propfan Noise*, Tech. Rep. (NASA Langley Research Center, 1991).

[34] C. J. Miller and J. P. Sullivan, *Noise Constraints Effecting Optimal Propeller Designs,* (1985) p. 850871.

[35] O. Gur and A. Rosen, *Multidisciplinary Design Optimization of a Quiet Propeller,* in *14th AIAA/CEAS Aeroacoustics Conference (29th AIAA Aeroacoustics Conference)* (American Institute of Aeronautics and Astronautics, Vancouver, British Columbia, Canada, 2008).

[36] G. Margalida, T. Sinnige, K. Knepper, B. Soemarwoto, and R. Nahuis, *Low Fidelity Multidisciplinary Methodology for Efficient and Quiet Propeller Design: Numerical Investigation and Experimental Validation,* in *30th AIAA/CEAS Aeroacoustics Conference (2024)*, Aeroacoustics Conferences (American Institute of Aeronautics and Astronautics, 2024).

[37] D. Ingraham, J. S. Gray, and L. V. Lopes, *Gradient-Based Propeller Optimization with Acoustic Constraints,* in *AIAA Scitech 2019 Forum* (American Institute of Aeronautics and Astronautics, San Diego, California, 2019).

[38] B. G. Marinus, *Multidisciplinary Optimization of Aircraft Propeller Blades*, Ph.D. thesis, Royal Military Academy, Brussels, Belgium (2011), doctoral dissertation, Polytechnical Faculty, Department of Mechanical Engineering, Royal Military Academy; Department of Turbomachinery and Propulsion, Von Karman Institute; Centrale Lyon - University Lyon I.

[39] D. Hanson, *Helicoidal surface theory for harmonic noise of propellers in the far field,* AIAA Journal **18**, 1213 (1980).

[40] R. Aalmoes, K. Knepper, N. Sieben, W. De Haan, G. Margalida, and T. Sinnige, *Sound Perception Study of Auralized Novel Propeller Design for Future Electrical Air Mobility Platforms,* in *30th AIAA/CEAS Aeroacoustics Conference (2024)* (American Institute of Aeronautics and Astronautics, Rome, Italy, 2024).

[41] P. Yu, J. Peng, J. Bai, X. Han, and X. Song, *Aeroacoustic and aerodynamic optimization of propeller blades,* Chinese Journal of Aeronautics **33**, 826 (2020).

[42] B. G. Marinus, *Comparative Study of Effects of Sweep and Humps on High-Speed Propeller Blades,* AIAA Journal **52**, 739 (2014).

[43] H. Lee, B. Sengupta, M. S. Araghizadeh, and R. S. Myong, *Review of vortex methods for rotor aerodynamics and wake dynamics,* Advances in Aerodynamics **4**, 20 (2022).

[44] W. Huang, R. Tang, and H. Ma, *The review of Vortex lattice method for offshore wind turbines,* Renewable Energy **236**, 121450 (2024).

[45] A. Rosen and O. Gur, *A novel approach to actuator disk modeling,* National Aerospace Laboratory NLR - 32nd European Rotorcraft Forum, ERF 2006 **3**, 1207 (2007).

[46] X. Geng, T. Hu, P. Liu, T. Sinnige, and G. Eitelberg, *ANALYSIS OF THRUST-SCALED ACOUSTIC EMISSIONS OF AIRCRAFT PROPELLERS AND THEIR DEPENDENCE ON PROPULSIVE EFFICIENCY,* in *Congr. Int. Counc. Aeronaut. Sci., ICAS* (International Council of the Aeronautical Sciences, 2021) journal Abbreviation: Congr. Int. Counc. Aeronaut. Sci., ICAS.

[47] H. Schlichting and K. Gersten, *Boundary-Layer Theory* (Springer Berlin Heidelberg, Berlin, Heidelberg, 2017).

[48] ICAO, *Title: Annex 16 to the Convention on International Civil Aviation, Environmental Protection, Volume IV - Carbon Offsetting and Reduction Scheme for International Aviation (CORSIA)*, Tech. Rep. Annex 16, Volume IV (ICAO, Montreal, Canada, 2023).

[49] ICAO, *Environmental Technical Manual Volum1 Procedures for the Noise Certification of Aircraft*, Tech. Rep. (ICAO, 2018).

[50] D. Hanson, *Near-field frequency-domain theory for propeller noise,* AIAA Journal **23**, 499 (1985).

[51] J. Sodja, R. De Breuker, D. Nozak, R. Drazumeric, and P. Marzocca, *Assessment of low-fidelity fluid–structure interaction model for flexible propeller blades,* Aerospace Science and Technology **78**, 71 (2018).

[52] D. C. Montgomery, ed., *Design and analysis of experiments,* eighth edition ed. (John Wiley & Sons, Inc, Hoboken, NJ, 2013).

[53] ATR, *Atr 72-600 aircraft specifications,* (2020), accessed: 2025-04-01.

[54] The MathWorks, Inc., *fmincon – Find minimum of constrained nonlinear multivariable function*, The MathWorks, Inc., Natick, Massachusetts (2024), available at `https://www.mathworks.com/help/optim/ug/fmincon.html`.

[55] D. Melpignano, *Effects of the Unsteady Blade Loading on the Aero-Acoustic Performance of a Boundary Layer Ingesting Propeller | TU Delft Repository,* (2024).